Modeling and Testing of a Micro-Tubular Low-Temperature Fuel Cell for use in a Micro Air Vehicle

Richard Blaine Evans

Thesis submitted to the Faculty of the
Virginia Polytechnic Institute and State University
in partial fulfillment of the requirements for the degree of

Master of Science
in
Mechanical Engineering

Dr. Michael R. von Spakovsky, Chair
Dr. Michael W. Ellis
Dr. Douglas J. Nelson

December 19, 2007
Blacksburg, Virginia

Keywords: PEM Fuel Cell, Micro-tubular, Micro Air Vehicle

Modeling and Testing of a Micro-Tubular Low-Temperature Fuel Cell for use in a Micro Air Vehicle

Richard Blaine Evans

Abstract

Micro air vehicles (MAVs) are small remote controlled aircraft used by military personnel for reconnaissance and are currently powered by batteries. The MAVs rely on the battery for propulsion, navigation, and reconnaissance equipment. The thrust of this research is to develop a fuel cell system capable of higher energy densities, higher energy to weight ratios, and increased overall energy output than the batteries in use today. To this end, a feasibility study is first conducted to determine if fuel cells could be used to replace batteries as the MAV energy source and what fuel cell configurations would show the best performance. Hydrogen, methanol, and formic acid fuel cells are considered, using a conventional flat-plate design and a novel micro-tubular design. Several micro-tubular fuel cells (MTFCs) are tested to show that these cells are a possibility for energy production in MAVs. Those tested are developed and improved in collaboration between Luna Innovations, Inc. and the Center for Energy Systems Research at Virginia Tech and then manufactured by Luna Innovations, Inc. Also, an isothermal, lumped-parameter (LP) model for MTFCs is developed to predict behavior. The use of this LP model aids in understanding the dominant losses of the cell and ways of improving cell performance.

Results from the feasibility study indicate that by using methanol powered MTFCs a 50% increase in overall energy output is possible, while also decreasing the mass of the power production system. Through testing and an iterative design process, an increase of three orders of magnitude of the maximum power production of the MTFCs constructed by Luna Innovations, Inc., has been realized. Results of the LP MTFC model are compared with the experimental results from the MTFC testing and tubular cells from the literature.

Acknowledgements

I would like to express my sincere appreciation to my wife, Katharine, and daughters, Hannah and Rebekah, for supporting me. Without their support I would not only have been hungry and lonely, but I would have lost my mind as well. Thank you for keeping me happy, sane, and fed. I give thanks to my Lord and Savior Jesus Christ for his sacrifice, love, and sustaining influence. I am grateful for the inspiration and strength that was given during times of difficulty, of which there were many in this research. Thank you also to Dr. von Spakovsky for his work and efforts in my behalf on this research. A special thanks to family and friends that have helped us during this time. I will forever be indebted and grateful to my parents for their sacrifices and examples that encouraged me to seek a higher education and to pursue a life-long goal of learning.

Table of Contents

List of Figures

List of Tables

Nomenclature

A_A Active Area (mm^2)

ϕ_{Anode} Anode relative humidity

π Constant PI (3.141)

ρ_C Density of the catalyst layer (gm/mm^3)

ρ_E Density of the electrode layer (gm/mm^3)

ρ_T Density of the Nafion™ layer (gm/mm^3)

ρ_P Density of the tube plate layer (gm/mm^3)

H_W Height of outer walls (mm)

H_T Height of tubes (mm)

θ Inside diameter of the Nafion™ tube (mm)

α Inside diameter of the Nafion™ tube with catalyst and electrode layers (mm)

L_P Length of tube plate (mm)

L_T Length (total) of tube needed to equal active area (mm)

m_P Mass of tube plate (kg)

m_W Mass of outer walls (kg)

m_T Mass of tubes (kg)

m_{TOT} Mass of system (total) (kg)

$x_{H_2O,i}^{Anode}$ Molar fraction of water

$x_{H_2,i}^{Anode}$ Molar fraction of hydrogen

ϕ Outside diameter of the Nafion™ tube (mm)

β Outside diameter of the Nafion™ tube with catalyst and electrode layers (mm)

P_{H_2} Partial pressure of hydrogen (kPa)

P_v Partial pressure of water (kPa)

P_s Pitch (square formation) (mm)

P_{DC} Pitch of the columns (diamond formation) (mm)

P_{DR} Pitch of the rows (diamond formation) (mm)

P_v'' Saturated water pressure (kPa)

t_C Thickness of the catalyst layer (mm)

t_P Thickness of the tube plate (mm)

t_W Thickness of the outer walls (mm)

t_E Thickness of the electrode layer (mm)

ρ_W Thickness of the outer walls layer (gm/mm^3)

P_{Anode} Total anode pressure (kPa)

W_T Width of tube plate (mm)

W_W Width of outer walls (mm)

η Total number of tubes needed to equal the calculated active area

V_S Total volume required (square formation) (mm^3)

V_D Total volume required (diamond formation) (mm^3)

Chapter 1

Introduction

Portable electronic devices have grown increasingly more powerful and complex in recent years. Demand for these devices increases as they are made both smaller and more portable. However, the energy required to power these devices has also escalated significantly. Battery technology has been stretched to the limit to provide sufficient power. As these devices continue to evolve, power systems with higher energy densities, lower system masses, and faster recharge times will be demanded. With superior energy densities, lower system masses, high efficiencies, and rapid recharges, fuel cell systems are posed to take over the position currently held by batteries in powering portable electronic devices.

1.1 Historical Development of Fuel Cell Technology

William Robert Groves built the first functioning fuel cell in 1843. This cell was based upon a description of experiments that Christian Friedrich Schönbein had performed. The next great improvement of fuel cell design came from W. Thomas Grubb in 1955 with the use of a new membrane material In 1959 Francis Thomas Bacon developed a 5 kWe stationary fuel cell. Several types of cells have been developed since that range from the mWe systems of microbial fuel cells to 100 MWe systems of solid oxide fuel cells. Major fuel cell types include:

- Proton Exchange Membrane Fuel Cell (PEMFC)
- Direct Methanol Fuel Cell (DMFC)
- Solid Oxide Fuel Cell (SOFC)
- Phosphoric Acid Fuel Cell (PAFC).
- Molten Carbonate Fuel Cell (MCFC)
- Alkaline Fuel Cell (AFC)

Recently several small portable fuel cells have been designed to replace batteries as power sources. In 2004 Toshiba announced the development of a DMFC that only weighs 8.5 g, and produces 100 mWe (Toshiba, 2004). It was designed to run a MP3 player for 20 hours on a 2 cc charge of concentrated methanol (MeOH). Sanyo has produced a prototype DMFC for use with laptop computers. The total system weighs about 2 kilograms and can produce 12 We for 8 hours using 130 cm^3 of MeOH (Kallender, 2005). Panasonic at the beginning of 2006 unveiled a prototype DMFC for laptop computers which has a tank of 200 cm^3 and a runtime of 20 hours (Williams, 2006). As research and new materials have become available small portable fuel cells have become a reality.

1.2 Fuel Cells for Micro Air Vehicle Applications

Current battery technology lags power requirements in the area of micro air vehicles (MAVs), which demand high power output and low weights. MAVs are small remote controlled aircraft that are used by military personnel for reconnaissance. They are small and light-weight. For example, the KJ Special Vision Based MAV shown in Figure1.1 was designed and constructed by the University of Florida Micro Air Vehicle

Figure 1.1 KJ Special Vision Based MAV built by University of Florida Micro Air Vehicle Laboratory (MAV Lab. University of Florida, 2007)

Laboratory to be used for reconnaissance. Using lithium polymer ion battery technology it achieves a flight time of only 20 minutes. It weighs a total of 15 oz. and has a flight

range of 3 miles. The University of Florida Micro Air Vehicle Laboratory has also designed another MAV designed for reconnaissance. It was designed for the US Air Force to be released with bombs to assess the damage done to bombing targets. It has foldable wings that allow it to be stored in a canister that is 4.5 inches in diameter and 18 inches long for easy transport by a soldier or easy attachment to a bomb for deployment. Using lithium polymer ion battery technology it achieves a flight time of only 15 minutes. It weighs a total of 16 oz. and has a flight range of 5 miles.

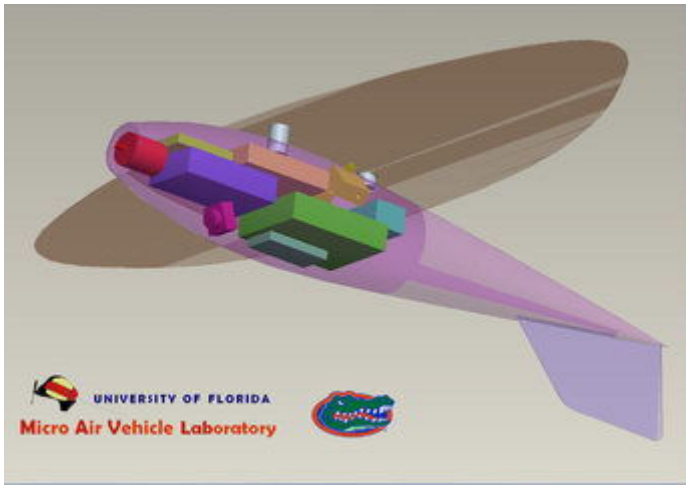

Figure 1.2 Bomb Damage Assessment MAV schematic of components (MAV Lab. University of Florida, 2007)

Battery life is currently the largest limiting factor on MAV missions. The MAVs rely on battery power for propulsion, navigation, and reconnaissance equipment. A larger energy supply than those currently used in the MAVs mentioned above would enable extended missions with better reconnaissance data. To create a larger energy supply with current battery technology would require a larger and heavier battery to be used. This would increase the size and weight of the MAV. Since MAVs may be carried by soldiers for example for extended periods of time increasing the size and weight of the MAV is not a viable option. One method of creating a larger energy supply without increasing the size or weight of the MAV might be the use of cutting edge fuel cell technology. For example the Panasonic DMFC discussed above that can power a laptop for 20 hrs on a 200 mL charge of methanol (Williams, 2006). Not only does this show that such a fuel cell can beat the best current battery technology but that the time to recharge is not an

issue because replacing the cartridge is much quicker than waiting for the battery to recharge.

1.3 Proton Exchange Membrane and Direct Methanol Fuel Cells

Each of the different types of fuel cells have unique strengths and weaknesses. For example PEMFC and DMFC cells are limited to low temperatures because of the membrane electrode assembly (MEA). The polymer material of the MEA begins to experience a failure in the material at temperatures over 120 ^{o}C for MEAs using Nafion™. Most PEMFCs use Nafion™ 112 because it has a thickness of only 0.05 mm (Larminie and Dicks, 2003). As the membrane becomes thinner the membrane resistances are also decreased (Springer, Zawodzinski, and Gottesfeld, 1991). Many DMFCs use Nafion™ 117 which has a thickness of 0.18 mm (Larminie and Dicks, 2003). The thicker membrane allows less fuel crossover (Larminie and Dicks, 2003), this will be discussed in more detail in Section 1.3.2.

Another type of cell, which are high temperature cells are large, complex, and extremely hot. The time needed to bring the cells up to temperature is another disadvantage. The tremendous heat produced by high temperature cells could potentially damage MAV components. The size and complexity of high temperature cells precludes them as a viable energy source for MAVs.

Alkaline fuel cells (AFCs) are not viable for use in MAVs because they require pure reactants. AFCs need both pure hydrogen and pure oxygen to avoid catalyst poisoning which causes poor cell performance. MAVs do not have sufficient volume to store both hydrogen and oxygen.

PEMFCs and DFMCs have several advantages that make them excellent candidates to replace batteries as the energy source for MAVs. The low temperatures of PEMFC and DMFCs make them able to achieve quick startups; also both use air as the reactant instead of pure oxygen. PEMFCs have high mass and volume energy densities. DMFCs also can have high mass and energy volume densities depending of the system configuration. This system configuration is discussed in more detail in Section 3.2. PEMFCs and DMFCs can have very simple passive systems which are also discussed in

Section 3.2. It is possible to create PEMFC and DMFCs that are as small as 1 mm^3 without a loss of power density (Mench et al 2001).

1.3.1 Proton Exchange Membrane Fuel Cells

PEMFC cells use hydrogen as a fuel source. The hydrogen flows to the anode where it electrochemically reacts in the electrode catalyst layer (usually containing platinum as the catalyst).The electrochemical reaction at the anode is:

$$H_2 \Leftrightarrow 2H^+ + 2e^- \tag{1-1}$$

The MEA allows conduction of the hydrogen ions or protons (H^+) through the polymer electrolyte to the cathode catalyst layer, but does not allow the conduction of electrons. This is illustrated in Figure 1.3 which shows the anode and cathode reactions as well as the proton and electron paths. The electrons are collected by a current collector and are

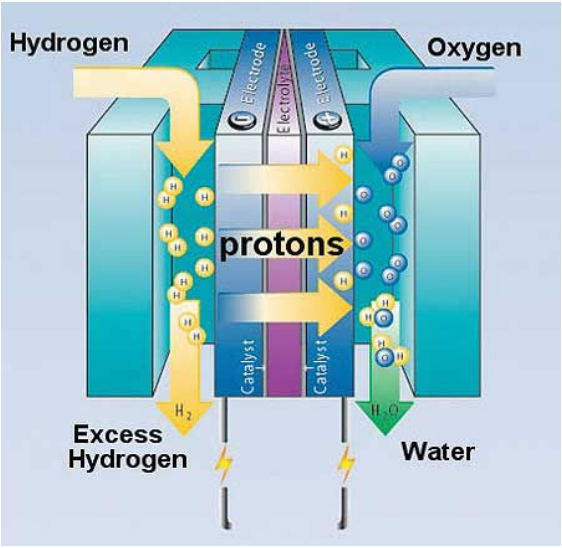

Figure 1.3 Flat-plate PEMFC (Joint Service Pollution Prevention and Sustainability Technical Library, 2005)

routed through an external circuit to the cathode catalyst layer as can be seen at the bottom of Figure 1.3. On the cathode side the hydrogen ions, electrons, and oxygen (generally from air) combine in the catalyst layer via the following electrochemical reaction:

$$\frac{1}{2}O_2 + 2H^+ + 2e \Leftrightarrow H_2O \quad (1\text{-}2)$$

This second reaction is exothermic, releasing energy which depending on the size and number of cells may need to be transferred out of the fuel cell in order to sustain the fuel cell's operating temperature.

1.3.2 Direct Methanol Fuel Cells

DMFCs have a high energy storage density making them more appealing when compared to the hydrogen storage if PEMFCs for which generally the energy storage density is lower. DMFCs are a PEMFC modified in terms of the reactant fuel this is discussed in detail below. Instead of hydrogen, methanol (CH_3OH) is used as the fuel. A variation on DMFCs is the direct formic acid fuel cell (DFAFC) which use formic acid

Table 1.1 Electrochemical reaction equations for oxidation of CH_3OH

Reactants	Products
CH_3OH	$CH_2OH+H^++e^-$
CH_2OH	$CHOH+H^++e^-$
	$CH20+H^++e^-$
CHOH	$CHO+H^++e^-$
	$COH+H^++e^-$
CHO	$CO+H^++e^-$
COH	$CO+H^++e^-$
$CHO+H_2O$	$HCOOH+H^++e^-$
$CO+H_2O$	$COOH+H^++e^-$
HCOOH	$COOH+H^++e^-$
COOH	$CO2+H^++e^-$

(HCOOH) as a fuel. Formic acid is an intermediate step in the electrochemical conversion of CH_3OH (sometimes also written MeOH) to H_2 and CO_2 in a DMFC (see Table 1.1). DMFCs work by using a methanol (MeOH) and water mixture at the anode of the fuel cell. The anode electrode catalyst layer is where the hydrogen is generated when the MeOH-water mixture reacts. The step reactions to the overall MeOH reaction can be seen below in Figure 1.4 (Larminie and Dicks, 2003) and the electrochemical reactions of these steps are found in Table 1.1. This reaction produces carbon dioxide, hydrogen,

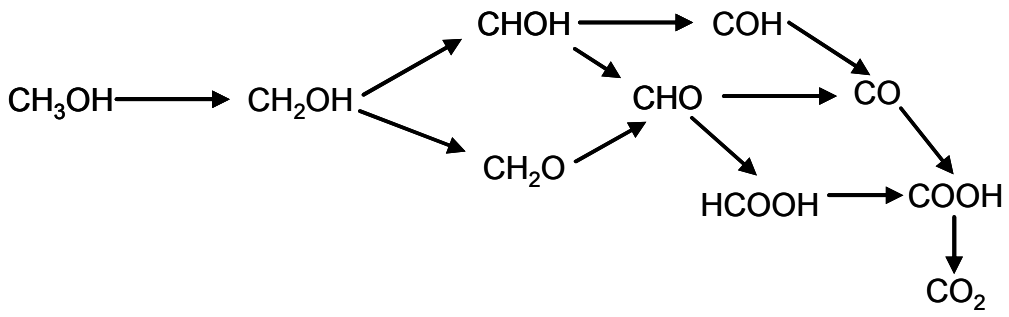

Figure 1.4 Oxidation of CH_3OH at anode

and releases six electrons which flow through the external load to be used for power. The DMFC cathode reaction is exactly the same as the PEMFC cathode reaction. DMFCs have much lower efficiencies than PEMFCs because the anode reaction is much slower for DMFCs and MeOH is readily absorbed by the membrane and thus goes through the membrane without reacting with the catalyst layer, and then it reacts on the cathode side. This phenomenon is call cross-over. To increase the performance of DFMCs different catalysts are used on the catalyst layers of the DMFC to speed up the reactions (see Section 4.2.2), and thicker membranes of Nafion™, e.g. Nafion™ 117. Using wicking technology DMFCs can achieve greater efficiencies and even higher energy storage density rates. Wicking technology is discussed in Section 3.6.

1.4 Fuel Cell Geometries

There are two basic types of PEMFC and DMFC fuel cell geometries: flat-plate and tubular. Although the method for producing power is the same regardless of the geometry, the components of these geometries vary as discussed below.

Figure 1.3 shows a fuel cell with a flat-plate geometry. The major components of a flat-plate cell include bipolar plates (blue plates on the outside), gas diffusion layer (GDL) (shown as electrodes), and MEA (electrolyte and catalyst layers) as shown in Figure 1.3. Bipolar plates provide hydrogen and oxygen flow channels and act as electron conductors. Gas diffusion layers act as electron collection and dispersion media and also serve to distribute gases to and from the MEA flow channels on the bipolar plates.

Tubular cells presently are the principal geometry used SOFCs, but are rare in PEMFCs and DMFCs. Figure 1.5 shows the geometry of a tubular cell cross-section,

while Figure 1.6 provides an axial view. The major components of a tubular cell include conduction layers, catalyst layers, and the MEA. Flat-plate cells have higher energy densities than tubular cells depending on the system configuration (see Section 6.1.5), but they are heavier and more expensive than tubular cells because of the cost of machining precise flow channels into the bipolar plates. The extra weight of the flat-plate cells are from the aluminum bipolar plates. Instead of bipolar plates, tubular cells use very thin conduction layers, e.g. 5 microns (Gunter, 2007, Phase I Final Report). Hydrogen is channeled through the center of the cell, while the outside of the cell is exposed to air, thus, eliminating the need for bipolar plates to act as channels, and the need for a GDL to distribute gases.

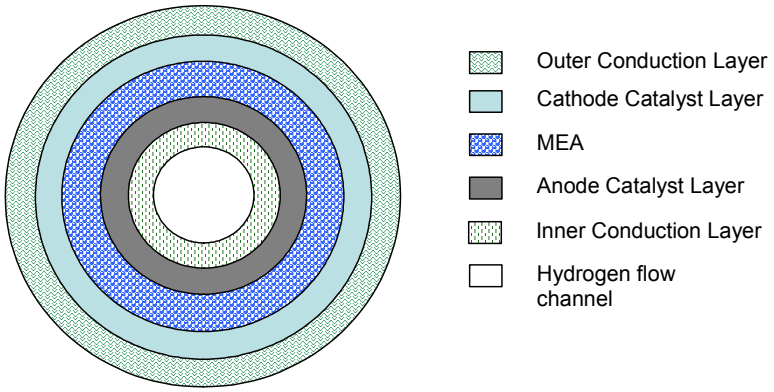

Figure 1.5 Cross-sectional view of a tubular PEMFC or DMFC

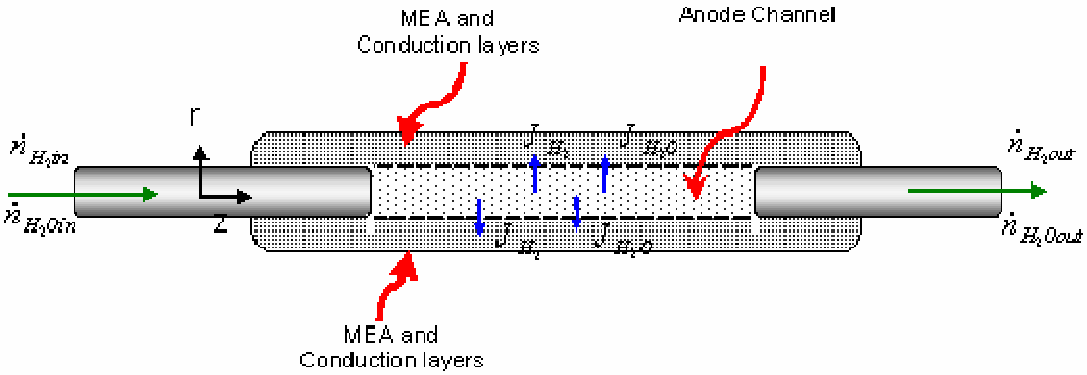

Figure 1.6 Axial view of tubular PEMFC showing flow of hydrogen and water into the cell and through the membrane

1.5 Thesis Objectives

The current largest limiting factor on MAV missions is insufficient energy. If the current power source (battery) was replaced by a fuel cell with a higher energy density this would allow prolonged MAV missions. Optimization of the fuel cell for use in MAVs requires a detailed comparison of PEMFCs, DMFCs, and DFAFCs of both tubular and flat-plate geometries, and different cell arrangements to find the best configuration of fuel cell type and geometry. This is explored in a feasibility study presented below. Development of flexible micro-tubular fuel cells (MTFCs) would enable further optimization of a fuel cell system for use in MAVs by allowing cells to be placed in non-traditional locations such as the tail of the MAV. Development of a model to predict losses, current density, voltage, and power density of MTFCs, would enable design changes to minimize the major losses. Experimental testing to validate the model is undertaken. Experimental testing is also used to evaluate current MTFC performance, i.e. current density, voltage, power density, and the magnitude of losses within the cell. Thus the major objectives of this thesis are as follows:

- Gain an understanding of the fundamental principles of fuel cells, particularly PEMFCs. These fundamentals include: electrochemical conversion, reaction kinetics, ionic conduction, and resistive losses within the cell.
- Determine the feasibility of using several fuel cell types, geometries, and cell arrangements for use in MAV applications using various performance criteria (i.e. energy, volumetric energy density, and mass energy density) to establish the most promising fuel cell configurations for the application.
- Establish testing criteria and methods for single MTFCs using hydrogen or methanol. Then using these criteria and methods to record the performance, i.e. current density, voltage, power density, and the magnitude of losses, of 13 different cells constructed by Luna Innovations, Inc. using Electrochemical Impedance Spectroscopy (EIS) and polarization curves.

- Develop a first principles model of a MTFC to predict losses, current density, voltage, and power density of MTFCs, to enable design changes which will minimize major losses in the cell, this will include the following components:
    - Through the Membrane Model
        - Anode Electrochemical Reaction Model
        - Cathode Electrochemical Reaction Model
    - Along the Channel Model
    - Resistance Losses Model
        - Activation Losses
        - Ohmic Losses
        - Concentration Losses
    - Electrical Model
- Use the results from MTFC lab testing and modeling to make recommendations on design changes and the experimental setup to enhance cell performance.

Chapter 2

Literature Survey

This chapter gives a brief overview of the available literature that is relevant to the analytical/numerical modeling and experimental testing of micro-tubular PEMFCs and DMFCs. The literature surveyed is split into three different areas: analytical/numerical models of PEMFCs with flat plate geometries, analytical/numerical models of PEMFCs with tubular geometries, and experimental testing of PEMFCs and DMFCs. Some of the results presented in this chapter will then be compared in Chapter 6 with the model and its results developed here for MTFCs. The full discussion of this model and the assumptions made is discussed in Chapter 5.

2.1 Proton Exchange Membrane Fuel Cells with Flat Plate Geometries

One of the first analytical/numerical models developed for simulating flat plate PEMFC behavior was that of Springer, Zawodzinski, and Gottesfeld (1991). This 1-D steady flow through the thickness model accounts for water content in the membrane, water diffusion, electro- osmotic drag in the membrane, the depletion of reactants, and the production of products. Figure 2.1 shows a schematic diagram of the fuel cell model developed by Springer Zawodzinski, and Gottsfeld (1991) where the cell is split into zones which include the gas diffusion layers (GDLs) of the anode and cathode and the membrane with the cathode and anode catalyst layers. Table 2.1 (Siegel, 2003) summarizes the model characteristics. This model is simple yet very effective means to model the performance of PEMFC for flat-plate cells in only one dimension (through the channel). Springer et al. show that by splitting the cell into zones (see Figure 2.1), where the catalyst layers are treated as interface sources and sinks, and assuming that product and reactant properties throughout each zone are constant one can create species balances on each zone. The species balances include one for the movement of water liquid water

transport is ignored) into and out of the GDLs and membrane as well as its creation at the

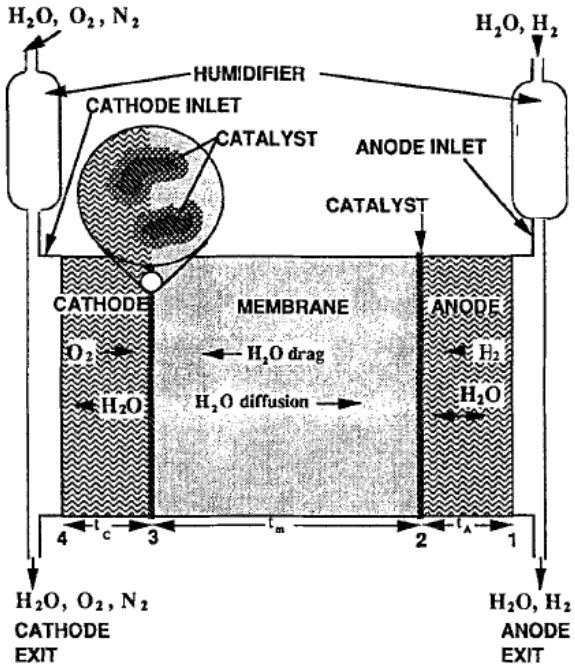

Figure 2.1 Schematic diagram of the fuel cell model developed by Springer, Zawodzinski, and Gottesfeld (1991) Reproduced by permission of The Electrochemical Society.

cathode. This tracking of the water balance of the cell enables the authors to predict the effect of water transport on cell performance, which is found to be large. The authors validate this model with experimental data from experiments conducted measuring the flow of water through the membrane by measuring the inlet and outlet flow conditions, and using high frequency resistance measurements the membrane resistance was found. The authors report that the experimental measurements of the flow of water through the membrane agree well with model predictions for cells are that operated under conditions where liquid water is not present. The authors report that model and experimental results for membrane resistance both show increases in membrane resistance as the current density is increased. In the fuel cell model developed and presented in Chapter 5 for MTFCs, an approach similar to that of Springer, Zawodzinski, and Gottesfeld which accounts for the effects of water transport and reactant depletion is used and modified to account for the geometric effects of the tubular shape.

Table 2.1 1-D through the thickness PEMFC model of Springer, Zawodzinski, and Gottesfeld (1991) taken from Siegel, (2003)

Model	Polymer Electrolyte Fuel Cell Model
Authors	Springer, Zawodzinski, and Gottesfeld (1991)
Regions	• Polymer membrane and both gas diffusion layers
Dimensionality	• One – through the thickness
Assumptions	• Steady-state • Isothermal • One-dimensional • Catalyst is an interface • Polymer water content data at 30 C applies at 80 C • Liquid water effects neglected
Phenomena investigated	• Transport of water and protons through the polymer membrane • Changes in ionic resistance with current density and water content • Effect of membrane temperature and thickness on performance
Main conclusions	• Net water flux across the membrane is less than that predicted by electro-osmotic drag alone • Thinner membranes offer advantages in decreased resistance and water flux from anode to cathode
Limits	• The model focuses principally on performance issues associated with the polymer membrane alone and does not consider liquid water accumulation and the related mass transport effects.

A second PEMFC model of interest is that by Yi, and Nguyen (1998). Yi and Nguyen propose a down the channel and through the thickness model which includes more phenomena than that of Springer, Zawodzinski, and Gottesfeld. These parameters include water transport across the membrane due to a pressure gradient, a temperature distribution in the solid portion (bipolar plates) forming the flow channels, and energy removal via a heat interaction by natural convection and by heat exchangers. A schematic of the modeling region used is shown in Figure 2.2 and Table 2.2 (Siegel, 2003). The flow channel and membrane used to setup the model are clearly shown in Figure 2.2. The results of this model show that a higher pressure on the cathode side improves membrane conductivity (see Table 2.2) and that injecting water into the anode at different parts of

the channel, cell performance can be enhanced. Results of cell performance using

Table 2.2 2-D down the channel and through the thickness PEMFC mode of Yi and Ngyuen (1998) taken from (Siegel, 2003)

Model	**An Along-the-channel Model for Proton Exchange Membrane Fuel Cells**
Authors	Yi and Nguyen(1998)
Regions	• Gas channels, current collectors, membrane
Dimensionality	• Two – through the thickness and down the channel
Assumptions	• Steady • Laminar flow • Incompressible • Gas transport resistance is neglected in GDL and catalyst layers • Drag and water diffusion coefficient are determined by anode vapor activity. • Catalyst and GDL are interfaces
Phenomena investigated	• Water transport in the gas channels and membrane • Temperature distribution down the channel • Membrane water transport effects related to an applied pressure gradient
Main conclusions	• Humidification of the anode gas is required for best performance. • An applied pressure gradient can be used to offset anode dehydration due to electro-osmotic drag. • Running the reactants counterflow produces a more uniform temperature distribution than does parallel flow.
Limits	• The treatment of the GDLs and catalyst layers as interfaces makes it impossible to accurately simulate performance, especially at high current densities. • Using the anode vapor activity to set the water content throughout the entire membrane leads to an underestimation of the amount of water in the membrane.

different pressures on the anode and cathode sides is shown in Figure 2.3, which shows that as the pressure on the cathode is increased the overall performance of the cell is enhanced.

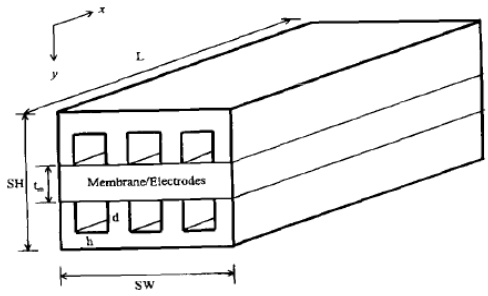

Figure 2.2 Schematic diagram of the modeling region used by Yi and Nguyen (1998) Reproduced by permission of The Electrochemical Society

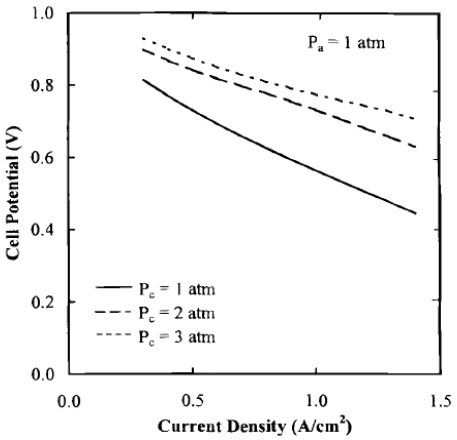

Figure 2.3 Effects of differential pressures as reported by Yi and Nguyen (1998) Reproduced by permission of The Electrochemical Society

In 2003, Ceraolo, Miulli, and Pozio publish a different type of PEMFC flat plate model for both the static and dynamic behavior. A schematic of the 1-D through the

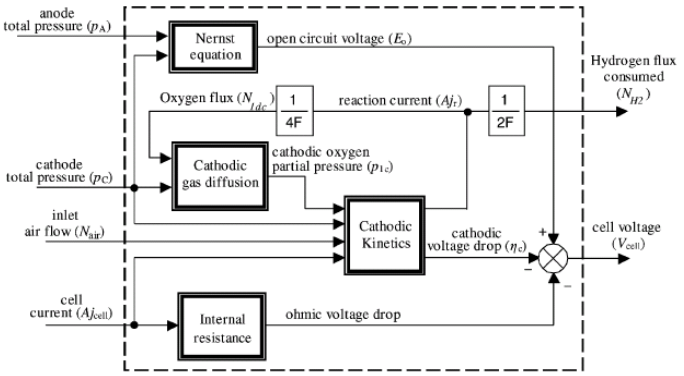

Figure 2.4 Schematic diagram of the 1-D through the thickness model structure used by Ceraolo, Miulli, and Pozio (2003).

thickness semi-empirical model structure used by the authors is shown in Figure 2.4, while the general characteristics of the model are given in Table 2.3. Figure 2.4 gives a general overview of the model showing the inputs and the interconnections between the different sub-models incorporated. This model assumes a constant water saturation of the

Table 2.3 1-D through the thickness PEMFC model of Ceraolo, Miulli, and Pozio (2002)

Model	**Modelling static and dynamic behaviour of proton exchange membrane fuel cells on the basis of electro-chemical description**
Authors	Ceraolo, Miulli, and Pozio (2002)
Regions	• Gas channels, electrodes, and membrane
Dimensionality	• One – through the thickness
Assumptions	• Constant porosity and tortuosity in electrode layers • One-dimensional • Isothermal • Pressure is constant throughout the cell • Partial water pressure is uniform • Membrane is completely saturated • Anodic overpotenials are disregarded
Phenomena investigated	• Steady-state response of fuel cell at different pressures • Dynamic response of fuel cell
Main conclusions	• Increases in pressure yield higher current densities • The behavior of the proposed model shows good agreement with experimental data

membrane as seen in Table 2.3, which makes the membrane conductivity a function of temperature only. The authors not only validate their model through experiments but also incorporate some of the experimental results directly into the model. For example the internal resistance of the cell was found experimentally as a function of temperature and current, this value was then incorporated into the model. The authors report good agreement between the model and experimental results for both static and dynamic load

conditions. Figure 2.5 shows the model and experimental results of a changing anode and cathode pressure on cell performance. The model performs well for cases with a pressure gradient across the membrane, but it seems to slightly under predict performance when no pressure gradient is present across the membrane (see Figure 2.5). Figure 2.6 shows the dynamic response of an experimental fuel cell and for the model of Ceraolo, Miulli, and Pozio. The results generated by the model and the results obtained through testing are virtually identical indicating excellent model performance for dynamic load conditions.

No DMFC tubular models were found, but the Coursange et al. model could be easily modified to model the performance of a tubular DMFC. The changes that would be required to model DMFCs include a change in the anode reaction, so that it includes the various step reactions and a parameter to model the losses caused by cross-over which would be a function of the catalyst layer type and loading as well as the membrane thickness.

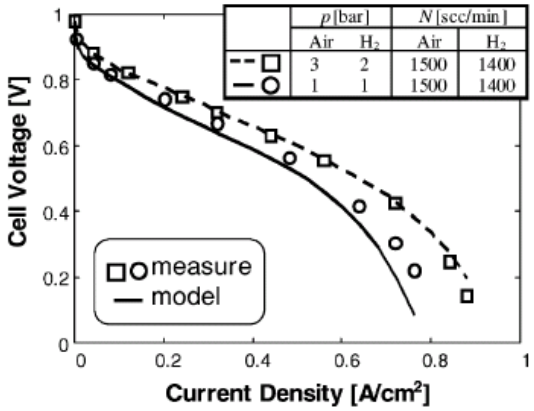

Figure 2.5 Comparison of model generated polarization curve and experimental results for different values of reactant pressures (Ceraolo, Miulli, and Pozio 2003).

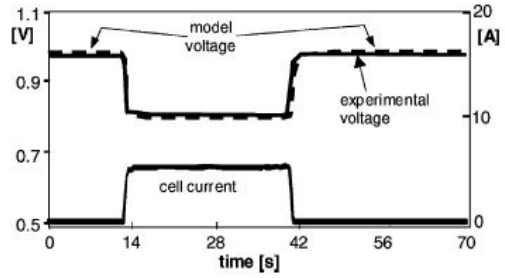

Figure 2.6 Comparison of the dynamic response of the model generated results with experimental results (Ceraolo, Miulli, and Pozio 2003).

2.2 Proton Exchange Membrane Fuel Cells with Tubular Geometries

For SOFCs, the principal geometry of choice is a tubular geometry, while PEMFCs generally have flat-plate geometries. As if yet there are very few PEMFC models that have been developed for tubular cells. One such model is that of Coursange, Hourri, and Hamelin (2003). The authors present 3-D models for both planar and tubular shaped PEMFCs. Figure 2.7 shows that for the flat-plate configuration used, while Figure 2.8 shows that for the tubular configuration used by Coursange, Hourri, and Hamelin (2003).

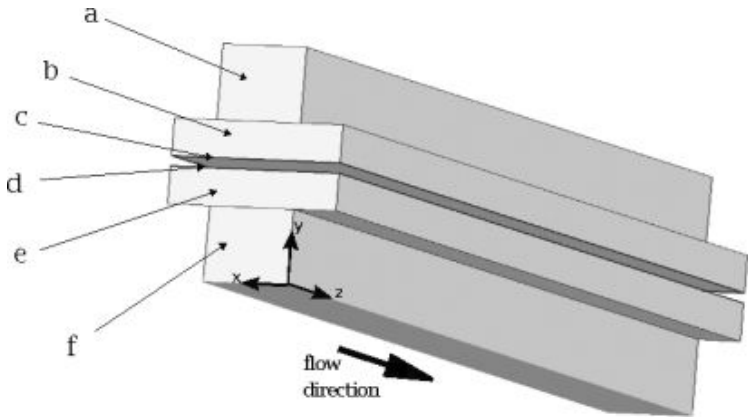

Figure 2.7 Flat-plate geometry used by Coursange, Hourri, and Hamelin (2003) where (a) and (f) are the cathode and anode flow channels respectively, (b) and (e) are the gas diffusion layers, and (c) and (d) are the catalyst layers

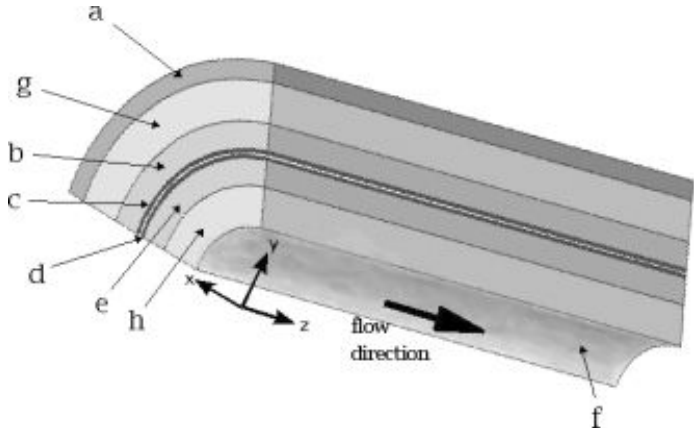

Figure 2.8 Tubular geometry used by Coursange, Hourri, and Hamelin (2003). where (a) and (f) are the cathode and anode flow channels respectively, (b) and (e) are the gas diffusion layers, (c) and (d) are the catalyst layers, (g) and (h) are the perforated plates that act as conduction layers

A commercial flow solver (Fluent) is used to solve the model and predict current density distributions. The simulations are for both types of geometries with diffusion layers on the anode and cathode, and water transport through the membrane. As seen in Figure 2.8, the model for the tubular cell assumes thin perforated tubes as the anode and cathode conduction layers. The results of the simulations show that the tubular fuel cells have higher power densities than the conventional flat-plate design due to the lower concentration losses of the tubular cells. The lower concentration losses are due to the fact that the cathode area of the cell where most of the concentration losses occur is actually larger than the anode. Thus with a larger reaction area the concentration on the cathode side are smaller than those that would be experienced by a flat-plate cell of similar size. This can be seen in Figure 2.9 where polarization and power density curves for both geometries are shown with tubular cells with and without a perforated plate. The highest power was achieved by the cell without a perforated plate. The results show an approximate increase of 30% in maximum power density.

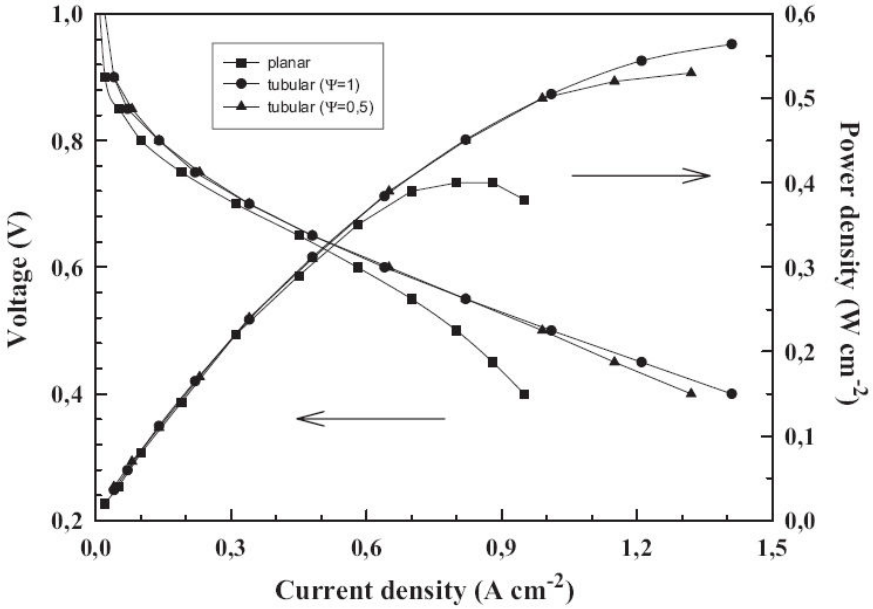

Figure 2.9 Polarization and power density curves comparing flat-plate geometry with tubular geometry with 2 different perforation ratios on the perforated tube (Coursange, Hourri, and Hamelin, 2003)

Various features were used from these models in the development of the MTFC model. The first of these is a lumped parameter model (zero-D) which uses several

relations which are developed and used in the 1-D through the thickness PEMFC model of Springer, Zawodzinski, and Gottesfeld (1991). The second is also a lumped parameter model (zero-D) which uses several of the relations from the down the channel portion of Yi and Nguyen's (1998) 2-D down the channel and through the thickness PEMFC model.

A lumped parameter model was chosen over 1-D, 2-D, and 3-D models primarily for simplicity and simulation times. The main function of the MTFC model is to find the major losses associated with MTFCs currently being produced. Once these losses are identified processing and design changes to the MTFCs can be made to improve performance. Therefore the higher resolutions provided by 1-D, 2-D, and 3-D models is not needed at this stage of research. It is also expected that the MTFC model will eventually be enclosed in a full system model with a MTFC stack. A larger 1-D, 2-D, or 3-D model would require much longer simulation times, which could potentially create problems in the evaluation of a full system model with several MTFCs.

The experimental results and the design and fabrication techniques of PEMFCs and DMFCs found in the literature will be discussed next. These are of great interest to the work performed in this research.

2.3 Experimental Data and Design and Fabrication Techniques for PEMFCs and DMFCs

There are copious amounts of information on fabricatin techniques and experimental data for PEMFCs and DMFCs. However, only the present research is

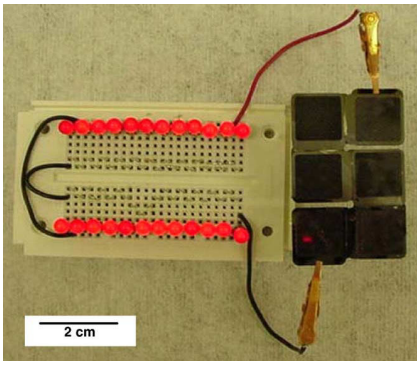

Figure 2.10 Six micro-MEAs, developed by Yeom et al. (2005), operating an array of LED lights using formic acid as the fuel.

presented here. For example the paper by Yeom,et al. (2005) details the techniques used to fabricate a millimeter scale flat-plate PEMFC that can also be used as a DMFC. Test results for various fuels using the same cell are presented. Figure 2.10 shows six assembled micro-MEAs, using a 10 molar (38.36% formic acid by volume) solution of formic acid as the fuel, lighting up an array of LED lights.

Fabrication of the cell is accomplished through use of a silicon wafer which effectively acts as the bipolar plate (flat-plate geometry). Etching of the silicon wafer was used to produce the silicon electrode structure. The etching process is very similar to the process currently used to create computer processors. Figure 2.11 shows four images of the etched silicon at various magnifications.

A number of tests were conducted by Yeom et al. in order to determine the performance of the micro-fuel cells using different fuels. It was found that hydrogen yields the best performance with an open circuit voltage of greater than 0.9 V and a maximum power density of about 35 mW/cm^2 (see Figure 2.12). The next best performance is that of formic acid (10 molar solution, 38.36% formic acid by volume) with an open circuit of 0.6 V, which is a decrease of about 33% of the open circuit voltage attained by the hydrogen cell. The maximum power density of the formic acid was about 16 mW/cm^2 (see Figure 2.13) which is close to 46% of that attained by hydrogen. Methanol (1.25 molar solution, 5% methanol by volume) produced the worst results with an open circuit of only 0.4 V, which is a decrease of 65% from the open circuit voltage attained by the hydrogen cell, and a maximum power density of about 0.38 mW/cm^2 (see Figure 2.14) which is only about 1% of that attained by hydrogen. These

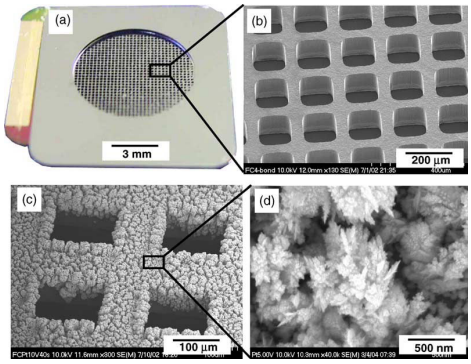

Figure 2.11 Images of the MEA bonded with the silicon electrode which is shown at different magnifications (Yeom et al. 2005)

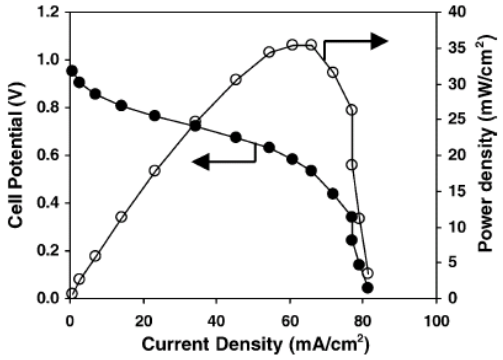

Figure 2.12 Polarization and power curves for the cell using hydrogen as fuel (Yeom et al., 2005).

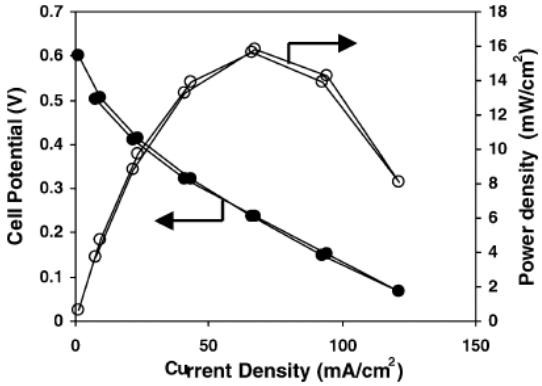

Figure 2.13 Polarization and power curves for the cell using formic acid as fuel (Yeom et al., 2005).

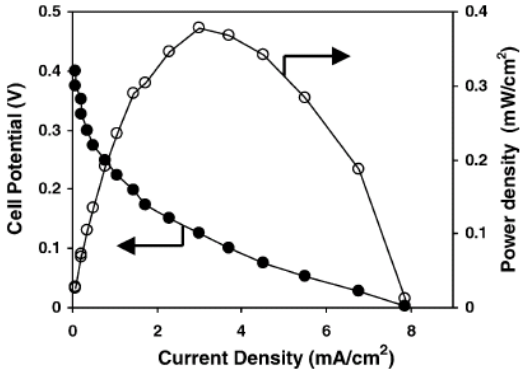

Figure 2.14 Polarization and power curves for the cell using methanol as fuel (Yeom et al., 2005).

results are used as a part of the feasibility study presented in Chapter 3 in which the polarization and power curves generated by Yeom et al. are used to determine the

efficiencies of power production between the hydrogen, methanol and formic acid micro-fuel cells.

A DMFC design proposed by Mench et al. (2001) uses gravitational, capillary, thermal, and solutal buoyancy forces to passively supply reactants to the cell. The authors estimate a power density of about 1 W/cm^3 for a cell with a total volume of 1 cm^3. Using this design the stack mass and volume were calculated for use in the feasibility study for systems which include the stack and fuel source volumes in the total system volume (this is explained in detail in Chapter 3). Actual performance results for this cell have not been made available by the authors.

Green, Slee, and Lakeman (2002) present a novel lightweight tubular PEMFC design in the article entitled as well as performance results with various configurations. Figure 2.15 shows a longitudinal cross-section of the design, also the electrolyte and catalyst layers are shown between cathode and anode conduction layers, which are

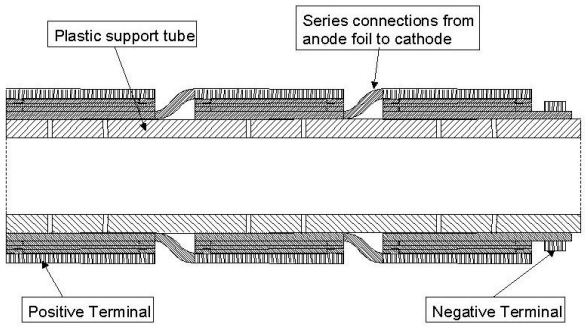

Figure 2.15 Three cell lightweight PEMFC stack of tubular design proposed by Green, Slee and Lakeman (2002)

shown connected in series, but the authors do not note these different layers in Figure 2.15. These layers are shown in more detail in Figure 2.16 below. The fabrication method proposed uses a flat-plate type MEA which is wrapped and secured around a perforated stainless steel tube. Figure 2.18 shows a cut away drawing of a single tubular cell. Both the steel anode and cathode collectors shown in Figure 2.16 are perforated to allow passage of reactants to the membrane. The carbon cloth gas diffusion layers shown in Figure 2.16 are necessary in this tubular design because of the perforated collectors.

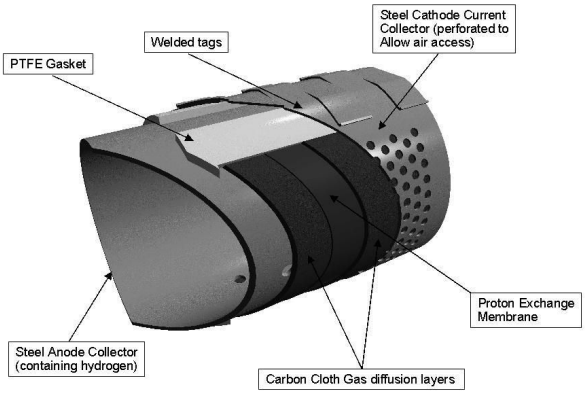

Figure 2.16 Single cell cut away drawing of Green Green, Slee, and Lakeman (2002) design

The diameter and number of perforations of the perforated steel tube on both the anode and cathode sides are studied. It is found that the optimal configuration for maximum power production for this design includes holes of 1.5 mm diameter and 14 total holes per cell on the anode. Figure 2.17 shows the effects of anode hole diameters and hole frequency. The effects of cathode hole diameters on cell performance

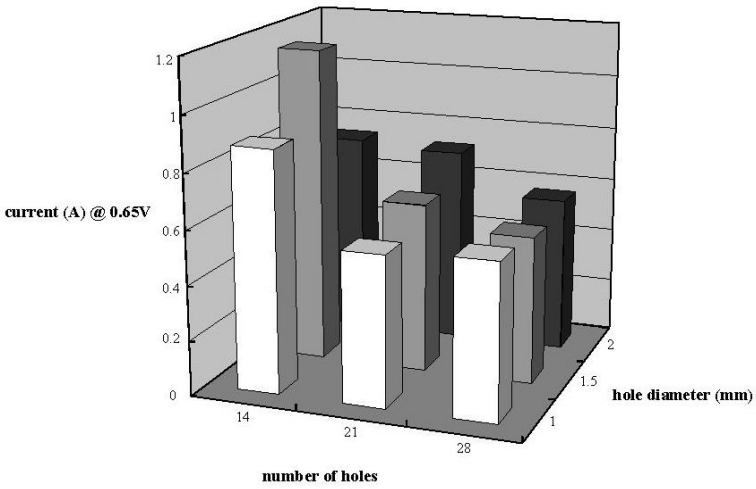

Figure 2.17 Effect of anode hole diameters and hole frequency on cell performance (Green, Slee, and Lakeman, 2002).

are shown in Figure 2.18 for two diameters, i.e. 1.056 mm and 0.798 mm. It can be seen that overall performance is improved by increasing the diameters of holes on the cathode. No testing conditions were given by the authors for the tests in Figure 2.18. The authors do not give sufficient information to determine an optimum cathode hole diameter as was

done for the anode hole diameter in Figure 2.17. The tubular cell performance reported by the authors cannot be compared with results received in this project because the active area of their tested cells is not given so that current and power densities cannot be calculated.

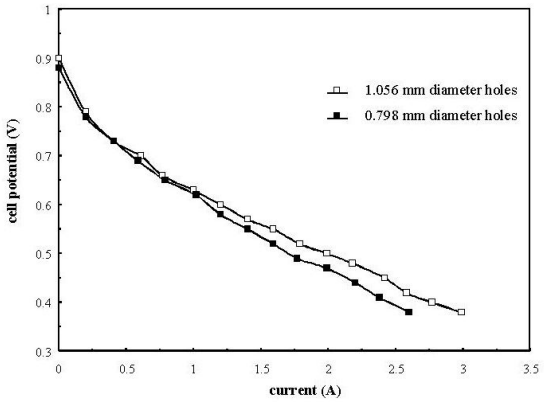

Figure 2.18 Effect of cathode hole diameter and number on cell performance by Kimble et al (2000), reprinted by permission of the American Institue of Aeronautics and Astronautics, Inc..

Another tubular design is that presented by Kimble et al (2000). This design uses micro-tubular PEMFC cells and shows methods for using them in arrays. The overall performance of these cells and arrays is determined through experiments. Also discussed is the effect of tube diameter on power density. Figure 2.19 shows a schematic of the design used by the authors. The separator shown in Figure 2.19 is the electrolyte. The

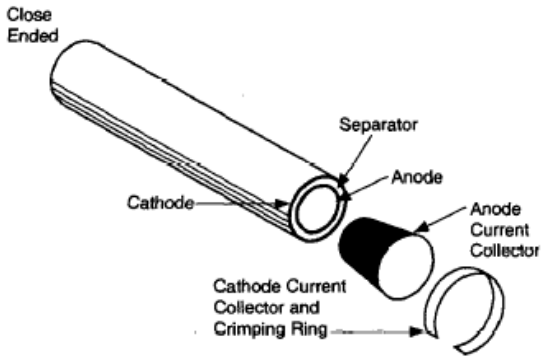

Figure 2.19 Schematic of a single micro-tubular cell (Kimble et al., 2000), reprinted by permission of the American Institue of Aeronautics and Astronautics, Inc.

authors show that these cells can be mounted in a manifold configuration to create a stack of cells. Figure 2.20 is schematic of how these cells would be mounted into the manifold

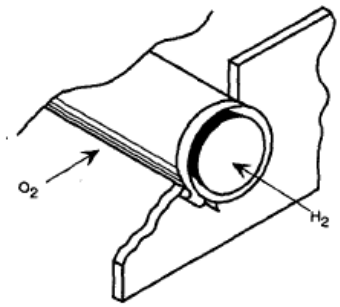

Figure 2.20 Schematic of the single micro-tubular cell design mounted in the manifold configuration (Kimble et al., 2000, reprinted by permission of the American Institue of Aeronautics and Astronautics, Inc.).

configuration. Typical manifold configuration (as viewed from the end) is shown in Figure 2.21. This configuration is similar to the diamond configuration which is discussed in Section 3.4 of the next chapter.

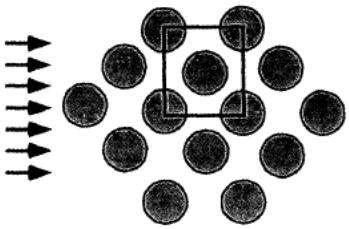

Figure 2.21 Staggered array pattern used to model flow over a 14 tube MEA array (Kimble et al., 2000, reprinted by permission of the American Institue of Aeronautics and Astronautics, Inc.).

The authors use a computational fluid dynamics (CFD) flow solver, Compact 2-D Version 4.0, to find the flow around an array of tubular MEAs. The authors found that a spacing of 0.51 mm between cells, which are modeled as cylinders, yielded good flow through the array, but if the spacing is smaller then 0.51 mm than the gas flow effectively goes around the array instead of through it. Poor flow through the array would cause poor cell performance because oxygen would not be readily available to the cells in the interior of the array. The authors did not explicitly state the type of CFD method (i.e. finite element, finite difference, or finite volume) used to evaluate the array. Individual cell

performance is shown to improve with design iterations by varying the catalyst and electrode structures. Figure 2.22 shows the effect of these iterations

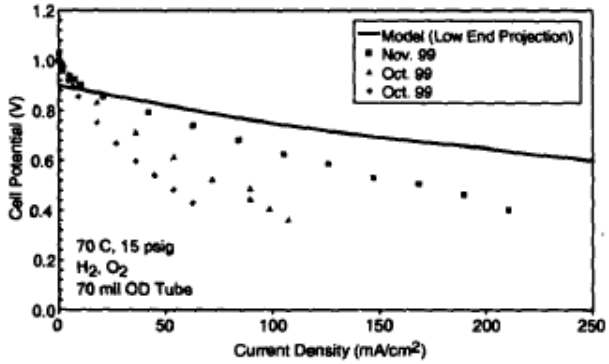

Figure 2.22 Single cell polarization showing design iteration improvements taken at 70°C, 15 psig H_2 and O_2 as reactants (Kimble et al. 2000, reprinted by permission of the American Institue of Aeronautics and Astronautics, Inc.).

on the polarization curve produced by a single cell. The volumetric power density (W/cm^3) and mass energy density (W/kg) was found to peak when the inner diameter of the cell is close to 25 mil, which is approximately equal to 0.635 mm. Figures 2.23 and 2.26 show the range of effects of changing the inner diameter on volumetric power

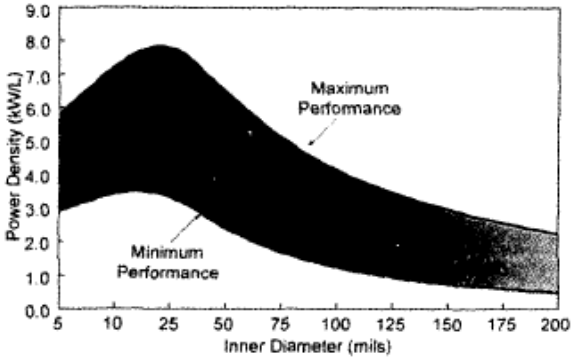

Figure 2.23 Effect of inner diameter on cell volumetric power density for a single cell (Kimble et al., 2000 reprinted by permission of the American Institue of Aeronautics and Astronautics, Inc.).

density and mass energy density. The range is given from experimental data and the upper limit is from a model made by the authors to predict performance of the cells. The authors do not give conditions for the data portrayed in Figures 2.23 and 2.24 beyond the

range of inner diameters used. Larger inner diameters in the cells also indicate thicker cell walls, thicker cell walls would cause more losses in proton conduction and thus larger cells would have lower volumetric and mass power densities. It is unclear from the data given why smaller diameter cells produce poorer results than those cells in the around 0.635 mm.

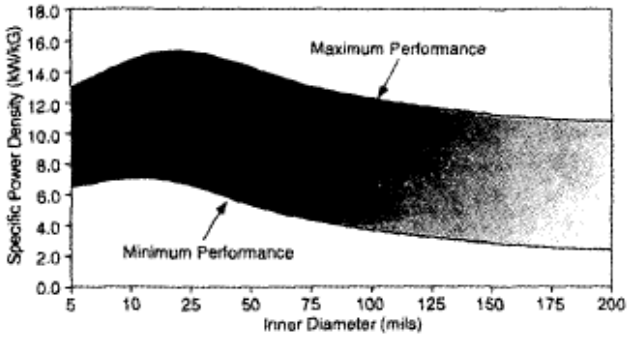

Figure 2.24 Effect of inner diameter on cell mass power density for a single cell (Kimble et al., 2000 reprinted by permission of the American Institue of Aeronautics and Astronautics, Inc.).

Eshraghi et al. (2005) have developed a number of methods for constructing micro-tubular hydrogen and methanol cells for which they have applied for a patent. The patent application records the methods of construction as well as performance data from cells made using the same construction methods. Eshraghi et al. use an extruded Nafion™ membrane tube which is then coated with a catalyst layer inside and outside the tube to

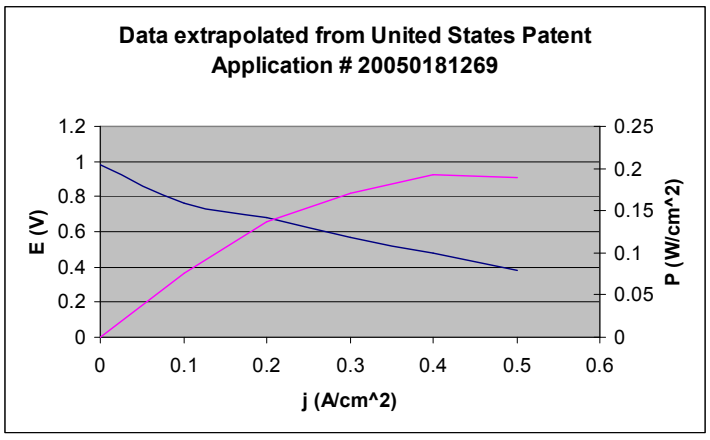

Figure 2.25 Data extrapolated from United States Patent Application # 2005181269 produced by Eshraghi et al. (2005)

form the MEA, followed by conduction collectors (wires) are applied tangentially along the tube on the inside and outside of the MEA. Figure 2.25 shows a polarization curve which was extrapolated from the patent application. This data is 3 times smaller than the data estimated by Coursange et al. This could be due to the different construction used by

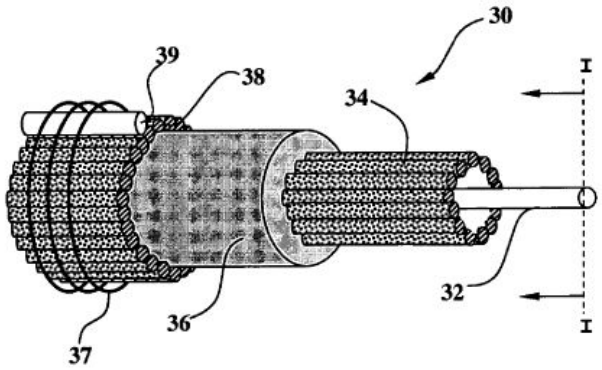

Figure 2.26 Schematic of cell fromUnited States Patent Application # 2005181269 produced by Eshraghi et al. (2005)

Coursange et al. in their modeling. The data from Eshraghi et al. is compared later in Chapter 6 with results from the MTFC model along with results from Coursange et al. Figure 2.26 is a schematic of the Eshraghi et al. design where #30 is the overall cell, #32 #39, and #37 are conduction layers, #34 and #38 are the anode and catalyst layers, and #36 is the membrane.

The next chapter explains the feasibility of using several fuel cell types, geometries, and cell arrangements for use in MAV applications using various performance criteria (i.e. energy, volumetric energy density, and mass energy density) to establish the most promising fuel cell configurations for the application

Chapter 3

Analytical and Numerical Feasibility Model

Phase I of this research involves a feasibility study with respect to various options for powering MAVs. Currently the MAVs used by the Air Force are powered only by battery technology. In an effort to increase MAV ranges and mission times, Air Force Solicitation F061-144-0607 (Topic # AF06-144) was created to fund the development of fuel cells with the intent of replacing the batteries used by MAVs. In particular the MAV of interest to the Air Force has a battery compartment with a volume that has dimensions

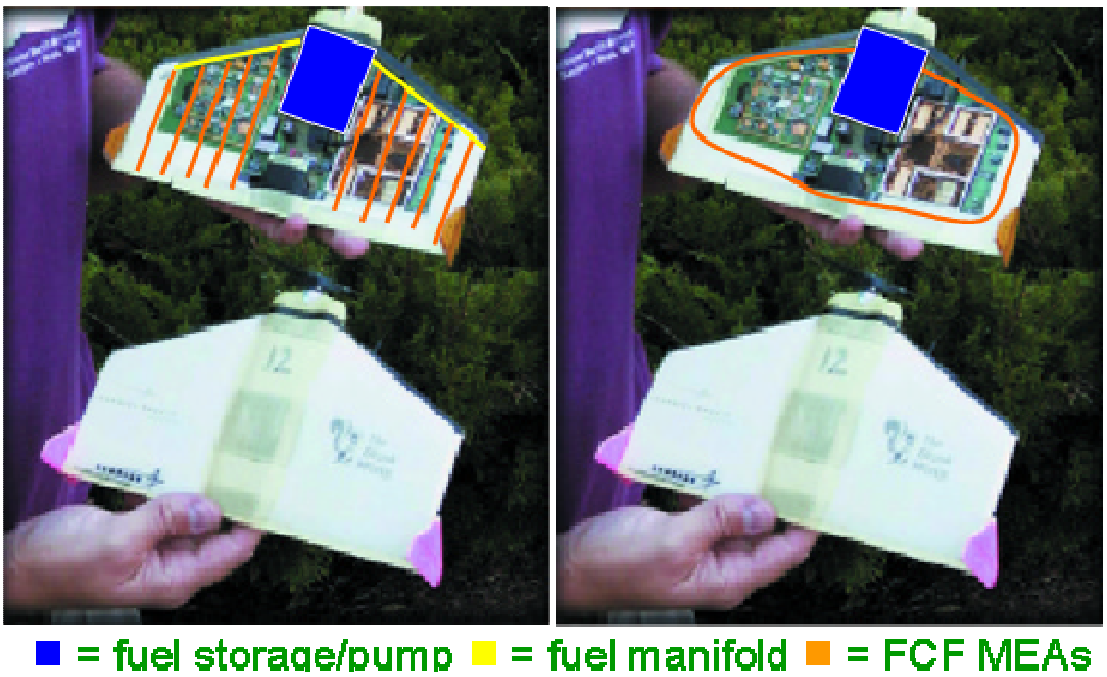

Figure 3.1 MAV showing two different configurations of MTFCs being distributed throughout the fuselage (Gunter, 2007, Phase I Final Report)

of 4 in by 1.25 in by 0.625 in. A current draw of 2 Amps and a voltage of 12 volts are the minimum requirements for the fuel cell system as given by the Air Force. Figure 3.1 superimposes the volume for the tank to power a fuel cell in a MAV over the current battery. It also shows two different configurations of distributing MTFCs throughout the fuselage. This feasibility study focuses on showing the potential of different fuel cell

configurations and types for powering the MAV of interest. The study focuses on fuel cell systems that are completely contained within the space currently allotted by the Air Force for the batteries as well as on MTFCs that could be dispersed throughout the fuselage (see Figure 3.1), saving the space currently occupied by the battery for fuel storage.

To compare fuel cells with existing battery technologies the potential of different fuel cell types and configurations as MAV power plants, several important criteria are used. The most important are the total energy generation capability, the mass energy density, and the volumetric energy density. The first of these is important because it gives the total amount of energy that the power plant is capable of producing on a single tank of fuel, which is important, for determining the maximum range of the MAV. The mass energy density shows how weight efficient the system is, which is an important factor in aircraft design and loading. Volume energy density gives a gauge of the space efficiency of the system. The higher the space efficiency is the smaller the MAV can be designed, making transportation easier.

The first feasibility calculations made are those which roughly determine the potential when compared to battery technologies of different types of fuel cell systems for fulfilling the requirements outlined above. Assuming initially that the entire fuel cell stack is housed outside of the specified volume (4 in x 1.25 in x 0.625 in) and that this volume is used only for a fuel tank, one can determine the theoretical maximum energy that each system would be able to achieve. The point of doing this is to eliminate at the

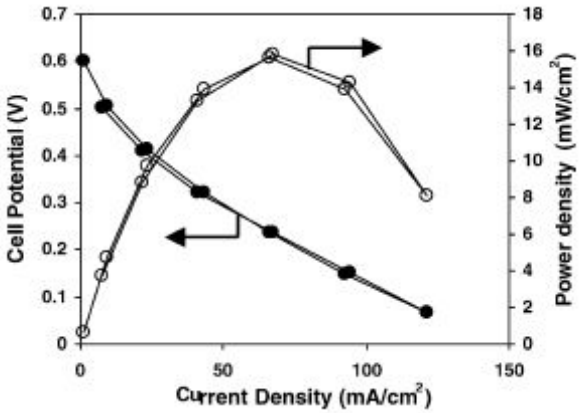

Figure 3.2 Polarization and power curves for a direct formic acid fuel cell (Yeom et al., 2005).

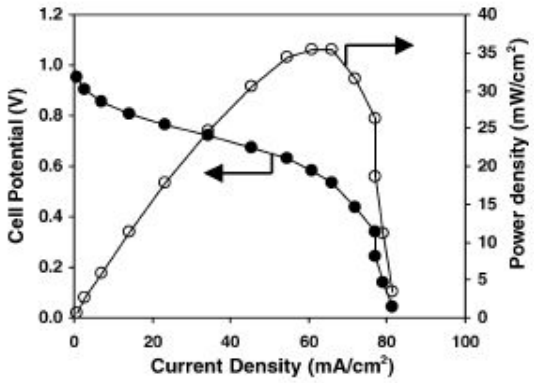

Figure 3.3 Polarization and power curves for a hydrogen PEMFC (Yeom et al., 2005).

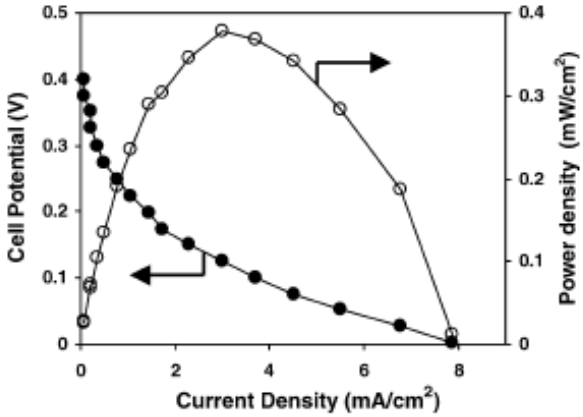

Figure 3.4 Polarization and power curves for a direct methanol fuel (Yeom et al., 2005).

outset those fuel cell technologies which with such a lenient (and yes, unrealistic) scenario cannot meet the requirements set by the Air Force or even if able to meet the requirements exhibit, nonetheless worse performance than that of the best battery technology. The efficiencies for the different fuel cell systems considered are based on the performance curves given in Figures 3.2 to 3.4, which are taken from Yeom et al. (2005) for the flat plate MTFCs depicted in Figure 2.10 of Chapter 2. These figures show polarization and power curves for methanol (MeOH), formic acid (HCOOH), and hydrogen (H_2) fuel cells using the exact same MEA. As seen in these figures, the DFAFC peak power production is only about 50% of the peak power produced by the PEMFC while for the DMFC it is only about 0.8% of the power produced by the PEMFC. The volume of the hydrogen tank is calculated assuming that the tank is a small carbon fiber wrapped composite cylindrical pressure vessels which are scaled down from information given in Vielstich, Lamm, and Gastiger (2003). The volumes of the methanol and formic

acid tanks are calculated assuming tanks of high density polyethylene (HDPE) with walls of 1/32 in (0.08 cm) thickness which are shaped to fit into the Air Force specified volume. Knowing the available volume and fuel properties, it is possible to calculate the number of moles of fuel in the storage space. In the case of hydrogen, the number of moles can be found using the ideal gas equation of state using the various pressures evaluated at a temperature of 298 ^{o}K. For the liquid fuels, the volume is divided by the fuel density and molecular weight to find the number of moles of fuel (liquids are assumed to be incompressible at a temperature of 318 ^{o}K. Using an assumed Faradaic efficiency value of 0.95, the change in the enthalpy of reaction, the number of moles, and

Table 3.1 Modeling details of fuel cells vs. battery feasibility study

Variable Description		Model Equation
n	# of moles (mol)	Calculated value
M	Molecular weight (kg/kmol)	Given value
m_t	Mass of tank (kg)	Calculated value
m_{fc}	Mass of fuel cell (kg)	Calculated value
Δh_o	Enthalpy of reaction (kJ/mol)	Given value
ε	Overall fuel cell efficiency	Given value
V	Volume occupied by fuel(cm^3)	Given value
φ	Voltage (v)	Given value
m_f	Mass of fuel (kg)	$m_f = nM$
m	Total mass (kg)	$m = m_f + m_t + m_{fc}$
E	Total energy (W-hr)	$E = \Delta h_o \varepsilon n$
e_m	Mass energy density (W-hr/kg)	$e_m = \frac{\Delta h_o \varepsilon n}{m} = \frac{E}{m}$
e_v	Volumetric energy density (W hr/cm^3)	$e_v = \frac{\Delta h_o \varepsilon n}{V} = \frac{E}{V}$

the cell efficiency, it is then possible to calculate the total energy that a particular type of fuel cell could produce from a single tank of fuel with the specified volume. Table 3.1 summarizes the equations and parameters used.

In the second set of feasibility calculations, a fuel cell stack (of a type not eliminated by the first set of calculations) along with a fuel storage tank is included in the volume. The individual fuel cell stack (see Figure 3.5) is based on a design proposed by

Mench et al. (2001). The design is for a flat plate passive fuel cell system which requires no pumps or fans. The methanol solution is in a reservoir on top of the cell and uses gravity and concentration gradients to passively move fuel down the edge of the individual stack into a small distribution manifold at the bottom of the stack. To

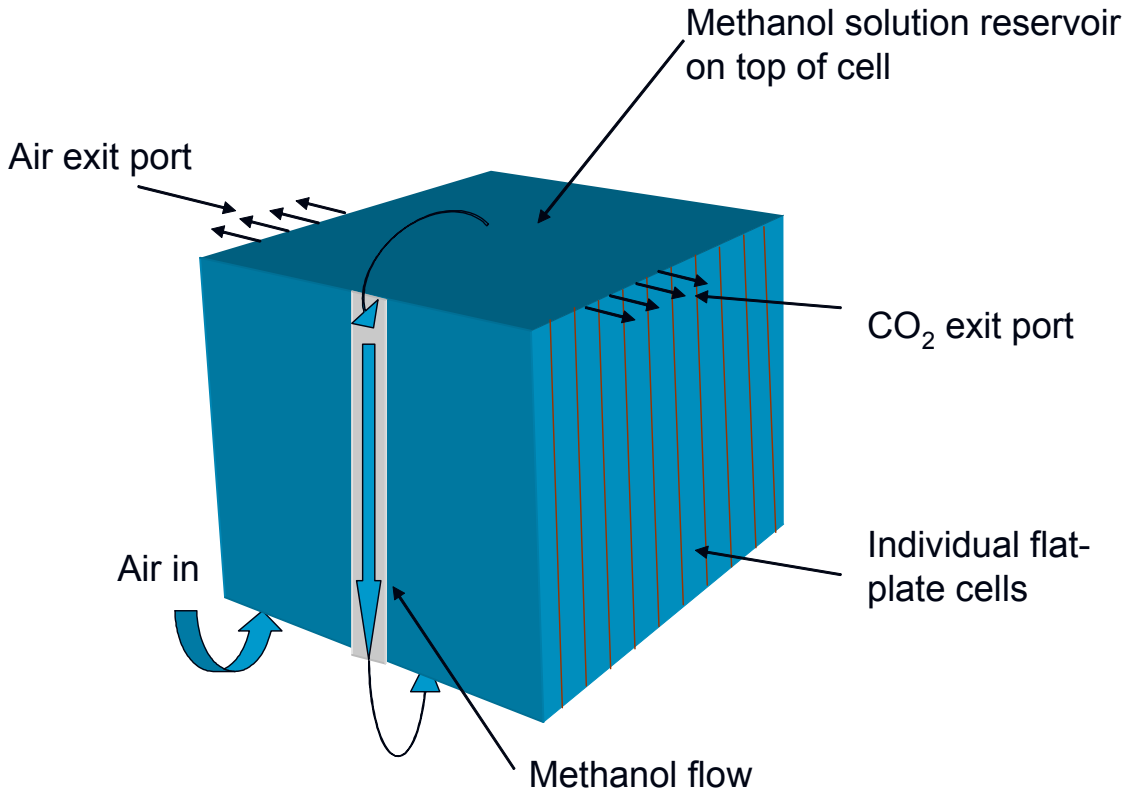

Figure 3.5 Schematic of passive DMFC proposed by Mench et al. (2001).

achieve the power required (e.g. 24 W) in the Air Force Solicitation, 24 of the individual stacks must be connected in series.

The design used for the MeOH and HCOOH fuel cell systems is based upon the neat fuel tank and wicking technology given in Guo and Cao (2004). As seen in Figure 3.6. A neat methanol tank has a much higher power density than a mixed tank (MeOH with water) because the neat tank holds many more moles of MeOH than the mixed tank. The results of this can be seen in Figure 3.7 which shows the voltage production over time of a neat tank system and a mixed tank.

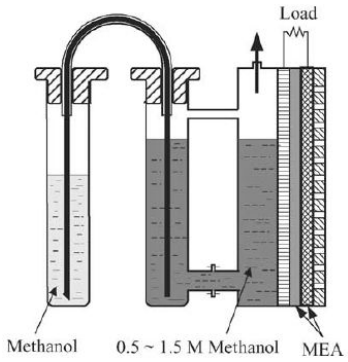

Figure 3.6 Air breathing DMFC employing wicking technology for fuel delivery (Guo and Cao ,2004).

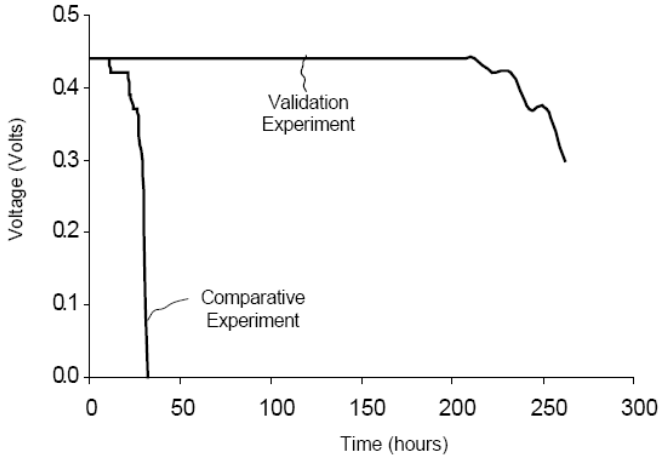

Figure 3.7 Comparison of output voltages of a DMFC using wicking (validation experiment) and a mixed tank (comparative experiment) (Guo and Cao ,2004).

These different types of fuel cell technologies are described in more detail below. Also discussed is a method for comparing the power density, volumetric density, and mass energy density of flat plate and tubular PEMFCs.

3.1 Battery technologies

As a basis for comparison with the fuel cell technologies considered, several types of the newer battery technologies are also examined such as lithium polymer ion, nickel metal hydride, nickel cadmium, and zinc oxide. All of these types fit the general requirements given for MAV power plants except the for zinc oxide battery. The zinc oxide battery performs very well with a high energy capacity, and high mass and

volumetric energy densities, but it is also non-rechargeable, and, thus, does not fit the general Air Force requirements for MAV power plants. Information on the different battery systems evaluated is found at Batteryspace.com, (2006) for the lithium polymer ion, nickel metal hydride, and nickel cadmium batteries; from Thunder Power Batteries, (2006) for the Thunder Power I lithium polymer ion battery; from power one (2006) for zinc oxide battery; and from private communications with the AFOSR program manager, Lt. Crosby, for the Thunder Power II lithium polymer ion battery (2006). Lithium polymer ion batteries are lightweight (about 175 W-hr/ kg for Thunder Power II), have a low self discharge rate and essentially do not have a charging memory. Battery charging memory is a decrease in performance over time because the electrolyte is adversely affected by incomplete charges and discharges. Nickel metal hydride batteries have the second highest mass energy density for the rechargeable batteries at 78 W-hr/kg, they have a higher self discharge rate than lithium polymer ion batteries, and have a slight charging memory. Nickel cadmium batteries have the lowest mass energy density for rechargeable batteries at only 60 W-hr/kg, the highest self discharge rate for rechargeable batteries, and experience high charging memory. Zinc oxides have the highest mass energy density (556.62 W-hr/kg), virtually no self discharge rate, and since they are not rechargeable the charging memory does not apply to them.

3.2 Fuel Cell Technologies

The three types of fuel cell systems evaluated are:

- Active
- Passive
- Passive with wicking technology

All of the hydrogen systems evaluated are active systems. Active systems use pressure as the driving force of the fuel to the anode and they also may use pressure as the driving force of the air on the cathode side. Active systems can be pressurized via several methods. One way is to use a pressurized fuel tank as depicted in Figure 3.8 (Ames et al., 2006), a method typical of many hydrogen storage applications. Pressurized hydrogen tanks generally have the form of cylindrical pressure vessels. Another approach

is to store the hydrogen in sodium borohydride systems (i.e. a chemical hydride system), which during exothermic chemical reactions release hydrogen and supply the hydrogen at a pressure sufficiently elevated to drive it to the anode. The form of sodium borohydride systems is variable depending on the system size and volume constraints. Generally they have a box type shape.

On the cathode side fans are often used as a source of pressurization for the air in active systems. Active systems also have better fuel cell and system efficiencies than

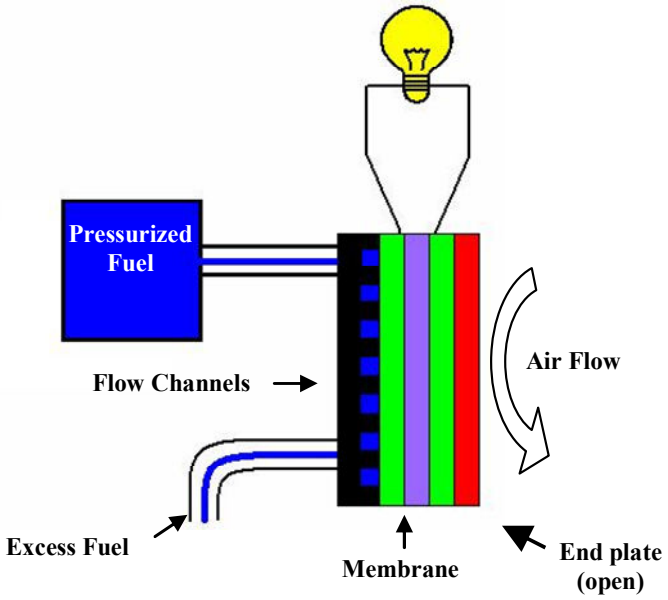

Figure 3.8 Active fuel cell design (Ames et al., 2006).

those of passive systems but are not the most space efficient because they require additional equipment to create and/or control the pressure for the driving forces. This equipment also requires a power source, resulting in parasitic losses and results in greater system complexity which has implications both for maintenance and reliability.

A passive system such as the one depicted in Figure 3.9 (Ames et al., 2006) is one where the driving force of the fuel to the anode is from either a concentration gradient or from gravity, with some systems using both methods. Figure 3.10 (Ames et al, 2006) shows a passive tubular fuel cell with the fuel being driven by a concentration gradient. The flat

plate design proposed by Mench et al., (2001) uses both methods. It is gravity fed but also uses a concentration gradient.

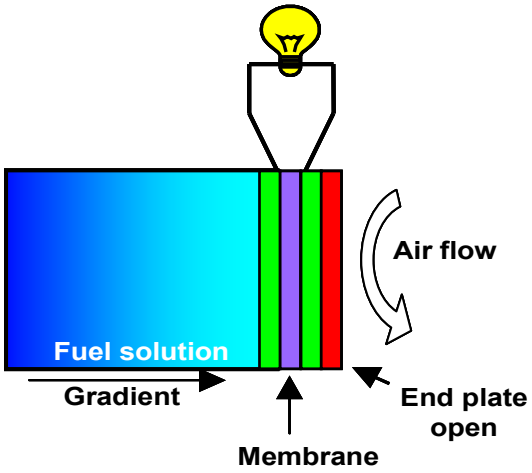

Figure 3.9 Passive flat-plate fuel cell (Ames et al., 2006).

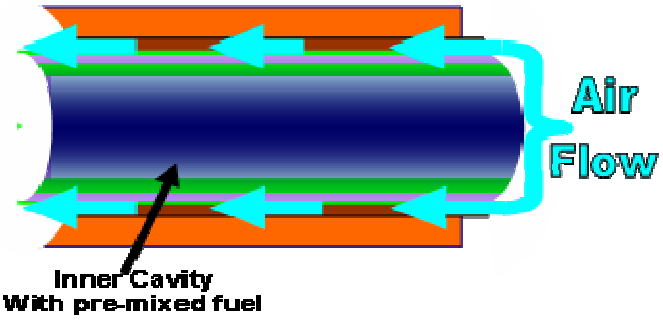

Figure 3.10 Passive tubular fuel cell (Ames et al., 2006).

In general passive systems are less efficient than active systems because the associated driving forces associated are usually much smaller. Although passive systems have lower efficiencies they are much simpler and require little if any additional equipment outside of the fuel cell stack and tank.

Passive systems with wicking technology make use of concentration gradients by use of a tank with concentrated fuel, a wick, and a pinch valve. Figure 3.11 (Ames et al., 2006) shows how these components are used together. The wick draws fuel from the concentrated fuel tank by use of differences in surface tension between the water and methanol. Water has a high surface tension while that for methanol is comparatively low. This means that methanol will "wet" a surface more than water. Methanol, thus, wets the

wicking material much more than the water so that the velocity of methanol in the wick is

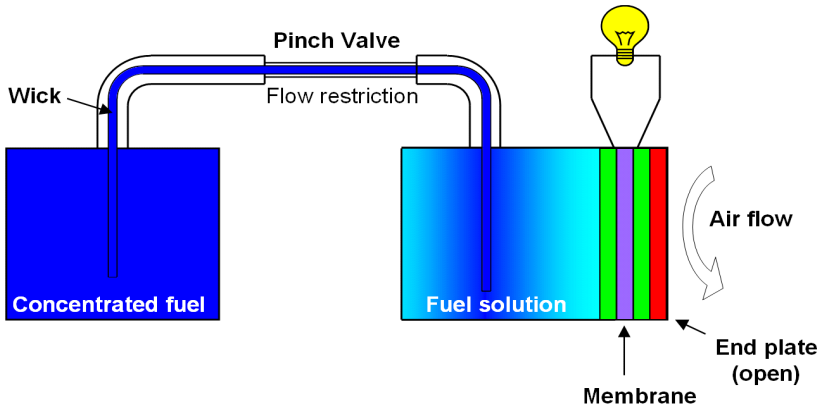

Figure 3.11 Passive flat-plate fuel cell with wicking (Ames et al., 2006).

higher than that for water (Guo and Cao, 2004). This means that the methanol reaches the top portion of the wick first and accelerates by gravity into the tank containing the water-methanol solution. The amount actually transferred is dependent upon the concentration gradient, with a pinch valve used to restrict the volumetric flow of methanol into the water-methanol tank next to the anode. Passive systems with wicking technology have the same generating efficiency as passive systems but can store highly concentrated amounts of fuel which provide significantly more energy to the system than the pre-mixed, water-methanol solutions used in passive systems without wicking. This results in higher volumetric energy densities for the former as well as greater total energy production.

3.3 Comparisons Between Different Fuel Cell Geometries

As an alternative to the flate plate fuel cell geometry a micro-tubular design is also considered here. Such a design has many potential advantages for use in MAVs. While flat plate designs are rigid and would use part of the same space in the MAV that is currently occupied by the battery, the placement of micro-tubular cells is more flexible, potentially allowing them to be placed in other locations as well such as the MAV fuselage. Even if this is not possible, as will be seen by the volume and weight configuration comparisons made in Chapter 6, the micro-tubular configuration for certain

layouts has an advantage in volume and weight over that of the flat plate design. An indication of this was already seen in Chapter 2. Such an advantage would permit a larger fuel tank to be used, and, thus, possibly allow for longer missions for the MAV between refills. Given this information it is important to have a precise comparison between micro-tubular and flat plate cells to accurately determine the potential of both types of geometries for use in MAVs.

With this in mind, the volume and weight required by each cell geometry are evaluated to determine which is more suitable for application in MAVs. The diameters and thicknesses of commercially available Nafion™ tubing are given on the website of Perma Pure (Perma Pure LLC, 2007) the producer of Nafion™ tubing. The thicknesses of the catalyst and conduction layers used in calculating the volume and weight of the micro-tubular cells are 5 microns and 20 microns, respectively. Using this information one can calculate the active area of the micro-tubular fuel cells. It is also feasible to assume that eventually the efficiency of micro-tubular cells should equal or exceed that of flat plate cells based on the results of Coursange, Hourri, and Hamelin (2003) and Green, Slee, and Lakeman (2002) which show that tubular cell efficiency generally equals or exceeds flat plate cell efficiency. This means that if given equal active areas of micro-tubular and flat plate cells it is reasonable to assume there should be an equal production of energy from each. Given this information, the total length of the micro-tubular cell that would be needed to produce the energy required by the MAV can be calculated once the needed active area is known. The needed active area can be found by calculating the area of the flat plate design proposed by Mench et al., (2001) This area yields the total length of tubing needed which then can be used to find the total weight and volume of the micro-tubular fuel cell. To determine these, the weights and volumes of the tubes, fuel delivery system, and walls must also be included.

The micro-tubular design used in the comparison is created with the Nafion™ tubes standing on end between two 30 gauge stainless steel plates or tube plates, which have been punched to hold the tubes in place (see Figure 3.12). The outermost plates are the walls of the outside of the cell. The tube plates are offset from the outer walls, also 30 gauge stainless steel, to allow the flow of reactants (fuel) and products to enter and exit the tubes. Also, because there are several methods of arranging the tubes, this changes the

volumetric, weight, and energy generation efficiency of the cell. The arrangement can be changed by altering the pattern that the tubes are positioned in as well as varying the

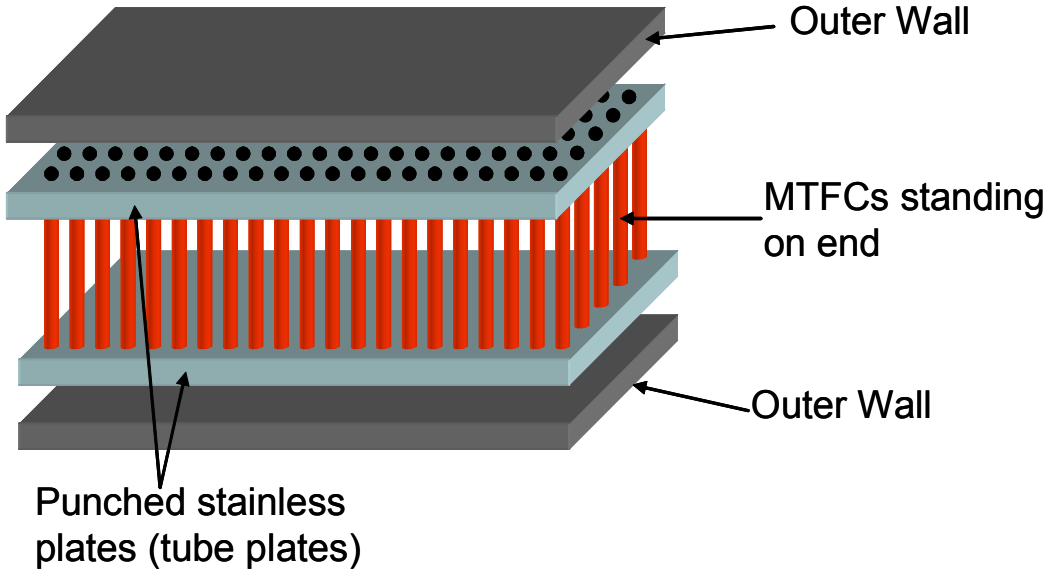

Figure 3.12 Micro-tubular stack design with the MTFCs standing on end between two punched stainless steel plates

distance from the center of one tube to the next, called the pitch. The two patterns investigated are the square and diamond as shown in Figure 3.13. In the square pattern, all of the tubes are in a grid formation and are separated by a specified pitch, P as seen in

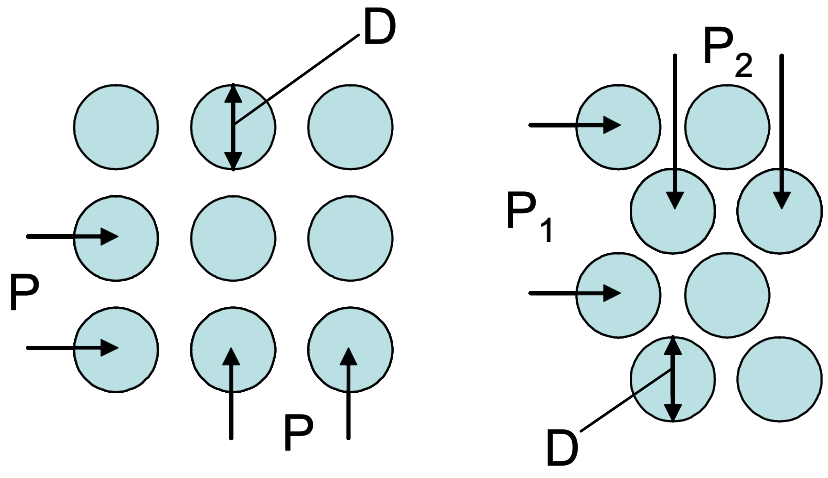

Figure 3.13 Schematic of square and diamond patterns

Figure 3.13. The diamond pattern is similar to the square pattern except every other row of tubes is offset by a specified pitch, P_1 in Figure 3.13, while the columns are separated by a different pitch, P_2 in Figure 3.13. To maximize the volumetric and weight efficiencies, the pitch should be minimized, but to maximize the energy generation efficiency, the distance between the tubes must be sufficient to allow for sufficient air flow between the tubes.

In the calculations, 5 different sizes of Nafion™ tubing are used in the setup shown in Figure 3.13 and are compared in weight and volume to the flat plate system described by Mench et al., (2001). The calculations include the thicknesses of the conduction and catalyst layers on both the inside and the outside of each micro-tubular cell. They are also done for each pattern at varying pitches beginning with a minimum pitch where each tube is in contact with the tubes next to it. The maximum height of the tubes was assumed to be 14 mm of the total 15.875 mm, to allow room for the tube plates and the outer walls. Using the fixed height and the required active area, the total volume and weight of the tubes in a specific pattern and pitch are found. The equations used are summarized in Table 3.2.

Table 3.2 Equations used to compare the performance of flat-plate cells versus MTFCs

Variable Description		Model Equation
β	Outer diameter of MTFC	$\beta = \varphi + 2(t_E + t_C)$
φ	Outer diameter of Nafion™ tubing (mm)	
t_E	Electrode thickness (mm)	
t_C	Catalyst layer thickness (mm)	
α	Inner diameter of MTFC (mm)	$\alpha = \theta 2(t_E + t_C)$
θ	Inner diameter of Nafion™ tubing (mm)	
L_T	Total tube length of active area (mm)	$L_T = \frac{A_A}{\pi\alpha}$
A_A	Active area (mm^2)	

Variable Description		Model Equation
η	Total number of tubes needed to equal the calculated active area	$\eta = \frac{L_T}{H_T}$
H_T	Height of tubes (mm)	
V_S	Total volume required (square formation) (mm^3)	$V_S = \eta(\beta P_S)^2 H_W$
P_S	Pitch (square formation) (mm)	
H_W	Height of outer walls (mm)	
V_D	Total volume required (diamond formation) (mm^3)	$V_D = \frac{\eta(\beta P_{DC})(\sqrt{3} P_{DR} \beta) H_W}{2}$
P_{DC}	Pitch of the columns (diamond formation) (mm)	
P_{DR}	Pitch of the rows (diamond formation) (mm)	
W_P	Width of tube plate (mm)	$W_P = W_W \quad t_W$
W_W	Width of outer walls (mm)	
t_W	Thickness of the outer walls (mm)	
m_P	Mass of tube plate (kg)	$m_P = t_P \quad L_P W_P \quad \frac{\pi \beta^2 \eta}{4} \quad \rho_P 2$
t_P	Thickness of tube plate (mm)	
L_P	Length of tube plate (mm)	
ρ_P	Density of the tube plate layer (gm/mm^3)	
m_w	Mass of outer walls (kg)	$m_W = t_W \rho_W \quad 2(L_P + t_W)(W_P + t_W) + 2H_W(W_P + t_W) + 2H_W(L_P + t_W)$
ρ_W	Thickness of the outer walls layer (gm/mm^3)	
m_T	Mass of tubes (kg)	$m_T = \eta H_T \frac{\pi}{4} \quad (\rho_T(\varphi^2 \quad \theta^2)) + (\rho_C([\varphi + t_E + t_C]^2 \quad [\theta + t_E]^2)) + (\rho_E([\varphi + t_E]^2 \quad [\theta]^2)) + (\rho_C(\theta^2 \quad (\theta \quad t_C)^2)) + (\rho_E((\theta \quad t_C)^2 \quad (\theta \quad t_C \quad t_E)^2))$
ρ_T	Density of the Nafion™ layer (gm/mm^3)	
ρ_E	Density of the electrode layer (gm/mm^3)	
ρ_C	Density of the catalyst layer (gm/mm^3)	
m_{TOT}	Mass of system (total) (kg)	$m_{TOT} = m_T + m_W + m_P$

3.2.1 Hydrogen

Generally touted as the future source of energy for the world, hydrogen has many advantages and disadvantages when compared with other fuels. Hydrogen fuel cell systems have some of the best overall efficiencies. There is little or no problem with catalyst poisoning by impurities or fuel crossover. However, low temperature hydrogen PEM fuel cells require hydration, which requires more equipment. An even more important disadvantage of hydrogen systems is storage. There are many different methods of storing (or creating) hydrogen, the primary ones of which are as follow:

- Cryogenic storage (at 22 °K)
- Fuel reforming
- Pressurized tanks
- Metal hydrides
- Chemical hydrides

Storing hydrogen at cryogenic temperatures is not a feasible idea with MAVs because of refueling issues and because the extremely low temperatures involved would require insulation around the tank occupying much larger volume than that allowed given. Refueling a cryogenic tank would not only be difficult in the field but also potentially hazardous. It would require carrying large heavily insulated cryogenic tanks.

Fuel reformation is also not practical for MAVs because the equipment required to reform a different fuel to hydrogen is too complex and bulky to include in the volume given. In contrast, the use of pressurized tanks of hydrogen as the fuel source for the MAV may be possible. Using current composite technology, pressurized tanks are relatively light and can withstand pressures as high as 10,000 psi. It is one of the simplest technologies used for hydrogen storage. However, pressurized hydrogen has one of the lowest energy densities of all the hydrogen storage methods. To refuel a pressurized system, a soldier would have to carry a 10,000 psi canister. This could be potentially fatal if the canister were struck by an object or exposed to an open flame or high temperatures.

Metal hydrides are metals that have been exposed to and reacted with hydrogen to form a compound in a reversible reaction. The metals are hydrogen absorbers. The

release of hydrogen from a metal hydride compound is controlled by adding heat to the hydride. The ease of this reaction makes it very appealing as a hydrogen storage option, but it is also the heaviest fuel storage option. The system needs to be sufficiently light weight for it to be feasible for use in MAVs. Another disadvantage is the required heat to release the hydrogen; this would cause a parasitic loss on the system and additional equipment causing it to be less efficient and probably not able to meet the volume constraints of the system.

Another form of hydride is the chemical hydride. Chemical hydrides are light weight and space efficient. One of the most promising types is sodium borohydride, which reacts with water to form hydrogen and borax. The reaction mechanism is given by

$$NaBH_4 + H_2O \rightarrow NaBO_2 + 4H_2. \tag{3.12}$$

Currently sodium borohydride systems are being produced for example by Millenium Cell. From their patent application (Amendola et al., 2003), the rate of hydrogen production can be found for different temperatures (see Figure 3.14). For room temperature (25 °C), the rate of hydrogen production is not sufficient to produce

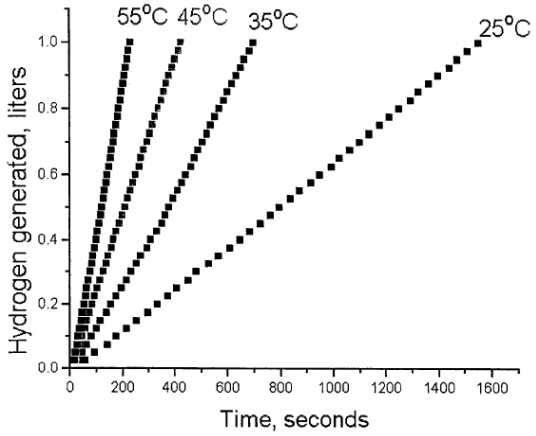

Figure 3.14 Hydrogen generation rate for sodium borohydride (Amendola et al., 2003).

the energy and power required by the Air Force. However, according to Millennium Cell, sufficient rates of hydrogen release can be achieved at temperatures between 60 °C and 90 °C. Furthermore, since the reaction to remove hydrogen from the sodium borohydride is exothermic, a parasitic source of energy for elevating the temperature is not needed.

Nonetheless, the problem with using sodium borohydride in a MAV is that it requires both water and sodium borohydride. Including the water, limits the amount of sodium borohydride that can be used, thus, limiting the amount of energy that can be stored and generated by the fuel cell.

3.2.2 Methanol (MeOH) as Fuel

Methanol is often the first choice for the replacement of hydrogen as a fuel in fuel cells. Its ease of storage, high energy density, low cost, and general availability make methanol a viable replacement for hydrogen in certain applications. Some of the main disadvantages of DMFCs include low efficiency and high fuel crossover rate and the potential for catalyst poisoning when the concentration of methanol in water gets too high. The concentration of the MeOH-water mixture at the anode is what determines the efficiency and the fuel crossover rate. The higher the concentration rate the higher the fuel crossover rate. The efficiency reaches a peak around a concentration of 3.25 molar (or 13% MeOH by volume) (Lu and Wang, 2005). Using higher concentrations than 3.25 molar results in extremely high fuel crossover which causes large drops in efficiency. The result is that the electrons for these reactions are not captured and, thus, the fuel is effectively wasted.

A method for creating a more space efficient DMFC in an effort to overcome somewhat the lower efficiency of such a fuel cell is to use wicking technology. Wicking technology provides a “bridge” between the neat fuel tank and the MeOH-water mixture on the anode side of the fuel cell. The “bridge” controls the concentration of the MeOH on the anode side of the MEA and uses the concentration gradient to move the MeOH across. Such an approach allows for 100% concentration of MeOH in the fuel storage tank while holding the concentration at the fuel cell MEA at a lower concentration. The concentration at the anode is dependent upon the material of the “bridge” as well as the pinch valve setting.

Finally, catalyst poisoning is caused by intermediate reactions of the MeOH that result in carbon monoxide (CO). Carbon monoxide reacts with the catalyst, thus, coating the catalyst and making it unavailable for the desired electrochemical reactions.

3.2.3 Formic Acid (HCOOH) as the Fuel

HCOOH is a fuel that can readily replace MeOH. Direct HCOOH fuel cells and direct methanol fuel cells are very similar because MeOH actually is oxidized to HCOOH before electrons are released. Furthermore, HCOOH does not have the same large fuel crossover problem as MeOH; and, therefore, it can have higher concentrations at the anode without significant problems. Provide that these concentrations are high enough, the direct HCOOH fuel cell can provide more energy then the direct MeOH fuel cell despite the fact that the lower heating value of the HCOOH is only about 40% that of MeOH. However, in terms of energy output when both the fuel storage using wicking technology and the fuel cell are simultaneously taken into account, the direct MeOH fuel cell provides significantly more total energy than the direct HCOOH fuel cell. As to the upper limit on concentrations, it is not clear from the literature whether the limit at which efficiency begins to decrease and degradation of the catalyst from catalyst poisoning becomes significant occurs at a 10 molar solution (38% formic acid by volume) (Yeom et al., 2006) or at a 21 molar solution (80% formic acid by volume)(Yeom et al., 2005)

3.4 Evaluations

The following are tables showing the various types of technologies (both battery and fuel cell) evaluated. Table 3.3 gives a brief description of the different battery

Table 3.3 Battery technologies evaluated

Evaluation #	Battery Technology Evaluated
1.	Lithium ion polymer
2.	Thunder Power I
3.	Thunder Power II
4.	Nickel metal hydride
5.	Nickel cadmium
6.	Zinc air

technologies that are evaluated. The evaluation number is there to keep track of the number of different systems. Table 3.4 shows the various hydrogen fuel cell systems

Table 3.4 Hydrogen PEMFC systems evaluated

Hydrogen Fuel Cell Systems Evaluated			
Evaluation #	**Type of Hydrogen Storage**	**Pressure (psi)**	**Stack included in Volume?**
7	Pressurized	5800	No
8	Pressurized	5800	Yes
9	Pressurized	10,000	No
10	Pressurized	10,000	Yes
11	Metal Hydride	n/a	No
12	Metal Hydride	n/a	Yes
13	Sodium borohydride	n/a	No
14	Sodium borohydride	n/a	Yes

evaluated. There are three types of hydrogen storage evaluated, i.e. pressurized, metal hydride, and sodium borohydride. The pressurized storage is evaluated using two different pressures as indicated. The last column indicates whether or not the stack is included in the system volumetric measurements. Cell stacks outside the volume constraints (i.e. 4 in by 1.25 in by 0.625 in) would be of a type (e.g., an MTFC stack) that is distributed throughout the fuselage of the plane.

Table 3.5 shows the configurations of DMFCs and DFAFCs evaluated. The second column indicates the fuel type of the fuel cell stack being evaluated, while the third column indicates the molarity of the fuel being used. Molarity is the number of moles of a substance per liter of solution. In the case of Table 3.5, there are two different types of solutions. The first is methanol mixed with water, and the second is formic acid mixed with water. The last column indicates whether or not the stack is included in the system volumetric measurements. For the stacks evaluated in Table 3.5, if the stack is included in the volumetric measurements, then wicking technology is assumed to be in use. If the

stack is not included in the volumetric measurements, then wicking technology is assumed not to be feasible because of the distance from the tank to the cells. If wicking

Table 3.5 DMFC and DFAFC systems evaluated.

Other Fuel Cell Systems Evaluated			
Evaluation #	**Type of Fuel**	**Molarity (moles/liter)**	**Stack included in Volume?**
15	MeOH	1.5	No
16	MeOH	1.5	Yes
17	MeOH	2.5	No
18	MeOH	2.5	Yes
19	MeOH	3.25	No
20	MeOH	3.25	Yes
21	MeOH	24.5	No
22	MeOH	24.5	Yes
23	Formic Acid	1	No
24	Formic Acid	1	Yes
25	Formic Acid	10	No
26	Formic Acid	10	Yes
27	Formic Acid	21	No
28	Formic Acid	21	Yes
29	Formic Acid	26	No
30	Formic Acid	26	Yes

technology were eventually tested and found suitable for use over longer distances such as would be used from the tank area to the stack distributed in the fuselage of the MAV then the feasibility study could be extended to include those cases. Systems 21, 22, 29, and 30 are evaluated to show the absolute maximum energy for methanol and formic acid given the volume constraints.

According to Perma Pure LLC (2007), the manufacturer of the tubular Nafion™, there are only 5 sizes of tubing available that could be used for the MTFCs. Table 3.6 gives a summary of these sizes in terms of the inside and outside diameters. The tube numbers in Table 3.6 also appear in Table 3.7 where the evaluations conducted on the micro-tubular cell and flat-plate cell configurations are evaluated to compare the weight and volume are listed. Note once more that the flat-plate geometry of Evaluation I

Table 3.6 Perma Pure LLC data on Nafion™ tubing (2007)

Tube #	Outer Diameter (mm)	Inner Diameter (mm)
1	0.838	0.635
2	1.346	1.067
3	1.6	1.321
4	1.829	1.524
5	2.743	2.184

Table 3.7 Set of evaluations for comparing system volume and weight for the flat-plate and micro-tubular stack configurations.

Evaluation	Cell Geometry	Tube #	Tube Pattern
I	Flat-Plate	n/a	n/a
II	Tubular	#1	Square
III	Tubular	#2	Square
IV	Tubular	#3	Square
V	Tubular	#4	Square
VI	Tubular	#5	Square
VII	Tubular	#1	Diamond
VIII	Tubular	#2	Diamond
IX	Tubular	#3	Diamond
X	Tubular	#4	Diamond
XI	Tubular	#5	Diamond

uses a stack design that is based upon the work of Mench et al., (2001). This same reference is also used to calculate the performance, weight, and volume of the flat-plate stack.

This feasibility study provides a detailed comparison of PEMFCs, DMFCs, and DFAFCs of both tubular and flat-plate geometries, and different cell arrangements to find the best configuration of fuel cell type and geometry. The information from this comparison is also augmented by MTFC testing data. The next chapter provides insight into the experimental setup, facilities, and equipment of said testing.

Chapter 4

Experimental Setup and Testing

A major part of this research has involved the experimental testing of individual MTFCs. The facilities and equipment used for testing are described below. The methods used for MTFC construction and the arrangement used for testing the cells are also discussed.

4.1 Testing Facilities and Equipment

All testing and evaluation of the MTFCs was performed at Virginia Tech in the Energy Systems Laboratory of the Mechanical Engineering Department. The Energy Systems Laboratory includes several pieces of equipment which can be used to assess the performance of cells.

The first of these is the Fuel Cell Technologies (FCT) fuel cell test station (see Figures 4.1 and 4.2). Table 4.1 gives a brief overview of the characteristics of the test

Table 4.1 Fuel Cell Technologies test station Characteristics

Fuel Cell Technologies Test Station Characteristics	
Characteristic	**Value or Type**
Anode Flow Rate Capacity	2000 sccm
Cathode Flow Rate Capacity	5000 sccm
Back Pressure Control	Computer Controlled
Electronic Load Capacity	150 W
Electrochemical Impedance Spectroscopy (EIS)	Integrated

station. The test station is used to control the flow of hydrogen to the anode of the fuel cell. The cathode flow rate is not controlled (although the test station has the ability to do so) because the MTFCs cathode is open to the air and does not need to be metered. The back pressure control has not been used, but can be used to pressurize the hydrogen flow

into the MTFCs. Since the electronic load of the test station does not have sufficient sensitivity to measure cell output or perform Electrochemical Impedance Spectroscopy (EIS) test on the MTFCs because of their small size and current power outputs of the

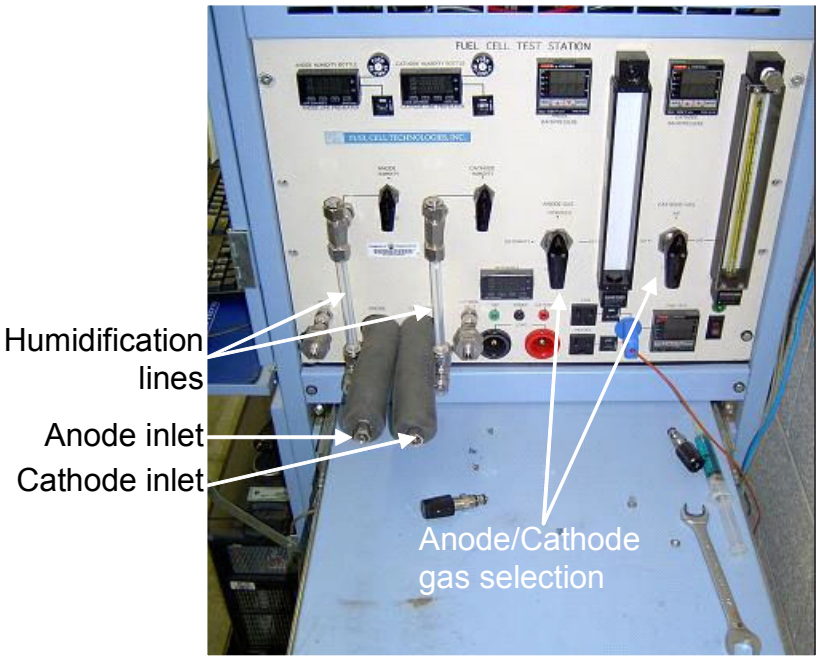

Figure 4.1 Fuel Cell Technologies test station gauges with important anode and cathode controls labeled.

Figure 4.2 Fuel Cell Technologies testing station monitor

MTFCs, an additional piece of equipment, the Solartron® Model 1480 8-channel

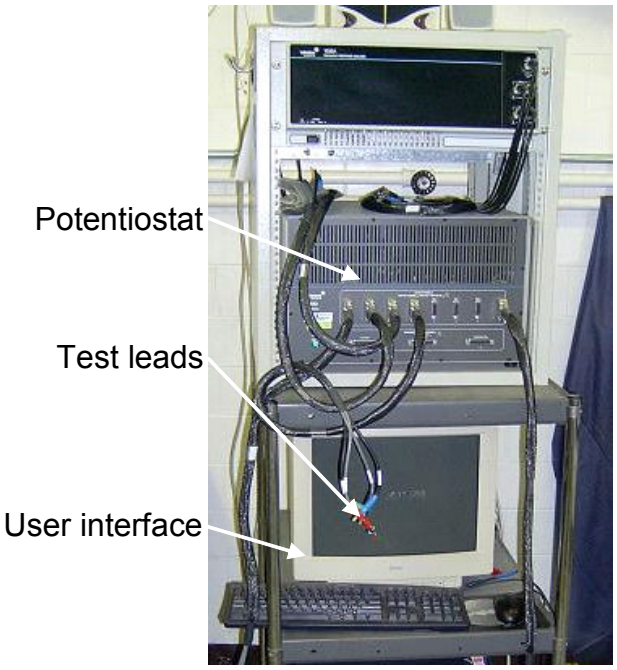

Figure 4.3 Solartron Analytical 1480 Potentiostat

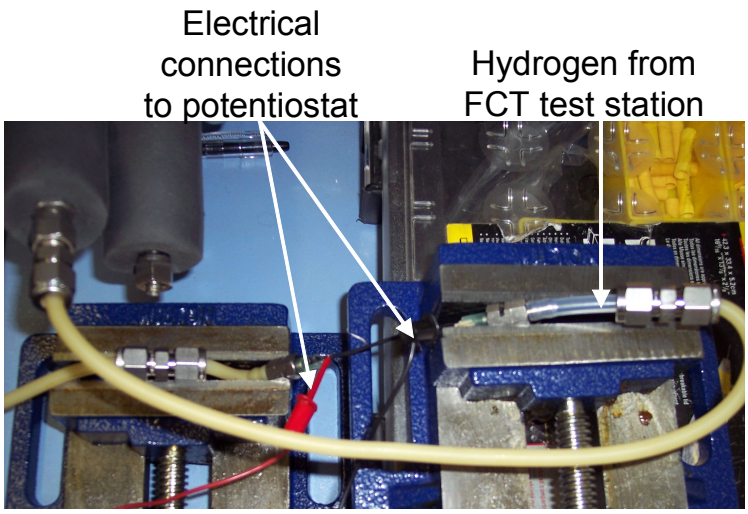

Figure 4.4 MTFC testing connections to the FCT test station and to the Solartron potentiostat

Potentiostat (see Figure 4.3) is used to measure the cell output of the MTFCs as well as conduct EIS tests. The potentiostat measures the current and voltage for the polarization curves and also the AC and DC currents used for the points on the EIS curves. Thus, in testing a MTFC, the fuel cell is connected, as shown in Figure 4.4, to the FCT test station

to control and condition (e.g., humidify) the anode flow of hydrogen as well as to the potentiostat in order to measure cell output and in a separate test, cell impedance Figure 4.4 shows the hydrogen connections from the FCT testing station to the MTFC and the electrical connections from the MTFC to the Solartron potentiostat.

4.2 Micro-Tubular Cell Construction

The traditional design for PEMFCs and DMFCs is the flat-plate geometry. The design includes bipolar plates, gas diffusion layers, a MEA, and flow channels. This is somewhat different from that of a MTFC. Figure 4.5 shows the different layers of the MTFC, while Figure 4.6 shows the axial view of the same cell. Note that the MTFC has a MEA which is similar to the flat-plate MEA although it is constructed differently, i.e. as extruded Nafion™ in cylindrical form. Figure 4.5 also shows that MTFCs have

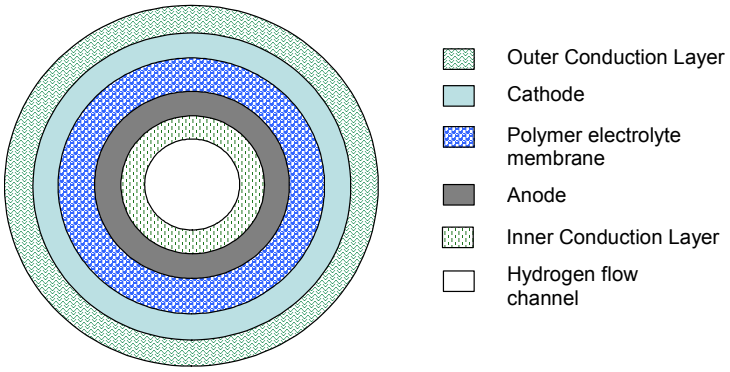

Figure 4.5 MTFC cross-sectional view

conduction layers on both the anode and cathode side perform a function (i.e. that of a current collector and conductor) similar to the mono or bipolar plates and gas diffusion layers of the flat-plate geometry. Their construction and material makeup, however, are completely different. For example the conduction layer is typically some type of metal such as tin-coated copper as opposed to the poco-graphite of the mono or bipolar plates of the flat-plate geometry cells. Furthermore, it may consist of a single axial wire or coil or a perforated tube running the length of the MTFC without flow channels machined, etched, or formed into their structure. In fact the MTFC hydrogen flow channel is simply

the interior of the micro-tube, while no constructed flow channels are used for the air on the cathode side.

In the next sections, the methods used for fabricating the tubular Nafion™ layer, for applying the catalyst, constructing the conduction layers, for channeling hydrogen into the cell, and for making the cell electrical connections are presented.

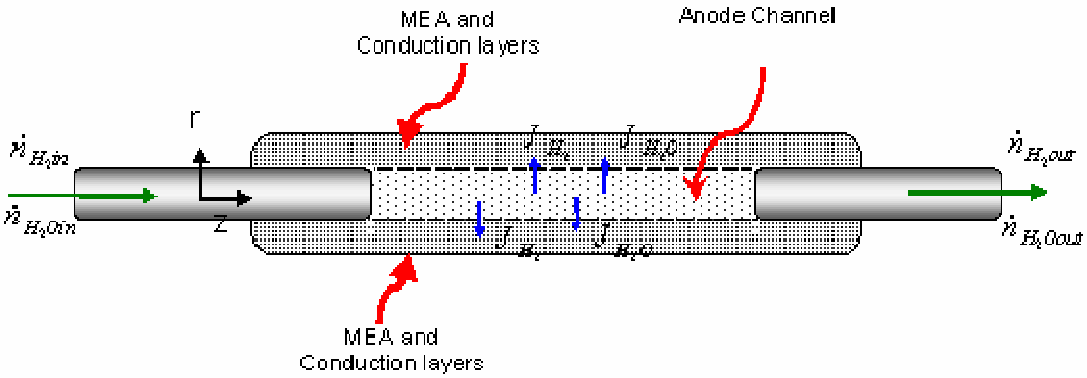

Figure 4.6 Axial view of tubular PEMFC showing flow of hydrogen and water into the cell and through the membrane and conduction layers

4.2.1 Nafion™ Layer

The polymer electrolyte membrane for MTFCs is made from a tube of Nafion™ that has been extruded. Extrusion is a process where the material is forced through a die of certain shape and it is pulled to create a long often cylindrical shape. The consequences of extruding may be that the randomness or isotropy of the proton conduction pathways may be changed to prejudice the axial direction, i.e. the conduction pathways become anisotropic, which, of course, can negatively affect the conduction of protons through the membrane from anode to cathode. After it is extruded it is subjected to sulfuric acid, which chemically activates it allowing it to react with its surroundings (Perma Pure LLC, 2007). Perma Pure LLC has an exclusive license from DuPont for manufacturing the Nafion™ tubing. Figure 4.7 shows the Nafion™ tubing as it is produced by Perma Pure LLC. Note that before any catalyst layers are applied to the surface of the membrane that the Nafion™ is clear.

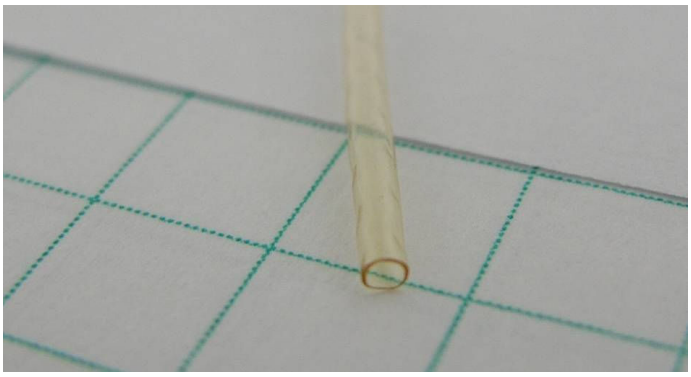

Figure 4.7 Nafion™ tubing as bought from Perma Pure LLC (Gunter, 2007, Phase I Final Report)

4.2.2 Catalyst Layers

Low temperature fuel cells such as PEMFCs, DMFCs, and DFAFCs need catalysts to speed up the rate of the electrochemical reactions which must take place in order for the fuel cell to function. A catalyst lowers the activation energy required to make an electrochemical reaction proceed in the desired direction. Catalyst layers for PEMFCs, DMFCs, and DFAFCs are usually formed by "painting" a catalyst ink onto the MEA. The catalyst ink is made up of a catalytic metal which varies by the type of fuel used by the fuel cell. For a hydrogen cell the typical catalyst is platinum while for methanol and formic acid fuel cells a platinum and ruthenium combination of equal proportions is generally used (Larminie and Dicks, 2003). The catalytic metals are deposited as nano-particles on carbon atoms which are dispersed into a Nafion™ solution. This solution is the catalyst ink that is painted onto the outside of the polymer membrane electrolyte (i.e. the Nafion™ tube). It is not possible to paint the inside of a Nafion™ tube, so for fabrication of the MTFC anode catalyst layer, an injection process is used. The injection process used involves injecting the inside of the tube with catalyst ink until it is full, then removing the excess ink by blowing nitrogen though the tube. The pressure and flow rate of the nitrogen determines the thickness of the catalyst layer which to date has been on the order of about 5 μm although future constructions may be of 10 to 15 μm. The cathode catalyst layer is produced by using a fine brush to evenly paint the ink on the cathode. After painting and injecting, the cells are heated in an oven to remove the

Table 4.2 Existing procedure for producing micro-tubular MEAs (Gunter, 2007, Private Communications)

Procedure Steps	Step #	Description
Prepare Membrane	1	Rinse Nafion™ tubing membrane in DI water and place in a clean glass beaker that has been rinsed with DI water and then filled with more DI water.
	2	Heat Nafion™ tubing membrane in DI water for 1 hour at 60^{o}C.
	3	Transfer to a 10% NaOH solution (for example, 5g NaOH in 50 mL water, scale to whatever volume needed for test piece), heat to 60^{o}C for 1 hour, and then shut-off heat and allow to cool and allow to sit overnight.
	4	Transfer to a 10% NaOH solution (for example, 5g NaOH in 50 mL water, scale to whatever volume needed for test piece), heat to 60^{o}C for 1 hour, and then shut-off heat and allow to cool and allow to sit overnight.
	5	Rinse the membrane with flowing DI water
	6	Place the membrane in more DI water and heat to 60^{o}C for 1 hr.
	7	Take-off heat and rinse with flowing DI water, store in fresh DI water
Prepare Catalyst Ink	8	Add 0.155 g of 20% Pt on CB to a small vial. Pipette 0.375 g of 20 wt% Nafion™ onto the powder with stirring. Add 1.1g ethanol to this mixture with stirring. Add 1.5g glycerin (glycerol) to this with stirring. Allow to stir for 2 hours. Place in ultrasonic bath for 1 hour.
Coat Interior Membrane	9	Using a syringe and appropriate sized needle, fill the interior of the Nafion™ tubing with catalyst ink
	10	Using a nitrogen gas line set to 20 psi, connect to a syringe need of gauge that closely matches the Nafion™ inner diameter
	11	Turn of gas flow and allow to flow until no ink drips from the end (~10 seconds)
	12	Place in the oven in air at 100-200^{o}C (varies with experiment, std has been 125^{o}C for one hour such that the uncoated side is down on a glass plate.
Coat Exterior Membrane	13	Apply a coating of the ink with an artists brush such that the surface of one side is continuously black, but not dripping or running. Wick up excess with brush.
	14	Place in the oven in air at 100-200^{o}C (varies with experiment, std has been 125^{o}C for one hour such that the uncoated side is down on a glass plate.
Convert Nafion™ to Acid Form	15	Place coated membrane in 2M H2SO4 solution and heat to 60^{o}C for 1 hour. Then cool to room temperature and allow to sit overnight.
	16	Rinse with flowing DI water, and then soak in DI water for 1-2 hours. Exchange water with fresh DI water after this time.
Hot Pressing	17	Place appropriate sized stainless steel rod inside anode of converted (to acid form) MEA
	18	Place the MEA in the machined groove in aluminum blocks, then tighten the bolts to pull plates together.
	19	Place in oven at 165^{o}C for 1 hour, then remove and allow to cool to room temperature, then remove the MEA from the aluminum blocks
	20	Place in DI water overnight to swell membrane, then remove stainless steel rod.
Applying the Silver Electrodes	21	An aqueous dispersion of silver nanoparticles is used as the ink for forming a silver conduction layer.
	22	The coating procedure matches the catalyst coating, inside first, then outside. Drying is in air at 80^{o}C for 2 hours.

glycerol used to make the catalyst ink. All of the micro-tubular MEAs used in this research have been produced by Luna Innovations, Inc. using the process described above. This method differs somewhat from the method generally used to create and adhere catalyst layers to flat-plate membranes. Flat-plate catalyst layers are prepared first on a Teflon blank which is cut to the size of the catalyst layer desired. The Teflon blank is coated with a light Teflon spray to ease removal of the catalyst layer from the blank. Next the blank is carefully painted and then weighed to insure that the correct amount of catalyst is used. Once the correct amount is obtained it is placed in a furnace to remove the glycerol in the ink. After it is dried two blanks are placed on either side of the membrane and are then hot-pressed into the Nafion™. After the hot-press process is finished, the Teflon blanks are removed and the catalyst layer is adhered to the Nafion™. This method for catalyst layer deposition has proven very successful for constructing flat-plate MEAs. However to date the method or procedure devised for the micro-tubular MEA construction has not been that successful, which method is given by Table 4.2. Work, thus, is underway by Luna Innovations, Inc. and by the Phase IX fuel cell project senior design team under the supervision of Dr. von Spakovsky to experiment with this procedure in order to produce more effective micro-tubular MEAs.

4.2.3 Conduction Layers

In a fuel cell, conduction layers are used to disperse or collect electrons. Without these conduction layers, the MTFCs would function poorly if at all. Flat-plate geometry cells use carbon fiber gas diffusion layers and bipolar plates to collect and distribute electrons that are given off or used in anode and cathode reactions. MTFCs do not have gas diffusion layers or bipolar plates, as seen in Figure 4.5 and 4.6. Instead they have separate conduction layers for both the anode and the cathode. In this research several different types of conduction layers are being used and include:

- Nanoporous silver layer (see Figure 4.8) on the anode and cathode sides
- Copper wire helically wrapped (see Figure 4.9) on the cathode side
- Singele axial copper wire (see Figure 4.10) on the anode side
- Copper mesh wrap (see Figure 4.11) on the cathode side

- No conduction layer added (see Figure 4.12) on the anode or cathode side

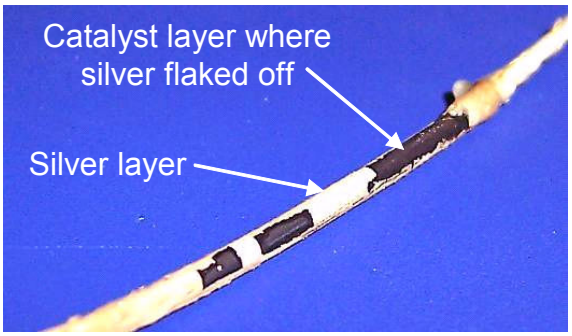

Figure 4.8 Nanoporous silver layer as conduction layer.

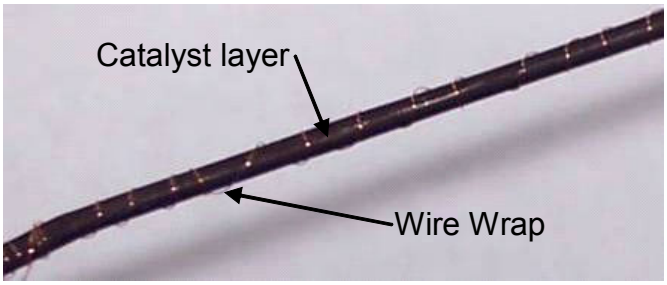

Figure 4.9 Copper wire helically wrapped as conduction layer.

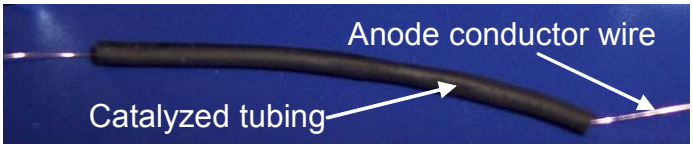

Figure 4.10 Copper wire in straight line as conduction layer.

Figure 4.11 Copper mesh wrap on the cathode side as conduction layer.

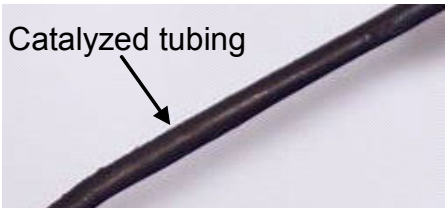

Figure 4.12 Cell with neither a conduction layer added on the anode nor on the cathode side.

The semi-porous silver conduction layers have been used on both the anode and cathode sides. Luna Innovations, Inc. produces these using nano-sized (1.0 E-9 meters) silver particles in a sintering process. By using a sintering process, Luna Innovations Inc. forms a semi-porous silver layer on the outside or inside of the catalyzed Nafion™ tubing (i.e. on the micro-tubular MEA). Figure 4.8 shows a cell with a Luna Innovation Inc. produced silver conduction layer on the cathode side.

As shown above in Figure 4.9 the copper wire helical wrap is done by hand around the cathode. The wire is wrapped around the tube while the tube is held in a vice to help ensure that the cell is stationary so a tight and uniform wrap is achieved which helps to eliminate poor contact with the MEA. To create a copper wire helical core on the anode side, a wire is wrapped around a stiff tube of smaller diameter than the catalyzed tubing to achieve the helical shape. To insert the helical core into the catalyzed tubing it is slowly pulled and massaged into place so as not to damage the catalyst layer of the anode.

Figure 4.10 shows an axial wire pulled through a catalyzed tube without bending or kinking the wire. The wire is held tight while needles for hydrogen injection are pushed into the ends of the catalyzed tubing. Thus the wire is held next to the anode wall by pressure from the needles.

The copper mesh wrap is constructed by measuring and cutting a piece of copper mesh sized to the cell being wrapped. The mesh is then carefully wrapped around the cathode of the cell and lightly crimped into place around the cathode of the cell as can be seen in Figure 4.11.

In order to test without conduction layers to determine if cell performance is impaired by the semi-porous silver layer MTFCs are also constructed without conduction layers. In these cases, the catalyst layers effectively act as conduction layers also. Figure 4.12 shows a cell with no added conduction layers on the cathode or anode sides.

4.2.4 Methods for Channeling H_2 into the MTFC

In flat-plate geometry PEMFCs hydrogen is distributed through the cell by flow channels etched into the bipolar plates. MTFCs of course have no bipolar plates. As seen

in Figure 4.5 and 4.6, the center of the MTFC acts as the hydrogen flow channel to distribute hydrogen. Luer-Lock syringe needles are used to channel the hydrogen into the

Figure 4.13 MTFC 6 with stainless steel syringe needles for hydrogen insertion

center of the MTFC (see Figure 4.13). After the insertion of the syringe needles, the MEA must be bonded to the needles to prevent leakage. Both 5 Minute Epoxy Gel (by Devcon®) and silicone SS-67A by Silicone Solutions were used as bonding agents. Initially the epoxy gel was used to bond the needles and the MEA but it was found that after soaking in water for extended periods the adhesion of the epoxy gel to the syringe needle was poor. The silicone SS-67A was produced specifically to bond well to Nafion™ with good performance even after soaking in water for extended periods. It was found that the silicone SS-67A provided better adhesion than the epoxy gel.

4.2.5 Anode Electrical Connection

The syringe needles used for hydrogen insertion also function as the anode

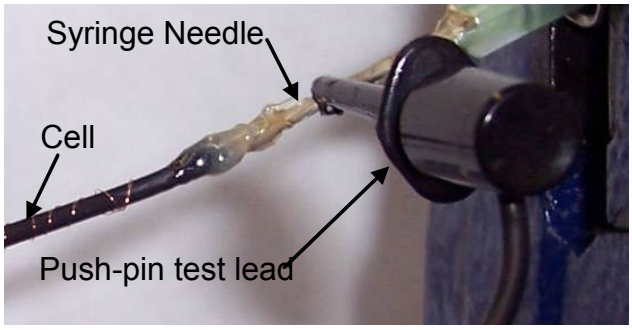

Figure 4.14 Anode electrical connection.

electrical connection (see Figure 4.14). Syringe needles were carefully sized to obtain a snug fit between the anode conduction layer and the needle surface to minimize electrical losses. For example on cell VT the syringe needles used have an outer diameter of 0.127 cm, and the inner diameter of the cell is 0.131 cm, thus a difference of only 0.004 cm between the cell and the needle. The sizing of needles to the tubing is critical because if the needle is too small then it will have a poor electrical connection with the anode, but if it is too large then it will damage the anode catalyst layer. Anode electrical connections use a small push-pin test lead (as seen in Figure 4.14) which hooks directly to the syringe needle.

4.2.6 Cathode Electrical Connection

Initially the cathode electrical connection was made by using a small push-pin type test lead similar to the one shown in Figure 4.14. The test lead needed to be attached over a portion of the MEA that was supported underneath by the syringe needle being used for channeling hydrogen on the anode side. To reduce confusing the test leads, the cathode side lead was attached to the MEA directly over the needle the farthest from the anode electrical connection (i.e. the other push pin lead). This lead has since been replaced with a thick copper wire that is wrapped at one end of the cathode. The thick copper wire provided a good connection without damaging the cathode catalyst layer, in contrast to the push pin test lead which damaged the cathode catalyst layer after being connected and disconnected many times.

4.3 Testing Setup

Controlled testing conditions during this research included a privacy curtain to maintain security, a specific cell orientation while testing, a set hydrogen flow rate, and cell conditioning.

4.3.1 Privacy Curtain

U.S. Federal Government International Traffic in Arms (ITAR) regulations prohibits any person that does not have United States citizenship or permanent residency from accessing export controlled information. All of the research conducted here as part of my M.S. thesis after May 2007 is ITAR restricted. Thus since the fuel cell testing equipment is situated in an area open to persons not involved in this research , a security screen (see Figure 4.15) has been constructed for use during testing in order to block access to the test which are always manned by authorized personnel or conducted during times when unauthorized persons are not in the lab. Upon completion of the tests, the screen is removed as is all data and devices undergoing test.

Figure 4.15 Privacy screen covering testing stations

4.3.2 Cell Orientation

The orientation of a MTFC greatly affects the performance of the cell over time. An

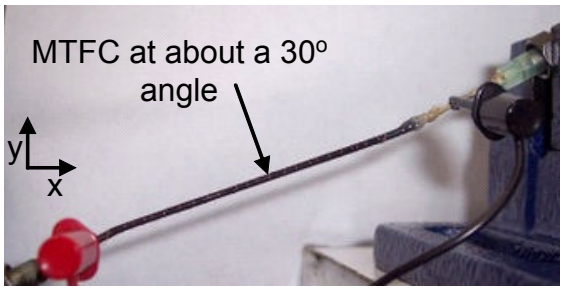

Figure 4.16 Cell orientation while testing

initial horizontal cell orientation yielded increasingly worse results the longer the cell was run. This was due to water build up inside the cell. A sloped cell orientation (approximately 30^{o}) allowed excess water to exit the cell and the performance no longer degraded over time. The effect of varying slopes was not investigated. Figure 4.14 shows the sloped cell orientation.

4.3.3 Hydrogen Flow Rate

Use of the FTC test station allows precise control of hydrogen flow rates to the cells. Hydrogen flow rates greater than 100 sccm produce results equivalent to flow rates of 100 sccm. Therefore, the standard flow rate for testing is set to 100 sccm.

4.3.4 Cell Conditioning

All MTFC cells are stored in deionized water to keep the MEA of the cell hydrated. After removal from the container, the cell is purged of water from the inside by using air to blow the hydrogen flow channel out. The air inserted is at room temperature and inserted using a small syringe with very low pressures. Thus, when the cell is initially hooked up any excess water and air left over must be removed from the anode before testing. This latter process is called cell conditioning. To properly condition the cell the hydrogen flow rate is set and the open circuit voltage is monitored. The open circuit voltage is monitored until it reaches a stable peak voltage at which point the open circuit voltage generally varies only by ±.0001 volts.

4.4 Types of Tests Utilized

This research utilizes two different types of testing to compare with the MTFC model developed as well as verify resistive losses inside the cells, i.e. a test to measure cell output to establish polarization curves and an EIS test to measure electrochemical impedance.

4.4.1 Polarization Curves

Fuel cells produce both voltage and current. As voltage changes so does current. A polarization curve is obtained by graphing cell voltage versus current.. Polarization curves give the overall performance of a cell. A general idea of the losses within the cell can be drawn from the shapes of the curves. The initial section is where activation losses are dominant. The activation losses of MTFC #8 can be seen by observing the first section of the polarization curve shown in Figure 4.17. The second section is a linear portion where ohmic losses are the dominant loss. The last section is usually an exponential loss due to concentration losses. In MTFCs the concentration losses appear to have little effect. This can be seen in Figure 4.17 which shows a polarization curve where only activation and ohmic losses can be seen. This is due to the fact that concentration losses are mainly from the cathode. MTFCs have larger cathode areas than anode areas and the entire cathode is exposed to air. These two factors eliminate much of the effect of the concentration losses.

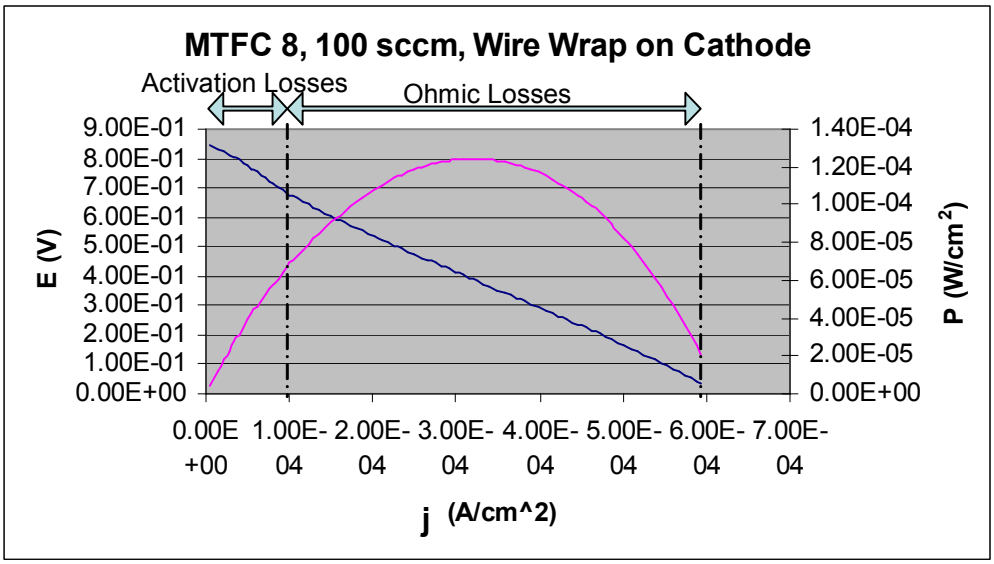

Figure 4.17 Polarization curve of MTFC 15

4.4.2 Electrochemical Impedance Spectroscopy (EIS)

EIS curves are taken by running the cell at a constant DC voltage and then sending a smaller AC current through the cell. The AC current phase is changed incrementally during the test. The change in the AC current magnitude yields the amount of resistance

in the cell, or the real impedance, while the change in phase of the AC current due to the cell yields the amount of imaginary impedance. The curves that are produced are called Nyquist diagrams and are a plot of the imaginary impedance (y-axis) versus the real impedance (x-axis). An example of a Nyquis diagram for a hypothetical flat plate PEMFC is given in Figure 4.19. Different parts of the Nyquist diagram show the magnitude of the losses in the cell as seen in Figure 4.19. The distance along the x-axis from zero to the first point on the curve gives an idea of the magnitude of the ohmic

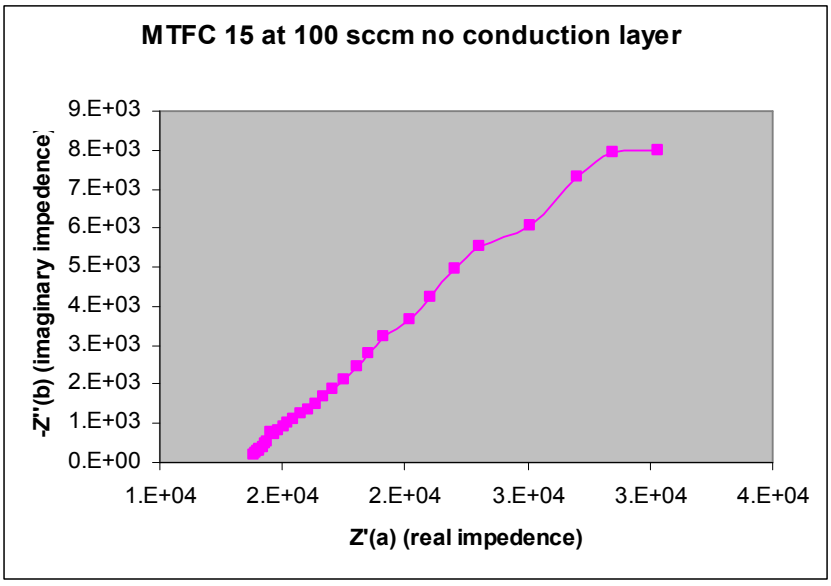

Figure 4.18 EIS curve of MTFC #15

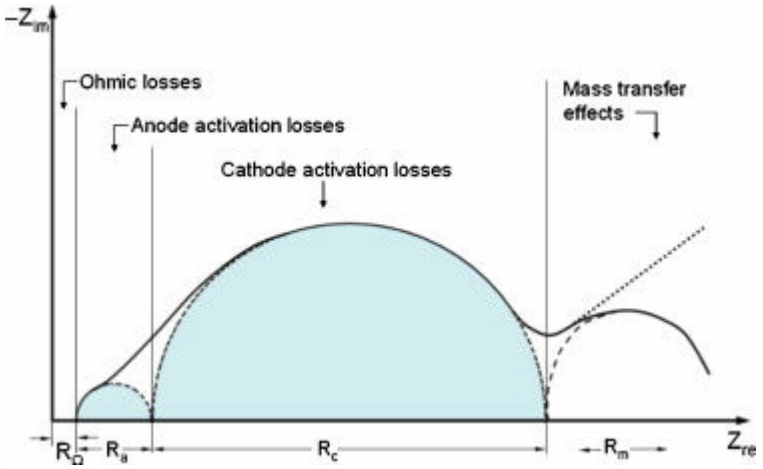

Figure 4.19 Nyquist plot of hypothetical flat-plate PEMFC by Zhu, Payne, and Tatarchuk (2007)

losses within the cell. As shown in Figure 4.19 the first small bump in the curve gives an idea of the anode resistances. This bump is often masked by cathode resistances (O'Hayre, 2006). The cathode resistances generally have the shape of a large hemisphere. Where the hemisphere meets the x-axis is where the resistances are calculated. Nyquist diagrams for MTFCs generally take the form seen in Figure 4.18, which is a plot for MTFC #15. The ohmic losses can be seen to be greater than 1.5 E4 ohms. The anode resistances seem to be mostly masked by the cathode resistances which are estimated by the extension of the impedance curve crossing the x-axis to be about 5E+4 ohms.

The following chapter develops a first principles model of a MTFC to predict losses, current density, voltage, and power density of MTFCs. This is done to enable design changes which will minimize major losses in the cell

Chapter 5

Micro-Tubular Fuel Cell Model

The last major portion of the project is a first principles based lumped parameter model for micro-tubular PEM fuel cells. All of the programming is done for the model was done using the iSCRIPT^{TM} program developed by TTC Technologies, Inc. The inherent complexity of fuel cells requires detailed numerical modeling to be able to approximate performance. This approximation is achieved by using two different sub-models in conjunction. The first of these is a lumped parameter (zero-D) loss sub model which uses an equivalent circuit approach to model the various resistances to flow and to activation of the electro –chemical reaction that occur in the MTFC. A number of the relations related to these resistances are developed and used in the 1-D model of Springer, Zawodzinski, and Gottesfeld (1991) are used in the lumped-parameter model developed and presented here. Details of this model are given in Section 5.2.

5.1 Lumped-Parameter Flow (LPF) Sub Model

The second sub-model is a lumped-parameter (zero-D) flow sub-model along the length of the interior channel (the z-direction) of the MTFC shown in Figure 5.1, accounting in the process for the diffusion of reactants (in this case H_2 and H_2O) into the

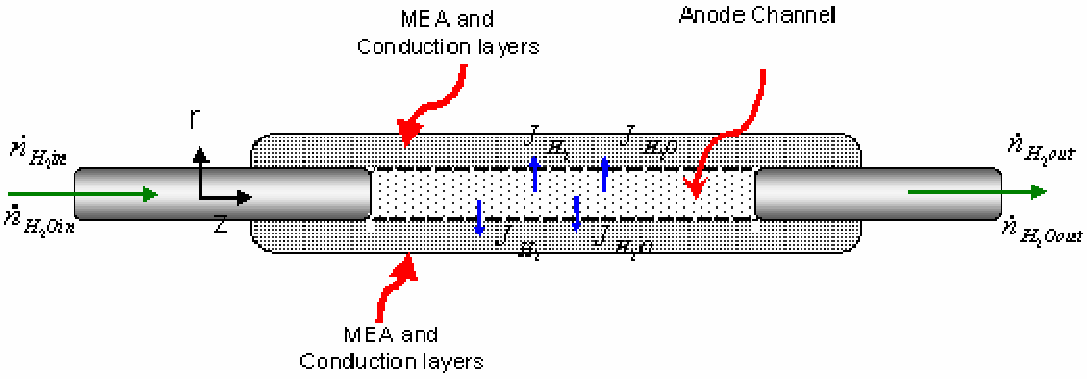

Figure 5.1 Lumped-Parameter Flow (LPF) Sub-Model

MEA in the r-direction as well. Thus in this model the effects of the depletion of reactants is taken into account as a function of the distance down the reactant channels. This sub-model is discussed in detail in the following section. The assumptions used in developing both sub-models are as follows:

- The cell operates at in steady state
- The cell is isothermal
- Liquid water effects are neglected
- All of the cathode is exposed to ambient air so there is no a significant depletion of oxygen along the length of the cell

The governing equations of the LPF sub-model are shown in Table 5.1 and consist of steady state molar flow rate balances of. water and hydrogen as well as the dominant electrochemical reaction mechanisms which. govern the use of the reactants and the production of products in the MTFC. Figure 5.1 shows the movement of hydrogen and

Table 5.1 Governing equations of the LPF sub-model

Variable Description		Model Equation
$\dot{n}_{H_2in}$	Molar flow rate of hydrogen entering cell	$\dot{n}_{H_2in} = \dot{n}_{H_2out} + J_{H_2}\pi D_i \Delta z$
$\dot{n}_{H_2out}$	Molar flow rate of hydrogen leaving cell	
J_{H_2}	Flux of hydrogen through membrane	
D_i	Inner diameter of cell	
Δz	Section length	
$\dot{n}_{H_2Oin}$	Molar flow of water entering cell section	$\dot{n}_{H_2Oin} = \dot{n}_{H_2Oout} + J_{H_2O}\pi ID\Delta z$
$\dot{n}_{H_2Oout}$	Molar flow of water leaving cell section	
J_{H_2O}	Flux of water produced	
Anode Reaction		$H_2 \rightarrow 2H^+ + 2e$
Cathode Reaction		$\frac{1}{2}O^2 + 2H^+ + 2e \rightarrow H_2O$

water into and out of the cell. The relations for determining the fluxes J_{H_2} and J_{H_2O} used in the mass balances given in Table 5.1 for hydrogen and for water are given in Table 5.2

and discussed in more depth below. The anode reaction given in Table 5.1 occurs in the anode catalyst layer of the MEA. This layer is immediately adjacent to the anode channel and anode conduction layer. This anode reaction draws hydrogen out of the anode channel into the MEA and is thus the driving force for the molar flux J_{H_2}. The cathode reaction occurs in the cathode catalyst layer which is on the opposite side of the MEA to the anode catalyst layer, is the driving force for the molar flux J_{H_2OBack} which contributes to the determination of J_{H_2O}.

The LPF sub-model takes into account the fact that the concentrations of products and reactants are not constant along the anode channel due to the electrochemical reactions occurring in the MEA. The sub-model divides the cell into several different sections of equal lengths. The molar flow rate balances given in Table 5.1 are then applied to each section in turn[1]. The hydrogen concentration is assumed constant

Table 5.2 Molar flow rate and flux relations used in the LPF sub-model

Variable Description		Model Equation
$\dot{n}_{H_2initial}$	Initial molar flow of hydrogen	$\dot{n}_{H_2initial} = \frac{P_{atm}\dot{V}_{H_2}}{RT_{std}}$
T_{std}	Standard temperature of 298.15 ^{o}K	
P	Pressure	
$\dot{V}_{H_2}$	Volumetric flow rate of hydrogen into cell	
J_{H_2}	Hydrogen flux through the membrane	$J_{H_2} = \frac{j}{2F}$
J_{H_2O}	Net molar flux of water into the MEA	$J_{H_2O} = J_{H_2O_{Drag}} - J_{H_2O_{Back}}$
$J_{H_2O\,Drag}$	Osmotic drag component of J_{H_2O}	$J_{H_2O\,Drag} = 2n_{drag}^{SAT}\frac{j}{2F}\frac{\lambda}{22}$
$J_{H_2O\,Back}$	Back diffusion component of J_{H_2O}	$J_{H_2O\,Back} = \frac{\rho_{dry}}{M_m}D_\lambda\frac{d\lambda}{dz}$

throughout each section. As long as the hydrogen concentration is greater than zero current is produced. This concentration or molar fraction of hydrogen in each section is

[1] Note that since the entire cathode is exposed to the ambient air, it is assumed that depletion of oxygen is not a function of cell length. Thus a molar flow rate balance for oxygen and water on the cathode side of the MTFC is not used.

determined by what happens in the anode and cathode catalyst layers and to the electrochemical activity there as well as by the net movement of water from anode to cathode across the MEA due to electro-osmotic drag and back diffusion. These effects are modeled by property relations which are part of the lumped parameter loss sub-model which is discussed next

5.2 Lumped-Parameter Loss (LPL) Sub Model

One of the major parts of modeling of any fuel cell is that of determining the various losses within the cell. These losses can be modeled as resistance and voltage losses. There are three major types of resistance losses. These include activation losses, ohmic losses, and concentration losses. Each of these types dominates the performance of cells in different ranges of the current, i.e. from low to medium to high. For example, at low currents the activation losses dominate performance whereas at mid-range currents, ohmic losses dominate. At high currents, concentration losses are the dominant loss in

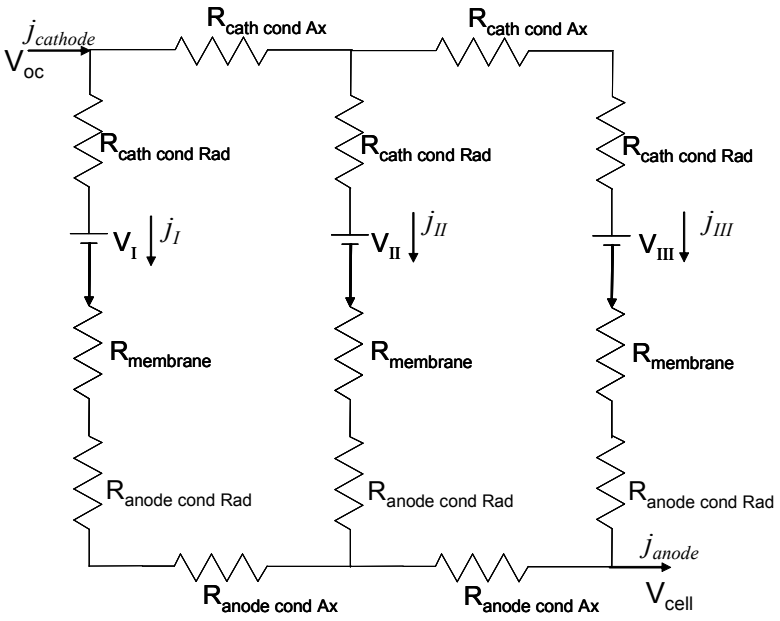

Figure 5.2 Possible equivalent electrical circuit diagram

cell performance. Figure 5.2 shows an equivalent circuit diagram for a MTFC split into 3 different columns. The resistive connections between each column are the connections in the axial direction of the cell. These can be seen in Figure 5.4. Each column represents

the losses going through the cell in the radial and circumferential directions, i.e.

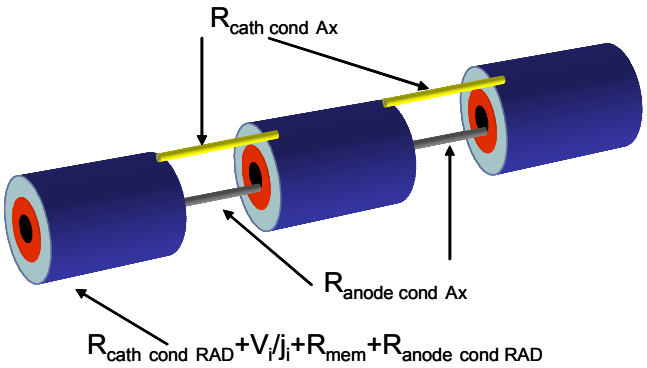

Figure 5.3 Physical interpretation of resistances

through and around a given cylinder or section (see Figure 5.3). Figure 5.4 shows the current pathways in the radial and circumferential directions in each cylinder or section. As the current passes through each layer, a resistance and/or voltage drop is associated with its passing.

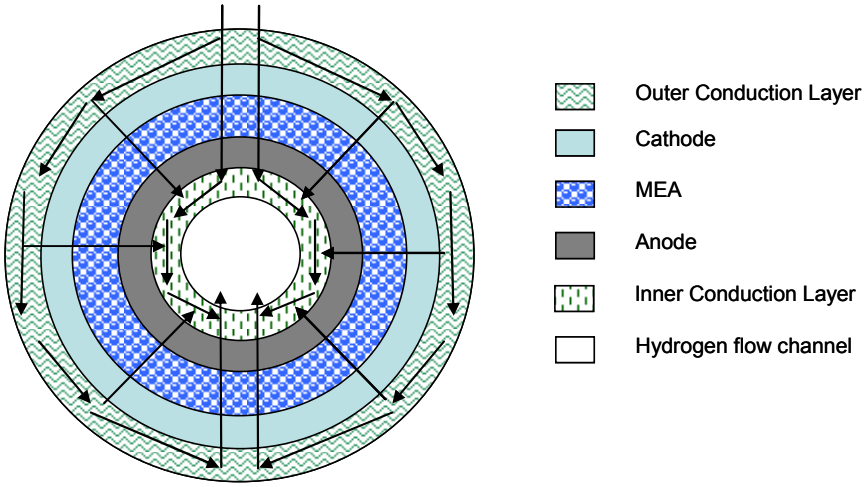

Figure 5.4 Current distribution within a micro-tubular fuel cell cross-section

5.2.1 Voltage Model

The governing equation for the equivalent circuit of the LPL sub-model is the voltage balance given in Table 5.2, as is the Nernst relation which establishes the relationship between the chemical potential of the hydrogen consumed in the MTFC and the cell's open circuit voltage.

R_{cell} which appears in the voltage balance equation comprises all the cell resistances and voltage losses as defined in Table 5.4. In this table, the voltage loss terms which appear in the columns of the equivalent circuit diagram of Figure 5.2, i.e. V_I, V_{II}, and V_{III},

Table 5.3 Governing and Nernst equations for the LPL sub-model

Variable Description		Model Equation
E_{thermo}	Open circuit voltage	$E_{thermo} = E_0 \quad \frac{RT}{nF} \ln\left(\frac{\prod a_{products}^{\upsilon_i}}{\prod a_{reac\,tan\,ts}^{\upsilon_i}}\right)$
a	Activity of constituent	
v_i	Stoichiometric coefficient	
R	Universal gas constant	
E_0	Standard state voltage	$E_0 = \frac{\Delta g_{rxn}}{nF}$
Δg_{rxn}	Change in chemical potential	
n	Number of electrons released per reaction	
V	Cell voltage	$V = E_{thermo} - R_{cell} j$
R_{cell}	Total cell resistance	
j	Cell current	

are the sum of the activation and concentration voltage losses or overpotenitals (i.e. η_{act} and η_{conc}) in each section of the MTFC. Expressions for these overpotentials are given in Table 5.5 along with expressions for the limiting current, j_L, and effective diffusivity, D_{ij}^{eff}, require to determine j_L.

As to the membrane resistance, $R_{membrane}$, it is a function of the membrane conductivity which is a function of temperature and membrane water content. This expression is shown in Table 5.6. To calculate R_{cell}, which is the total resistance of the equivalent circuit shown in Figure 5.2 the equivalent resistance in each part of the circuit

Table 5.4 Resistance and voltage loss relations used in the LPL sub- model.

Variable Description		Model Equation
$R_{membrane}$	Resistance of the membrane	$R_{membrane} = \int_0^{t_m} \frac{dr}{\sigma[\lambda(r)]}$
t_m	Thickness of the membrane	
R	General resistance of a material	$R = \frac{L}{\sigma A}$
L	Length of material	
A	Cross sectional area of the material	
σ	Conductivity of the material	

Variable Description		Model Equation
R_1	Resistance one	$R_1 = R_{cathcondAX}$
$R_{cathcondAX}$	Resistance of the cathode conductor in the axial direction	
R_2	Resistance two	$R_2 = \begin{pmatrix} R_{cathcondRAD} + R_{anodecondRAD} \\ + R_{membraneI} + R_{anodecondAX} \end{pmatrix} + \frac{V_I}{j_I}$
$R_{cathcondRAD}$	Resistance of the cathode conductor in the radial direction	
$R_{anodecondAX}$	Resistance of the anode conductor in the axial direction	
$R_{anodecondRAD}$	Resistance of the anode conductor in the radial direction	
V_i	Summation of voltage losses	
j_i	Cell current	
R_3	Resistance three	$R_3 = \begin{pmatrix} R_{cathcondAX} + R_{cathcondRAD} \\ + R_{anodecondRAD} + R_{membraneIII} \end{pmatrix} + \frac{V_{III}}{j_{III}}$
R_4	Resistance four	$R_4 = \begin{pmatrix} R_{cathcondRAD} + R_{anodecondRAD} \\ + R_{membraneII} \end{pmatrix} + \frac{V_{II}}{j_{II}}$
R_5	Resistance five	$R_5 = R_{anodecondAX}$
R_{cell}	Total cell resistance	$R_{cell} = \frac{\begin{pmatrix} R_1R_2R_3 + R_1R_2R_4 + R_1R_2R_5 + \\ R_1R_5R_4 + R_1R_5R_3 + R_2R_3R_5 + \\ R_2R_4R_3 + R_3R_4R_5 \end{pmatrix}}{\begin{pmatrix} R_1R_5 + R_1R_4 + R_1R_3 + \\ R_2R_3 + R_2R_4 + R_2R_5 + \\ R_5R_4 + R_5R_3 + R_4R_3 \end{pmatrix}}$

(i.e. R_1 to R_5) with the same current flow (i.e. $j\text{-}j_I$, j_I, j_{III}, j_{II}, j_I+j_{II}, respectively) is defined as indicated in Table 5.4 with each of the individual resistances as indicated in Figure 5.2 contributing to the determination of R_1 to R_2. Note that the cathode and anode conduction layer resistances are constant unless the cell being modeled does not have a separate conduction layer, at which point the resistance to the axial current is modeled as a

membrane resistance. Furthermore note that the resistances due to the catalyst layers are effectively modeled by the V_l/j_l terms which appear in Table 5.4

Table 5.5 Relation for the activation and concentration overpotentials

Variable Description		Model Equation
η_{act}	Activation losses	$\eta_{act} = \frac{RT}{\alpha nF}\ln(j_0) + \frac{RT}{\alpha nF}\ln(j)$
j_0	Exchange current density	
α	Slope of the Tafel plot	
F	Faraday's constant	
η_{conc}	Concentration losses	$\eta_{conc} = \frac{RT}{2F}\ln\left(\frac{j_L}{j_L - j}\right)$
j	Limiting current density	$j_L = \frac{4FD_{ij}^{eff}}{t_{electrode}}$
$t_{electrode}$	Thickness of the electrode	
D_{ij}	Nominal diffusivity	$D_{ij} = \frac{\left(a\left(\frac{T}{\sqrt{T_{ci}T_{cj}}}\right)^b (P_{ci}P_{cj})^{\frac{1}{3}}\right)}{(T_{ci}T_{cj})^{\frac{5}{12}}\left(\frac{1}{M_i}+\frac{1}{M_j}\right)^{\frac{1}{2}}}}{P}$
T_{ci}	Critical temperature of constituent i	
P_c	Critical pressure of constituent i	
M_i	Molecular mass of constituent i	
T	Cell temperature in Kelvin	
P	Pressure of location (anode or cathode)	
a	Constant dependent upon reaction	
b	Constant dependent upon reaction	

In order to determine the membrane resistance to current flow, $R_{membrane}$, the expression given in Table 5.4 is used. However, this expression depends both on the membrane water content as well as on its electrical conductivity. Expressions for both of these appear in Table 5.6. The simplified calculation for water content in the membrane, λ_{simp}, is dependent only upon the anode and cathode water vapor activities, which in turn are equal to the anode and cathode relative humidities. Table 5.7 provides the equations

Table 5.6 Relation for membrane water content and electrical conductivity.

Variable Description		Model Equation
λ_{simp}	Simplified membrane water content	$\lambda_{simp} = \begin{cases} \left.\begin{pmatrix} .0043 + 17.81 a_{H_2Oi} \\ 39.82(a_{H_2Oi})^2 + \\ 36.0(a_{H_2Oi})^3 \end{pmatrix}\right\} & for \; 0 < a_{H_2Oi} \le 1 \\ \left.\begin{pmatrix} 14 + 1.4(a_{H_2Oi} \quad 1) \end{pmatrix}\right\} & for \; 1 < a_{H_2Oi} \le 3 \end{cases}$
a_{H_2Oi}	Activity of water (cathode or anode)	
D_λ	Average water diffusivity in the membrane	$D_\lambda = \begin{pmatrix} \exp\left[2416\left(\frac{1}{303} - \frac{1}{T}\right)\right] \\ \begin{pmatrix} 2.563 \quad .33\lambda_{simp} + \\ .0264\lambda_{simp}{}^2 - .000671\lambda_{simp}{}^3 \end{pmatrix} 10^{\quad 6} \end{pmatrix}$
$\lambda(r)$	Membrane water content as a function of r	$\lambda(r) = \left(\frac{11\alpha}{n_{drag}^{SAT}} + C\exp\left[\frac{jM_m n_{drag}^{SAT}}{22F\rho_{dry}D_\lambda} r\right]\right)$
n_{drag}^{SAT}	Electro-osmotic drag coefficient	
M_m	Equivalent weight of Nafion™	
ρ_{dry}	Density of dry Nafion™	
α	Constant to be solved for	
C	Constant to be solved for	
σ_{303}	Membrane conductivity at 303 ^{o}K	$\sigma_{303}(\lambda(r)) = .005193\lambda - .00326$
σ	Membrane conductivity	$\sigma(T, \lambda(r)) = \sigma_{303}(\lambda)\exp\left[1268\left(\frac{1}{303} - \frac{1}{T}\right)\right]$

Table 5.7 Property relations used in the anode channel

Variable Description		Model Equation
φ	Relative humidity	$\phi = \frac{P_v}{P_{SAT}}$
P_v	Water partial pressure	
P_{SAT}	Saturated water pressure	
P_{H_2}	Hydrogen partial pressure	$P_{Anode} = P_{H_2} + P_v$
P_{Anode}	Total anode pressure	
y_{H_2O}	Water molar fraction	$y_{H_2O} = \frac{P_v}{P_{Anode}}$
y_{H_2}	Hydrogen molar fraction	$y_{H_2} = \frac{P_{H_2}}{P_{Anode}}$
a_{H_2O}	Activity of water (valid for anode)	$a_{H_2O} = \frac{P_{Anode}}{P_{sat}} y_{H_2O}$
y_p	Molar fraction	$y_p = \frac{n_{p,o}}{\sum_{p=1}^{5} n_{p,o}}$
$n_{p,o}$	Number of moles of constituent p	

used to calculate the relative humidity and activity in the anode channel while Table 5.8 provides those for the cathode side. As an approximation the water content of the membrane is the assumed to be an average of the anode and cathode simplified water contents. This average is used to find the average water diffusivity, D_λ, of the membrane, but only for $\lambda > 4$ (O'Hayre, 2006). Next the water content as a function of r (through the membrane), is calculated using the membrane water content equation from Table 5.2. The electro-osmotic drag coefficient shown in Table 5.6 is the number of water molecules dragged per proton across the membrane. Both α and C are constants that can be solved for by using the simplified membrane water content equation to calculate the water content at the anode and cathode. These values are then used found are used as boundary conditions r = 0 (membrane/anode boundary) and r = tm (membrane/cathode boundary) to determine the constants α and C. Knowing the value of λ at any r location one can solve for the membrane conductivity at any r location. This is done using the membrane conductivity expression as a function of temperature and water content. The membrane conductivity and water content equations are valid for all sections of the MEA layer.

Table 5.8 Property relations used on the cathode side.

Variable Description		Model Equation
φ	Relative humidity	$\phi = \frac{P_v}{P_{SAT}}$
P_v	Water partial pressure	
P_{SAT}	Saturated water pressure	
P_{Air}	Air partial pressure	$P_{Atm} = P_{Air} + P_v$
P_{Atm}	Total anode pressure	
y_{H_2O}	Water molar fraction	$y_{H_2O} = \frac{P_v}{P_{Cathode}}$
y_{O_2}	Oxygen molar fraction	$y_{O_2} = \frac{P_{Air}(.21)}{P_{Cathode}}$
a_{H_2O}	Activity of water (valid for anode)	$a_{H_2O} = \frac{P_{Atm}}{P_{sat}} y_{H_2O}$
y_p	Molar fraction	$y_p = \frac{n_{p,o}}{\sum_{p=1}^{5} n_{p,o}}$
$n_{p,o}$	Number of moles of constituent p	

Now, before completing this chapter, a few words are in order about the voltage losses (overpotentials) which occur due to elector-chemical activation, Ohmic resistance, and mass diffusion (concentration) limitation. These are discussed in the following sections.

5.2.2 Activation Voltage Losses (Overpotential)

The Tafel equation is used to find the activation voltage losses (overpotentials) in the cell. It is an approximation of the more general electrochemical kinetic rate equation called the Butler-Volmer equation The former is expressed as $\eta_{act} = a + b\ln(j)$, which is equivalent to the version given in Table 5.5 where *a* is the y-intercept of the Tafel plot which is dependent upon temperature, the number of electrons, *n*, released in the reaction, and on two kinetic parameters, namely, the so-called charge transfer coefficient α and the exchange current density $j_{0.}$ The slope of the Tafel plot *b* depends only on temperature, α, and *n*. The exchange current density, $j_{0,}$ is found by using the data from an experimentally determined polarization curve. A Tafel plot is created by plotting the overpotential from the polarization curve versus the natural log of the cell current density. The current that causes the overpotential to be zero is then found by extrapolation. This is the so-called exchange current density, j_0, for both the anode and cathode. However, due to the fact that the cathode activation resistances losses are much greater than those for the anode, this joint (i.e. anode and cathode) experimentally determined current density primarily reflect the exchange current density of the cathode alone. Nonetheless, it is a good approximation and useful since the exchange from the experimentally determined polarization curves presented in the next chapter as well as in the literature.

5.2.3 Ohmic Voltage Losses (Overpotential)

Ohmic voltage losses (overpotentials) are the losses due to resistances in the materials of the cell to current flow. These include both electronic resistances and resistance to the movement of protons across the membrane of the cell. The general equation for calculating the resistance of a material is given in Table 5.4. For most materials this is a straight forward calculation. For the membrane however, it is not

because the resistance of the membrane is not constant. It is a function of current, while current in turn is a function of resistance. One method to solve this would be to use a simple circuit such as the circuit shown in Figure 5.2 and find the ratio of currents which is flowing through each section. This ratio would then be used to find the membrane resistance for each column shown in Figure 5.2.

5.2.4 Concentration Voltage Losses (Overpotential)

The concentration losses of the cell are due to mass diffusion limitations wich occur in the cathode and anode catalyst layers. These occur when the rates of reaction of te heterogeneous (i.e. surface) reactions occurring at the so-called 3-phase boundaries (i.e. joint carbon, platinum, and polymer sites) in these layers have reached a maximum and any further addition of reactants in the bulk flow within these layers causes a significant drop off in performance since these additional reactants can no longer be processed rapidly enough. Thus, more is not always better.

5.2 iSCRIPT™

iSCRIPT™ is the name of the scripting language used to develop the MTFC model. It was developed by TTC Technologies specifically to create engineering models and perform optimizations of the same. This scripting language was chosen because it is expected that eventually the MTFC model will be used as a sub-model in a MTFC system model which will include parameters of fuel storage and delivery etc., thus the need to use a scripting language that would be able to perform optimizations later on a full system.

Finally, the results generated by the MTFC model are presented in Chapter 6 which also gives the results for the feasibility study and for the experimental tests which were explained earlier.

Chapter 6

Results and Discussion

The results of each of the three major research focuses are presented and discussed here. These results include the final results obtained from the feasibility study, the experimental results of cell testing, and the iSCRIPT™ computer model.

6.1 Feasibility Study Results

A summary of the most pertinent results in the feasibility study which lead to the three fuel cell configurations which warrant further study and possible development are given below by fuel type and storage, with and without a fuel cell stack. Comparisons are made with current battery technology.

6.1.1 Hydrogen with and without a Fuel Cell Stack Inside

In an initial screening, based solely on the storage medium capacity to provide an

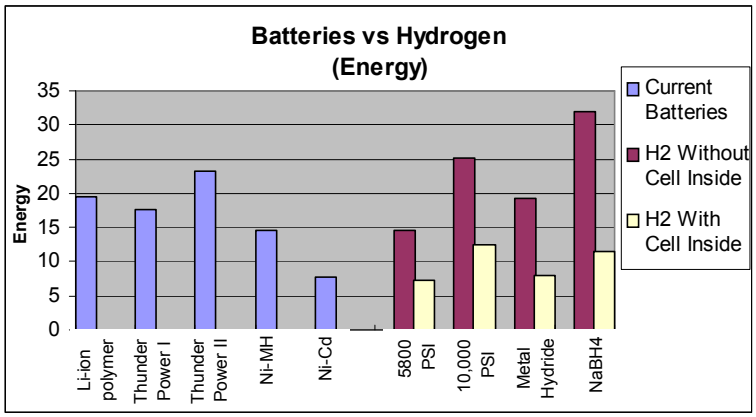

Figure 6.1. Batteries versus hydrogen with and without fuel cell.

upper limit on range for the micro air vehicle (MAV) discussed in Chapter 1, the only hydrogen fuel storage systems able to potentially exceed the 24 W-hrs provided by the best current battery technology (i.e. the lithium-ion Thunder Power II) are the 10,000 psi

and the sodium borohydride hydrogen storage systems as shown in Figure 6.1. This assumes that the storage system occupies the entire volume set aside for the fuel cell stack in the MAV (i.e. 4 in (101.6 mm) x 1.25 in (31.75 mm) x 0.625 in (15.875 mm)) and that there is sufficient interstitial space is available in the fuselage where micro-tubular fuel cells could be used. If in fact the set-aside volume must also be occupied by a fuel cell stack, none of the hydrogen systems can produce over 24 W-hrs, and are, thus, not able to compete with current battery technology.

6.1.2 Direct Methanol (MeOH) Fuel Cells with and without a Neat Storage

By using neat (i.e. pure) storage of MeOH passively delivered using wicking technology, the direct methanol (MeOH) systems with both the fuel storage and fuel cell stack in the set aside volume provide excellent results, i.e. exceed the performance of existing battery technologies as see in (see Figure 6.2). Of these systems, the ones with 2.5 molar (10.12% by volume) and 3.25 molar (13.15% by volume) water-MeOH

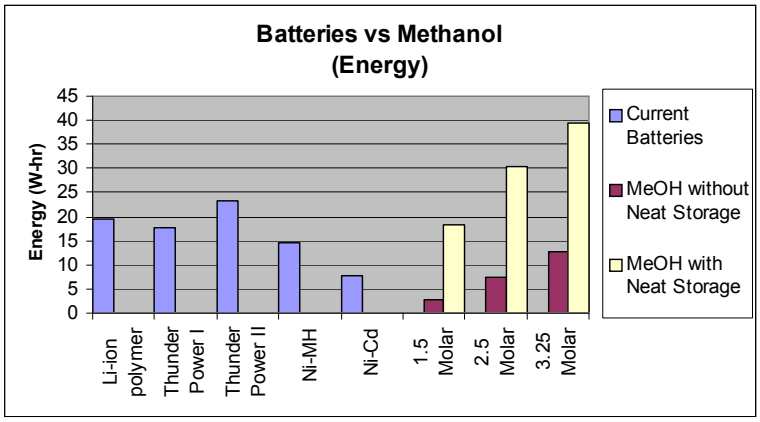

Figure 6.2 Energy production comparison between battery technologies and DMFC systems with and without neat storage.

solutions on the anode side of the fuel cell (where 3.25 molar is the maximum allowable concentration due to fuel cross-over) exhibit the most promising results with some of the highest energy (W-hr), mass energy densities (W-hr/kg), and volume energy densities (W-hr/cm^3) (see Figure 6.2 as well as Figures 6.3 to 6.5 below) of all the systems studied.

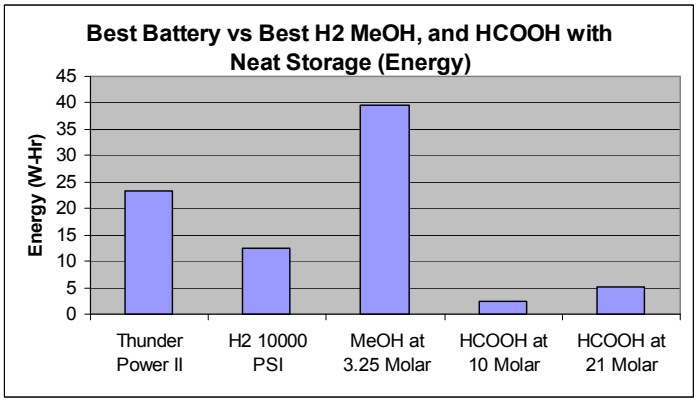

Figure 6.3 Energy delivery of the best battery technology versus the best fuel storage options plus fuel cell included in the set aside volume.

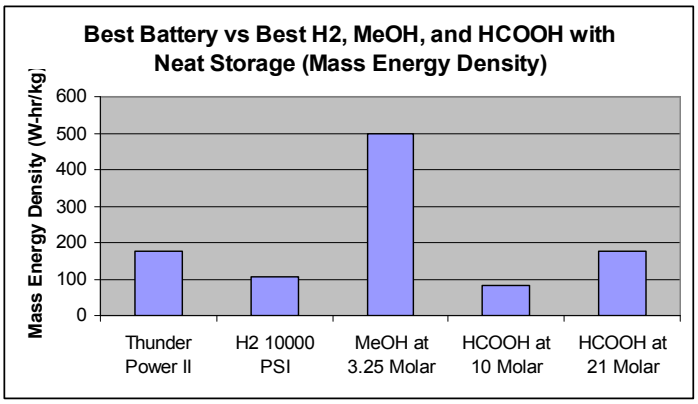

Figure 6.4 Mass energy density of the best battery technology versus the best fuel storage options plus fuel cell included in the set aside volume.

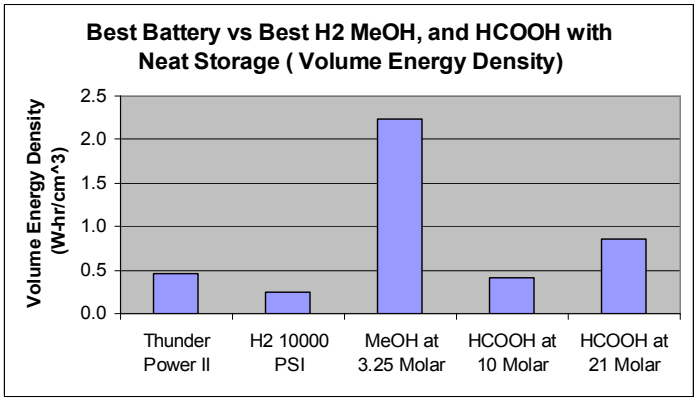

Figure 6.5 Volume energy density of the best battery technology versus the best fuel storage options plus fuel cell included in the set aside volume.

The alternative direct MeOH fuel cell case of storing a premixed solution of MeOH and water (i.e. no neat storage of MeOH) assumes that the entire set-aside volume for the stack is, in fact, occupied by the storage of the water-MeOH solution and that there is sufficient space in the remained of the fuselage for the fuel cell stack. This alternative as can be seen in Figure 6.2 does not fair well. Furthermore note that the direct formic acid systems which also appear in Figures 6.3 to 6.5 are discussed in the next section.

6.1.3 Direct Formic acid (HCOOH) Fuel Cells with and without Neat Storage

The direct formic acid (HCOOH) systems that display the largest energy (W-hr) and mass energy density (W-hr/kg) are the systems without neat fuel storage and that do not include the fuel cell stack with in the set aside volume. This is seen in Figure 6.6 and 6.7 as well as Figures 6.3 and 6.4 above. As seen in these figures, molar concentrations of HCOOH in water of 1.0, 10.0 and 21.0 (3.86%, 38.6%, and 80.55% by volume) are considered with the latter the maximum allowable concentration due to fuel crossover.

Unlike with MeOH, HCOOH does not benefit from the neat storage of fuel as much as does MeOH for several reasons. With HCOOH, higher molar concentrations at the fuel cell anode can be used without the problem of significant crossover (as MeOH is prone to do at such high concentrations, i.e. at 10.0 and 21.0 molar). Also, HCOOH has a lower

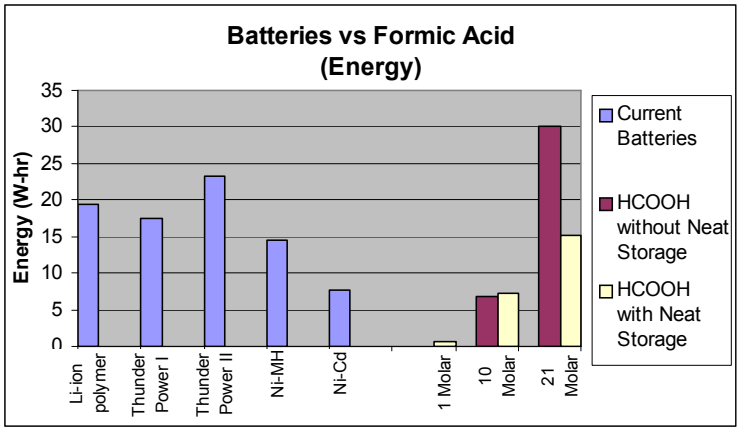

Figure 6.6 Energy production comparison between battery technologies and DFAFC systems with and without neat storage.

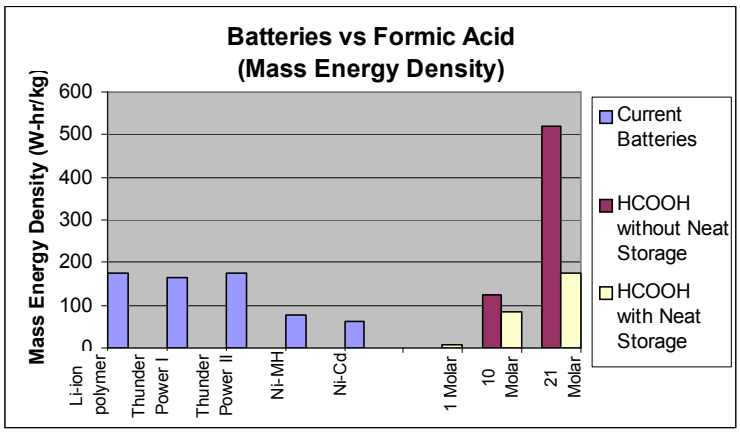

Figure 6.7 Batteries versus HCOOH with and without fuel cell

energy density than MeOH. So for a small increase in the number of moles of formic acid, there is a relatively small increase in total energy. Thus the DFAFC system with neat fuel storage is in this case the better DFAFC system with respect to energy production and mass energy density (see Figures 6.6 and 6.7). However, it is not when considering the volume energy density as seen in Figure 6.8. Additionally, due to HCOOH's lower energy density when compared to MeOH, neither DFAFC system (i.e. with and without neat storage) does as well as the DMFC system with neat storage.

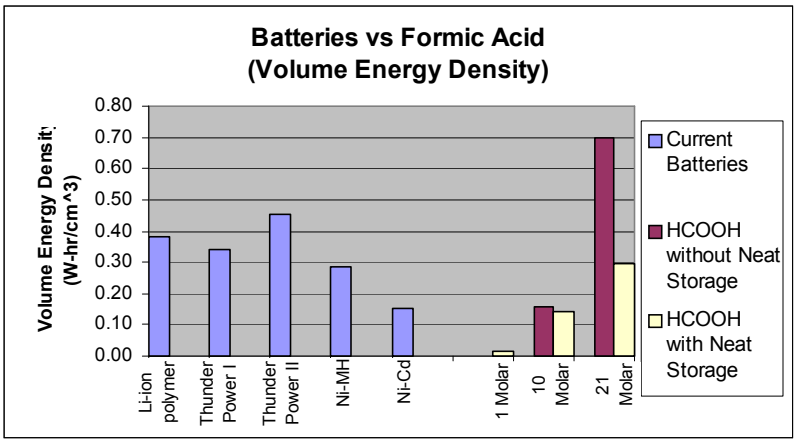

Figure 6.8 Batteries versus HCOOH with and without fuel cell

6.1.4 More Comparisons between the Best Battery Technologies and the Best Fuel Storage Options

When comparing the best battery technology (Thunder Power II) with the best of hydrogen storage option (hydrogen pressurized at 10,000 psi) and fuel cell included in the set-aside volume, the best MeOH storage option and fuel cell included in the set-aside volume (MeOH with wicking technology and 3.25 molar solution at the fuel cell anode), and the best HCOOH storage option in the set-aside volume with the fuel cell outside this volume (HCOOH without wicking technology and both 10 molar and 21 molar solutions at fuel cell anode), it can clearly be seen in Figures 6.3 to 6.5 which technologies offer the most promising solutions. Both the 10 molar and 21 molar HCOOH concentrations are used because the literature is unclear what the actual upper limit on HCOOH concentration is before cross-over becomes too important. Figure 6.3 shows that the best MeOH solution out performs all other technologies by at least 13 W-hr. That is 150% of the best battery technology. The MeOH solution is also the clear winner in terms of mass energy density with 750 W-hr/kg (see Figure 6.4). HCOOH at 21 molar is the closest with 253 W-hr/kg, while Thunder Power II comes in a distant third at 175 W-hr/kg. Figure 6.5 shows that the MeOH solution also has the best performance in terms of volume energy density with 2.2 W-hr/cm^3. At a concentration of 21 molar, HCOOH is the second best performing with 0.86 W-hr/cm^3 while the best battery comes in at only 0.45 W-hr/cm^3. Thus the MeOH solution outperforms the Thunder Power II in terms of energy density by 329% and 388%, respectively.

Finally, Figure 6.8 compares the total energy of the best battery technology against the best hydrogen storage options (i.e. hydrogen both at 10,000 psi and in a sodium borohydride tank) without a fuel cell included in the set-aside volume, the best MeOH storage option without a fuel cell included in the volume, and the best HCOOH (both 10 molar and 21 molar) storage options without a fuel cell include in the volume. The large difference between the 10 and 21 molar is due mostly to the change in efficiency attributed to the fuel cell. For the 10 molar solution, the efficiency is found to be 22% while at 21 molar the efficiency is determined to be 46%. These efficiencies as well as those for the other fuel cells are calculated on the basis of the performance curves found Yeom et al. (2005) and are presented and discussed in Chapter 3. Of course, when the MeOH storage option is changed from a 3.25 molar MeOh-water solution to neat storage

of MeOH, then even with the storage tank now sharing the set-aside volume with the fuel cell, the DMFC beats all the competition as seen in Figure 6.10.

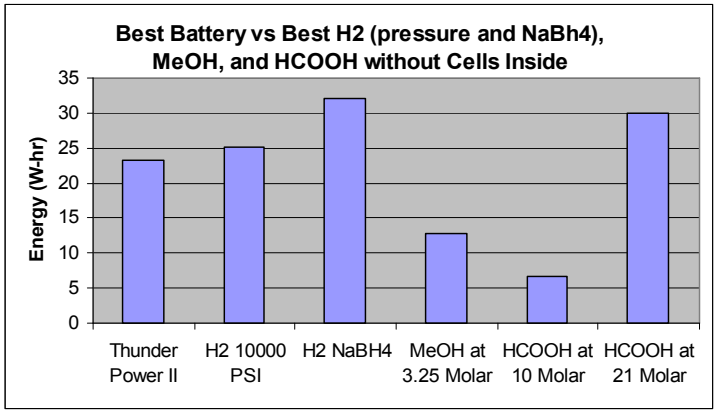

Figure 6.9 Energy production comparison of the best battery technology versus the best fuel storage options without a fuel cell included in the set-aside volume.

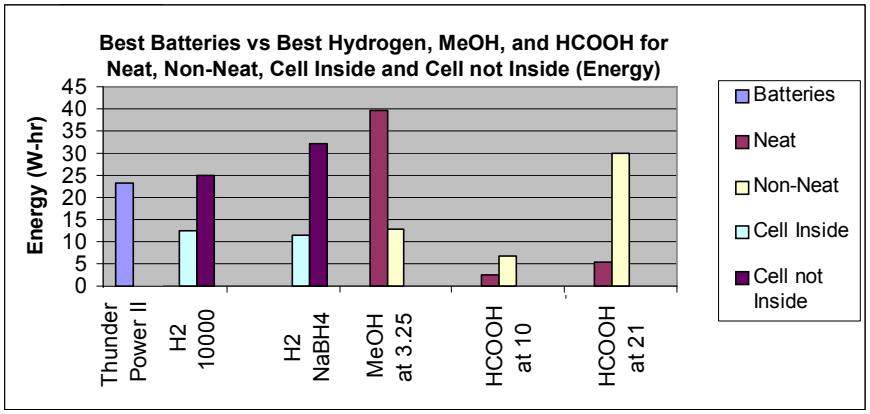

Figure 6.10 Energy production comparison of the best battery technology versus the best fuel storage options.

Another method to quickly compare energy storage devices is a Ragone plot. The y-axis on the Ragone plot is a measurement of the system's mass power density (W/kg) while the x-axis is the system's mass energy density, i.e. the x-axis shows the amount of energy available in the system and the y-axis shows how quickly the energy is able to be delivered by the system. The axes are plotted on logarithmic scales. This allows a comparison of very low power systems with high power systems. Figure 6.11 shows a gravimetric Ragone plot of the Thunder Power II and MeOH (3.25 molarity) with neat

fuel tank systems. It can be seen that over the range shown that the fuel cell system has a fairly constant rate of energy production over the range of 5 to 40 W-hr/kg. At higher ranges, the fuel cell system is seen to drop in energy production rates because of the tradeoffs in stack size and fuel storage size. The battery as expected has a very limited range for energy density. The energy density of the battery is not a constant because at higher energy draw rates (i.e. higher powers) batteries experience a drop in energy density due to resistive losses present in the cell at high discharge rates. Figure 6.11 also shows that the DMFC system could be used to power a 10 W system for over 10 hours or a 60 W system for only 4 or 5 minutes.

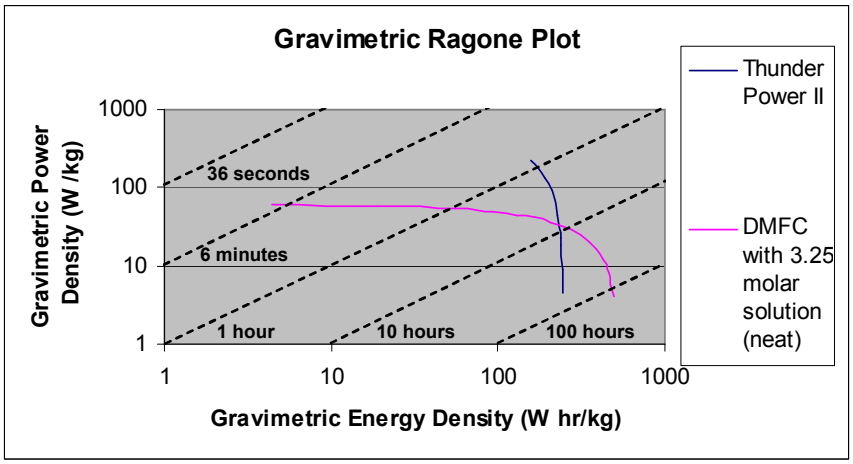

Figure 6.11 Gravimetric Ragone plot showing the DMFC neat system (3.25 molarity) and the best performing battery.

The complete information on the battery evaluations is shown on Table A1 of Appendix A. The complete information on the hydrogen capabilities is presented on Table A2 of Appendix A, on the MeOH capabilities in Table A3a and A3b of Appendix A, and on the HCOOH capabilities in Table A4a and A4b of Appendix A.

The calculations for the hydrogen configurations with the cells inside the set-aside volume, and the neat storage configurations for MeOH and HCOOH were based upon the design and performance estimation of Mench et al. (2001) for a DMFC as discussed in Chapter 3. By comparing the performance estimation of Mench et al. (2001) (about 50 mW/cm^2 at 0.5 v and 0.1 A/cm^2 for a DMFC) and the experimental results of Yeom et al. (2005) (for a PEMFC and a DMFC) it is found that the performance estimation for the

DMFC initially seems high. The hydrogen cell performance presented by Yeom et al. (2005) is about 15 mW/cm^2 (at 0.55 v and 65 mA/cm^2, using atmospheric pressure and room temperature) less than the performance estimation by Mench et al. (2001) for a DMFC. Generally hydrogen fuel cells exhibit a difference of at least an order of magnitude higher performance than a DMFC and half an order of magnitude for a DFAFC under the same conditions. This can be seen in the testing of Yeom et al. (2005) where the hydrogen performance mentioned above is compared with the performance of a DMFC and a DFAFC, using atmospheric pressure, room temperature, a 1.25 molar solution, and a 10 molar solution, respectively. A difference of 2 orders of magnitude is seen between the DMFC (0.35 mW/cm^2, at 0.45 v and 3.75 mA/cm^2) and the PEMFC results. While a difference of about 0.5 is seen between the DFAFC (0.16mW/cm^2, at 0.6 v and 60 mA/cm^2) and the PEMFC results. Mench et al. (2001) present data from a 50 cm^2 DMFC with operating conditions of 1 molar solution, 80 ^{o}C, and pressures of 1 atm on the anode and 2.1 atm on the cathode and find a peak power generation of about 110 mW/cm^2. The differences between the results of Mench et al. (2001) and Yeom et al. (2005) for DMFCs and DFAFCs could be due to the differences in the testing conditions that are used. Another reason for the disparity between the performance of Yeom et al.(2005) and Mench et al. (2001) could be the catalyst layer type. The type used by Yeom et al. (2005) is a platinum catalyst while Mench et al. (2001) most likely used a platinum and ruthenium catalyst (Pt-Ru). The authors do not explicitly state the catalyst type used for testing, but the Pt-Ru catalyst is the type most commonly used in DMFC configurations (Larminie, and Dicks, 2003). The Nafion™ type used by Yeom et al. (2005) is Nafion 112 while Mench et al. most likely use the thicker Nafion™ 117. Again, the authors do not state the type used, but Nafion™ 117 is the type most commonly used in DMFC configurations (Larminie, and Dicks, 2003). The performance estimate of 50 mW/cm^2 at 0.5 v and 0.1 A/cm^2 assumed in the calculations for the PEMFC cells seems plausible because all of the cell operating pressures, which vary by storage type, are above atmospheric. Also the performance claimed by Mench et al. (2001) for DMFCs and DFAFCs (50 mW/cm^2 at 0.5 v and 0.1 A/cm^2) seems plausible, depending on the temperature, pressure, catalyst type, and Nafion™ type in use.

6.1.5 Volume Comparisons between the Best of the Micro-Tubular and Flat Plate Configurations

Only the most promising results of the comparison between the micro-tubular and flat plate configurations are presented (see Figure 6.12 and Figure 6.13) and discussed

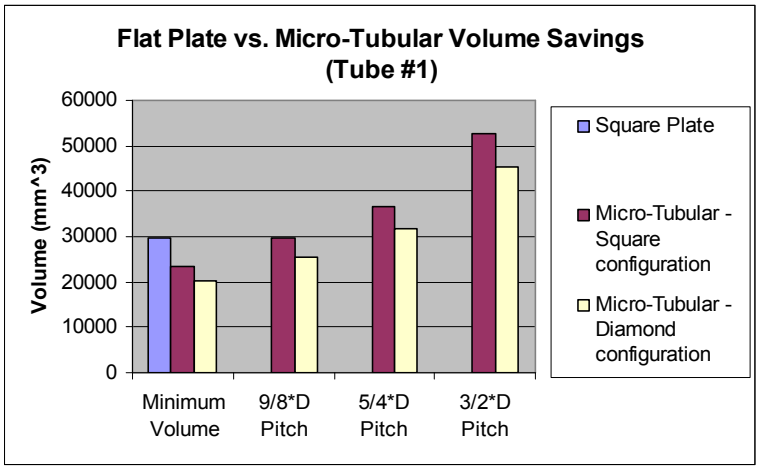

Figure 6.12 Volume efficiencies of flat plate cell versus tubular cell in several configurations.

here. The data used to generate these figures and additional data is given in Appendix B which show the results presented in tables for the less promising configurations. The results of the less promising considerations are not included here because all of them have worse volumes and weights than the flat-plate configuration. This can be seen in Figure 6.14, which shows the volumetric results for tube 5 which are much poorer than those of tube 1. Results for a volumetric comparison between the best micro-tubular and flat plate configurations are seen in Figure 6.12 and show that by using a diamond tubular pattern with a (9/8)D pitch and the micro-tube (tube #1) with the smallest outside diameter (D=0.838 mm; see Tables 3.6 and 3.7 as well as Figures 3.8 and 3.9 of Chapter 3) that the volume of the micro-tubular fuel cell stack sized to meet the power and energy requirements of the given MAV (2 A and 12 v at steady state with a maximum transient current draw of about 5-6 A and an energy output exceeding that of the best battery technology) is only 25,602 mm^3 compared to the 29,766 mm^3 required by the flat plate design (the flat plate design used for calculations is that of Mench et al. (2001) which is discussed in Chapter 3). Note that these values represent 50% and 58% of the total set-

aside volume (51, 210 mm^3) intended for the fuel cell system (i.e. fuel cell stack plus fuel storage). The effect of replacing a micro-tubular stack for the flat-plate stack would

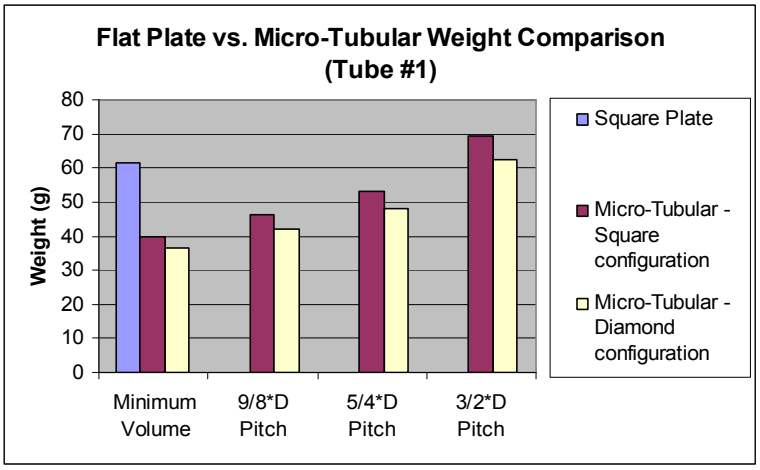

Figure 6.13 Weight efficiencies of flat plate cell versus tubular cell in several configurations.

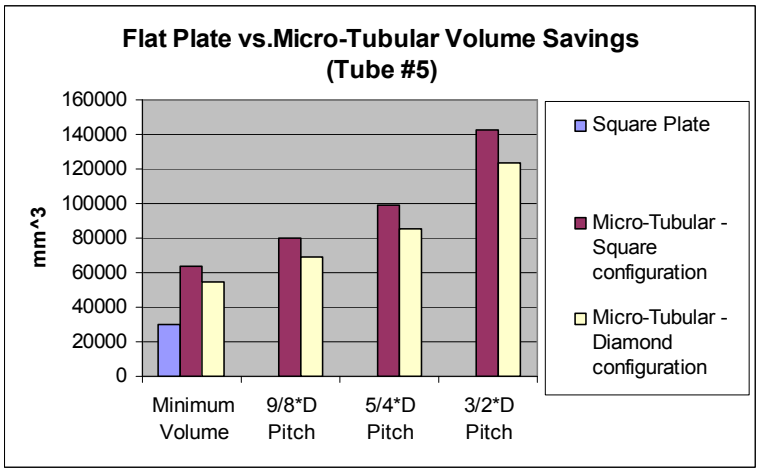

Figure 6.14 Weight efficiencies of flat plate cell versus tubular cell (with Tube 5 as size) in several configurations.

provide even better energy production, mass energy density, and volume energy density, this would cause the results seen in Figure 6.5 to have an even greater disparity between the battery and fuel cell performance.

Results for a weight comparison between the best micro-tubular and flat plate configurations that are sized to meet the same power and energy requirements are seen in Figure 6.13. Using the same configurations as in Figure 6.12, shows that the flat plate

configuration has a mass of 61.3 g while the best micro-tubular cell using the diamond pattern a (9/8)D pitch and tube #1 has a mass of only 43.2 g. For comparison, the mass of the Thunder Power II battery is 133 g, which is over 3 times the mass of the micro-tubular cell configuration using the diamond pattern the (9/8)D pitch, and tube #1. Also the minimum volume in both figures refers to a micro-tubular fuel cell with no spacing between the tubes. This is done in order to establish a lower limit on the micro-tubular volume and weight performance.

6.2 Experimental Results

The experimental results for this section were obtained using the methods described in Section 4.3 of Chapter 4. These results are used to gauge the improvements realized in the MTFC design and will be compared with the results from the iScript computer model. All of the MTFC MEAs tested were prepared by Luna Innovations, Inc., and all of the micro-tubular cells were also constructed by Luna Innovation, Inc. with the exception of MTFCs #VT and #2 VT, as discussed above. Over 78 polarization tests and over 24 different EIS tests were conducted using 13 different fuel cells. Only the best results are presented here. Additional figures of results can be found in Appendix C. Table 6.1 shows the best results for each fuel cell that yielded results. Three of the cells tested yielded open circuit voltages that were too low to be able to measure a polarization curve. The polarizations produced by MTFCs as can be seen in the results have a

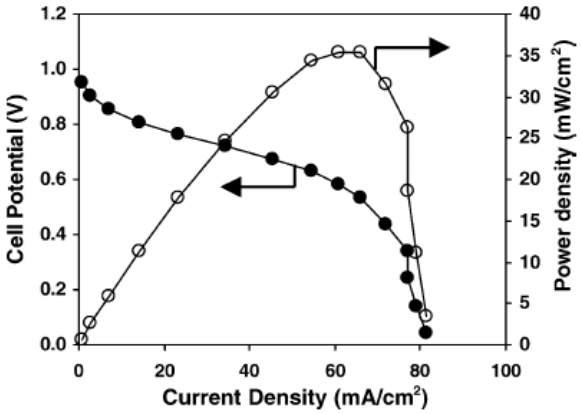

Figure 6.15 Polarization and power curves using hydrogen as fuel (Yeom et al., 2005).

slightly different shape than polarization curves of flat-plate cells. Flat-plate polarization curves usually end with distinct drop-off due to concentration losses as seen in Figure

Table 6.1 Summary of fuel cell properties and test results

Cell	Active Area (cm^2)	Anode Conduction Layer	Cathode Conduction Layer	Max Eoc (V)	Max P (W/cm^2)	Max j at .3 V (A/cm^2)	Min Real Impedance (Ω)
MTFC #4	2.59	Silver	Silver	.574	3.93 E-7	5.54E-7	None
MTFC #5	.930	None	None	.594	9.73 E-6	3.24E-5	None
MTFC #6	1.536	None	None	Not Useable			None
MTFC #7	1.162	None	None Wire Mesh	.786 .818 .553	3.81 E-6 3.18 E-5 6.04E-6	1.02E-4 1.03E-4 3.24E-5	8.23 E4 3.17E3 None
MTFC #8	.835	None	None Wire	.861 .844	2.69 E-5 1.32 E-4	8.29E-5 4.12E-4	4.36 E3 None
MTFC #9	1.939	None	None Wire	.867 .869	1.13 E-5 8.38 E-5	3.45E-5 4.12E-4	3.68 E4 None
MTFC #10	1.372	None	None Wire	.800 .799	4.75 E-5 2.07 E-4	1.50E-4 5.69E-4	Not usable None
MTFC #12	1.068	Silver	Silver Silver / wire	.652 .622	1.33E-4 1.25E-4	4.40E-4 3.84E-4	582 None
MTFC #13	1.2246	None	None Wire	.814 .796	7.88E-6 1.36E-4	2.44E-5 4.35E-4	None None
MTFC #15	1.788	None	None Wire	.738 .766	3.57 E-6 1.32 E-5	1.19E-5 4.21E-5	1.39 E4 None
MTFC #17	1.79	None	None Wire	.534 .532	2.78E-8 2.64E-8	9.12E-8 8.69E-8	None None
MTFC #VT	.806 Repair .776	Wire	None Wire	.737 .746	1.10 E-4 8.07 E-4	3.56E-4 2.62E-3	3.93 E4 None
MTFC #2 VT	.806	Wire (helical)	None Wire	.79 .717	7.10 E-5 3.92 E-4	2.30E-4 1.30E-3	250 51

6.15. Thus it would appear that concentration overpotentials play little or no role in the MTFCs tested here.

In addition to a lack of concentration overpotential, several of the polarization curves were unsmooth (i.e. erratic). The data from unsmooth curves is not included in Table 6.1. As can be seen in the table from early results (MTFCs #4, #5, and #6) and later

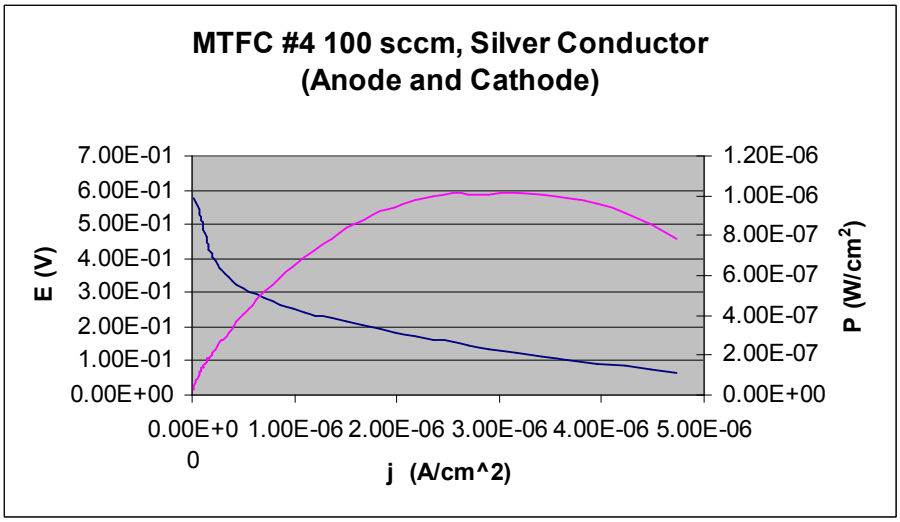

Figure 6.16 Polarization curve of MTFC 4 at 100 sccm with a silver anode and cathode conduction layer

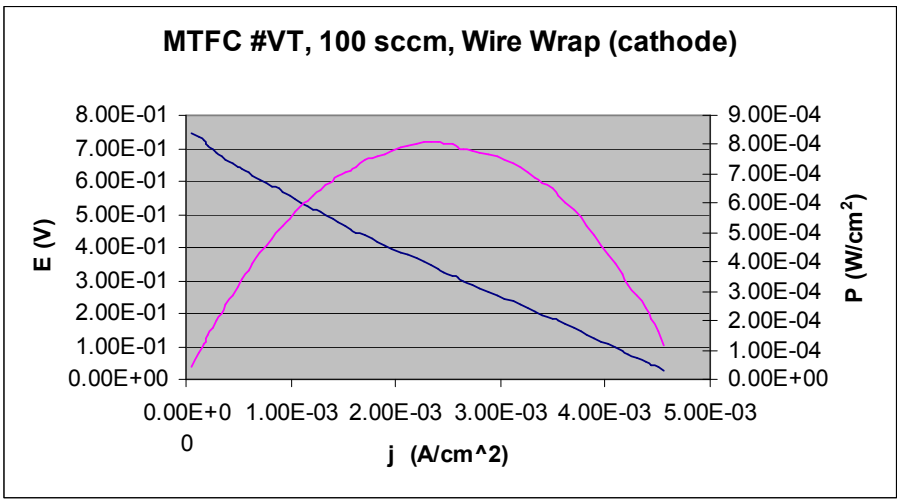

Figure 6.17 Polarization curve of MTFC VT at 100 sccm with a wire wrap as a cathode conduction layer, and a single straight wire as an anode conduction layer

results (MTFCs #VT and #2 VT) an increase in maximum power production of over 3 orders of magnitude has been realized. This can easily be seen by comparing the results shown in Figures 6.16 and 6.17. This increase is due to many different factors. Improvements in cell construction, catalyst layer application and uniformity, and conduction layer performance all aided in increasing cell performance. The poor results from MTFC #4 have been attributed in part to the silver layer. As discussed in Section 4.2.3 of Chapter 4 the silver layer constructed by Luna Innovations, Inc. is formed using

nano-sized particles. The silver layer is supposed to be nano-porous. It was speculated initially that the silver layer was not allowing sufficient diffusion of products and reactants for the cell to function properly. From the data in Table 6.1 on MTFC #12 it can be seen that the performance of the nano-porous silver layer has improved tremendously due to changes in the preparation of the silver before the cell is coated.

The best performance to date of any of the MTFCs is that of MTFC #VT. As can be seen from Table 6.1, the higher power density of this cell is due in part to an enhanced conduction layer constructed at Virginia Tech. The anode conduction layer of MTFC #VT consists of a small 0.003 in. diameter copper wire that was placed in the anode at the time of cell construction. It runs the length of the cell. In addition, the cathode conduction layer, also constructed at Virginia Tech, is a helically wrapped copper wire. As see in Figure 6.17, these conduction layers allow MTFC #VT to have lower ohmic losses than previous MTFCs, leading to high power densities. In fact, MTFC power density is generally increased by at least a factor of 5 when a single copper wire is added as a cathode conduction layer as seen in Table 6.1, such as MTFC #7, #8, and #9. The exceptions are MTFC #12 and #17 which do not show a marked increase in power density due to the addition of a copper wire at the cathode. This is expected with MTFC #12 where the addition of another conduction layer, i.e. a wire wrap on top of the already existent cathode-side silver coating, should not increase electron conduction noticeably and could actually cause a slight decrease in the oxygen reaching the catalyst layer. The poor performance of MTFC #17 when wire wrapped is probably due to the fact that ohmic losses are not the dominating losses, but instead are most likely the extremely high activation losses. These abnormally high activation losses might be due to the method of cell construction. MTFC #17 was the only cell of those tested that used a 1 molar tetrabutyl ammonium (TBA) cation to convert the Nafion™ to a TBA counterion. According to the literature (Phillips and Moore, 2006), this TBA counterion should allow for higher processing temperatures and better membrane properties than Nafion™ in the sodium form. Usually the Nafion™ is converted to a sodium form that allows higher temperatures to be used when adhering the catalyst layers. The conversion to sodium form is accomplished by immersing the Nafion™ in a sodium hydroxide solution for a

time. However, there might have been a problem in the cell construction with the TBA conversion.

Figure 6.18 shows the highest open circuit voltage (0.869 v) attained by any of the MTFCs. As seen in Figure 6.15, the open circuit voltage attained by MTFC #4 was only 0.574 v. The rise in open circuit voltage from MTFC #4 to MTFC #9 is due in large part to cell conditioning. In the beginning stages of the research, the conditioning time for

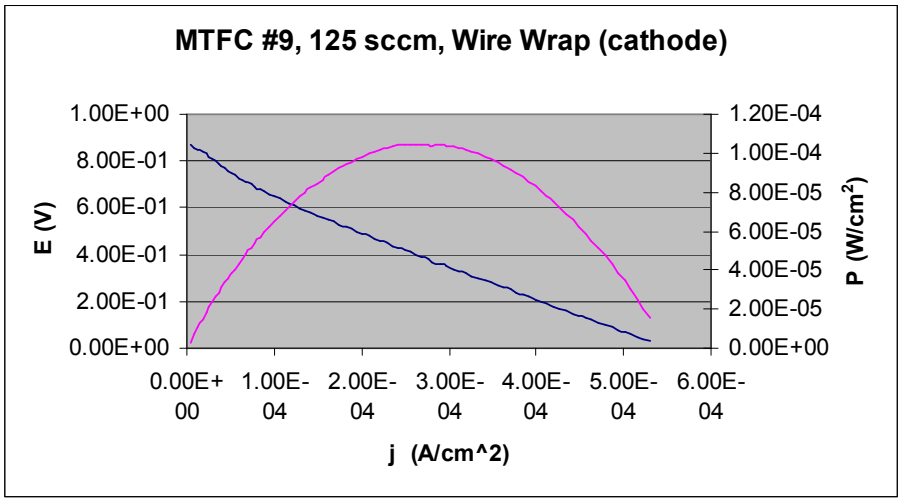

Figure 6.18 Polarization curve of MTFC #9 at 125 sccm of $H_2$with a wire wrap as the cathode conduction layer

cells was very low (less than a minute), while the conditioning time for MTFC 9 was several minutes (about 16 minutes). The cell conditioning method described in Section 4.3.4 of Chapter 4 was prompted primarily because of the difference that cell conditioning appeared to have on the open circuit potential of the cell. Furthermore the main factor on polarization curve smoothness for MTFCs was found to be cell conditioning. Figures 6.19 and 6.20 show polarization curves for MTFC #15. Both curves were taken only 1 hour and 6 minutes apart under the same conditions. The time between the tests allowed for better cell conditioning resulting in the smooth polarization curve seen in Figure 6.20.

In addition to the many polarization curves generated, several EIS tests were taken

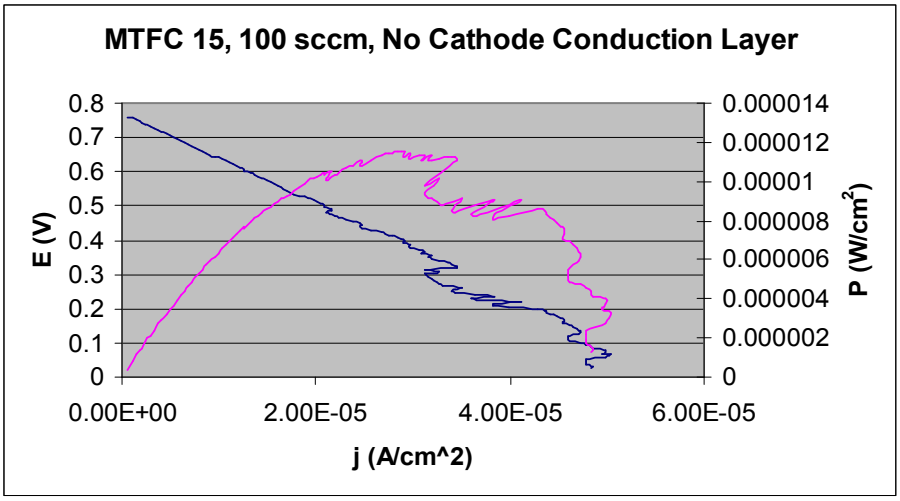

Figure 6.19 Polarization curve of MTFC 15 at 100 sccm with no conduction layers added.

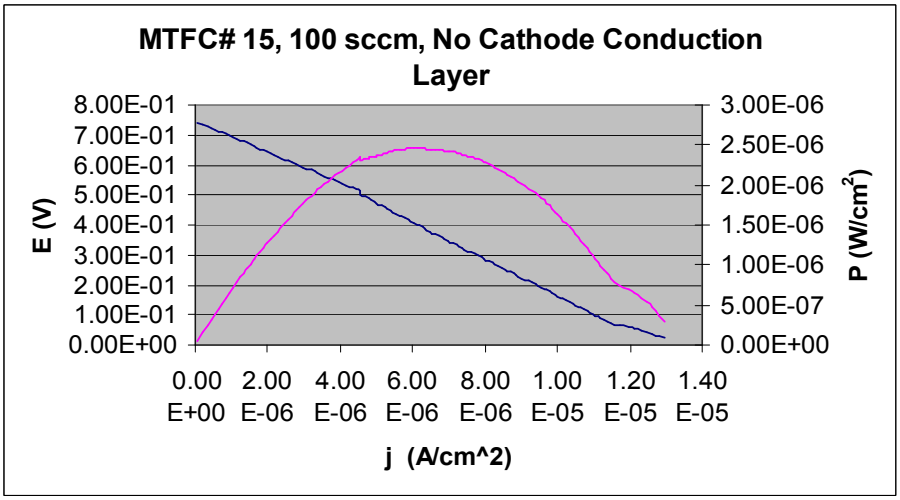

Figure 6.20 Polarization curve of MTFC 15 at 100 sccm with no conduction layers on both anode and cathode

for various cells. The results of these tests provide some insight to the losses occurring in each cell recorded in a Nyquist diagram (see Chapter 4). Thus the minimum real impedence (see Figure 6.21, and Table 6.1) is a measure of the ohmic losses of the cell. The various losses are shown as a function of position in the EIS curve of a hypothetical flate-plate cell as shown in Figure 6.21. Tubular losses should follow a similar pattern.

Initial tests produced poor results. Figure 6.22 shows the results for the first EIS

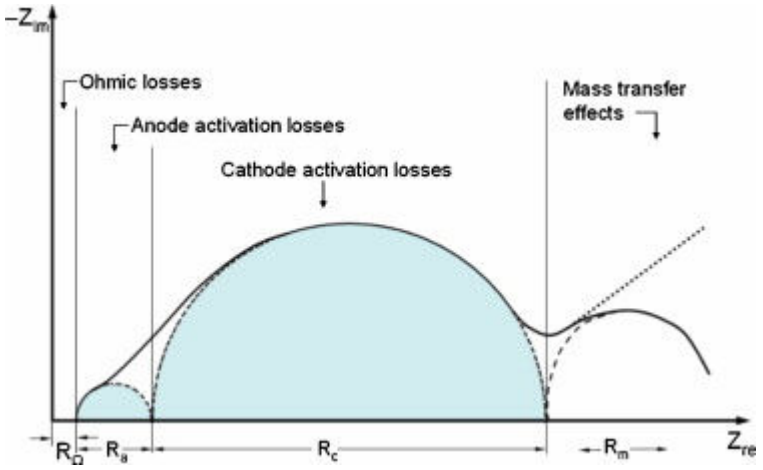

Figure 6.21 Nyquist plot of hypothetical flat-plate PEMFC by Zhu, Payne, and Tatarchuk (2007)

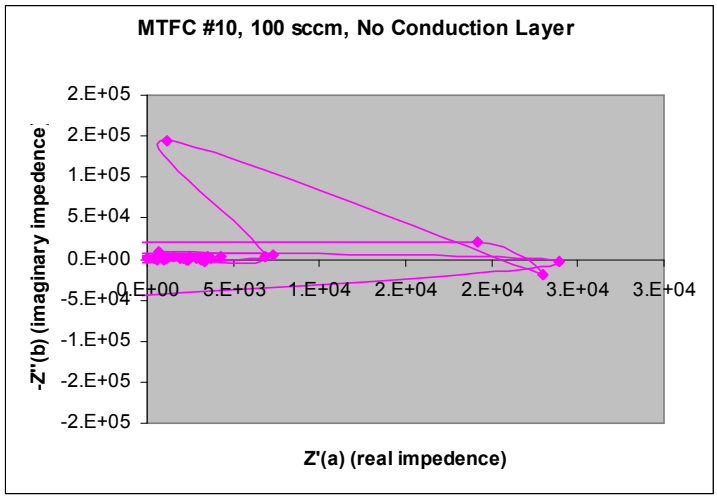

Figure 6.22 Nyquist diagram of MTFC 10 with no cathode conduction layer

test. The data in this figure is unusable. It was found that the AC and DC currents were set too high in the initial tests and that the ratio between them was incorrect. The initial test used machine defaults with the DC current of 1 A, and the AC current of .1 A. The settings that produce the best results for MTFCs are a DC current that of about ½ the maximum current of the cell, and an AC current of ½ the DC current. On both MTFC #7 and #2 VT it was shown that by placing a copper wire on the cathode side the minimum real impedance was reduced by an order of magnitude. Figure 6.23 shows the EIS curve of MTFC #2 VT without a cathode conduction layer, but with a helically wrapped copper wire for the anode conduction layer. Figure 6.24 shows the EIS curve of MTFC #2 VT with cathode and anode conduction layers of helically wrapped copper wires. Note that

the curve shape is almost identical, but is shifted by the addition of the cathode conduction layer. Also, it should be noted that the distinction between anode and cathode

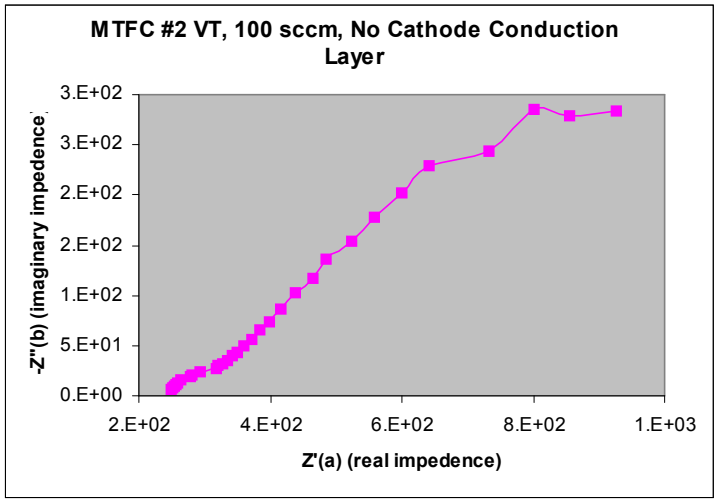

Figure 6.23 Nyquist diagram of MTFC VT 2 with no cathode conduction layer, and a helically wrapped wire as the anode conduction layer

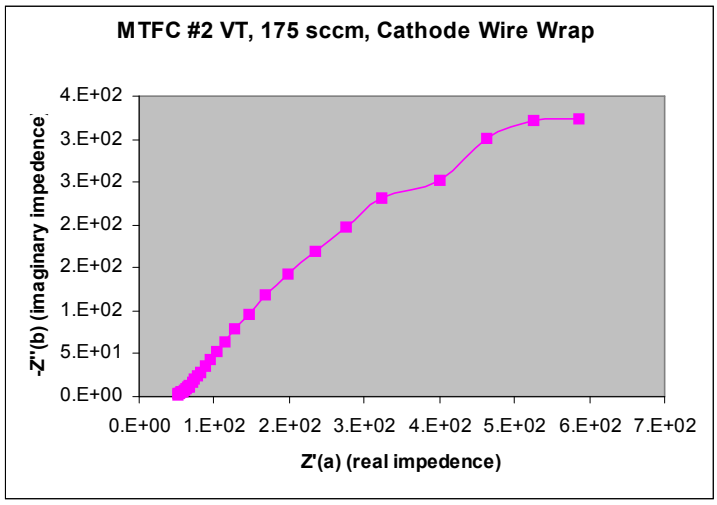

Figure 6.24 Nyquist diagram of MTFC VT 2 with a wire wrapped cathode conduction layer, and a helically wrapped wire as the anode conduction layer

activation losses is not readily apparent. This could be due to either the domination of the cathode activation losses or a loss of significance due to the small currents produced by the cells.

The performance of the MTFCs created by Luna Innovations, Inc. is relatively poor when compared with other tubular fuel cells in the literature. This could be due to several different issues.

Electron conduction is key to fuel cell performance; if the electron conduction paths are poor it will lead to poor performance. It can be seen in the results presented above that by enhancing the conduction layers, i.e. conduction pathways, of the MTFCs an increase on the range of half an order of magnitude to a full order of magnitude can be achieved. The EIS curves in Figures 6.18 and 6.19 also show that the ohmic losses of MTFCs can be significantly reduced by effective conduction layers.

Of course, another issue is that of contact resistances between the conduction layers and the MEA, and between the catalyst layers and the Nafion™ membrane. Due to the methods used in manufacturing the MTFC conduction layers, contact resistances could be high. For example the wire wrap conduction layer which is wrapped by hand always has several locations along the axis of the cell where the MEA and the wire do not contact each other fully. Also, contact resistance between the catalyst layers and the Nafion™ membrane could be high because the current method used for hot-pressing the cells is very poor. Hot-pressing would help to ensure smaller contact resistances between the catalyst layer and the membrane by creating a better interface between the layers to enhance the conduction of protons, which is likely inhibiting the effectiveness of the MTFCs' 3-phase boundary region.

Another possible source of loss could be due to the extrusion process used to create the Nafion™ tubes used for the MEAs. This process could cause an anisotropic rearrangement of the proton conducting sites which favor the axial as opposed to the radial direction, thus, impeding the transfer of protons from anode to cathode.

Finally, the exchange current density found for MTFC #7 is 4.74518E-07 A/cm^2, which is very small compared to the value for the data given by Eshraghi et al. (2005) of 1.4193E-03 A/cm^2. This could also explain the lower open circuit voltages that have been attained by the MTFCs.

6.3 MTFC Model Results

The lumped-parameter MTFC model implemented in iSCRIPT™ (see Chapter 5) provides an estimation of MTFC performance based upon first principles. The results of this model are compared with experimental data taken from the patent application of Eshraghi et al.(2005), the owners of Microcell Corp., the CFD model by Coursange, Hourri, and Hamelin (2003) and with experimental data taken from cells produced by Luna Innovations, Inc. These results can be seen in Figures 6.25, 6.26, and 6.27.

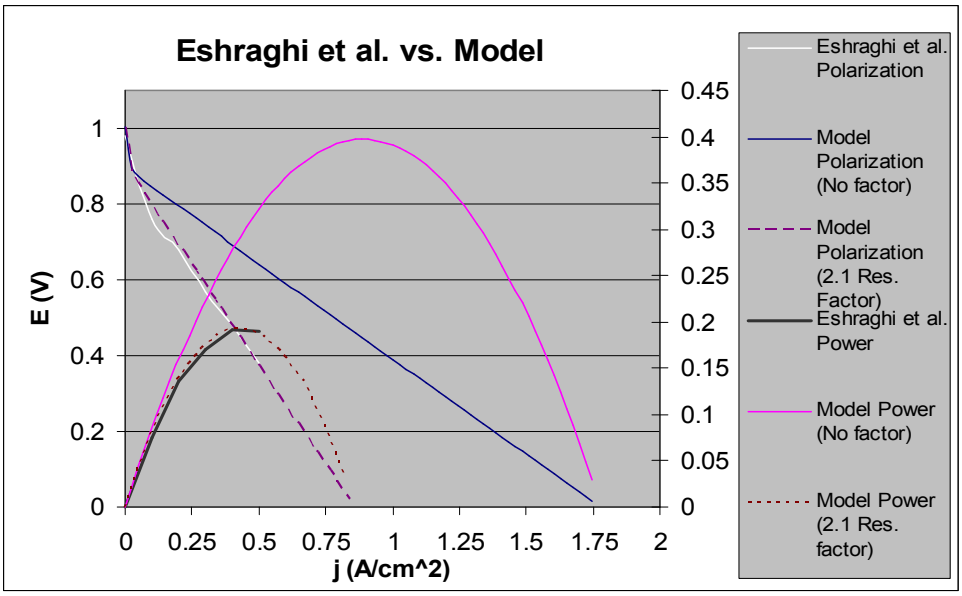

Figure 6.25 Comparison of polarization and power curves generated by MTFC model and from experimental data found in the patent application of Eshraghi et al. (2005)

Figure 6.25 shows the performance estimated by the model without a resistance factor, and the performance when the membrane resistance is increased by a factor of 2.1. The data from Eshraghi et al. was obtained by visual extrapolation of the polarization curve from the patent application. Using the polarization curve of Eshraghi et al. the exchange current density was found to be 1.419 E-3, which is used in the model estimation. The resistance factor used is reasonable when considering the unknowns involved with the Eshraghi et al.(2005) data such as membrane thickness, Nafion™ properties, and error in data extrapolation. The membrane thickness used in the comparison was 0.015 cm, this corresponds to the most commonly used membrane thickness used by Luna Innovations, Inc. which is assumed to be similar to that used by Eshraghi et al. The Nafion™

properties assumed are a 1970 kg/m^3 dry density of and a Nafion™ equivalent weight of 1 mol/kg, which are average values for flat-plate cell membranes. It can be seen that the initial portion of the curve does not fit exactly. This initial portion of the polarization curve is shaped mainly by the activation losses of the cell. The difference in this could be due to such factors as the cell temperature and humidification of reactants. Cell temperature is assumed to be 353^{o}K, while the relative humidities are assumed to be 80% and 90% for the anode and cathode, respectively.

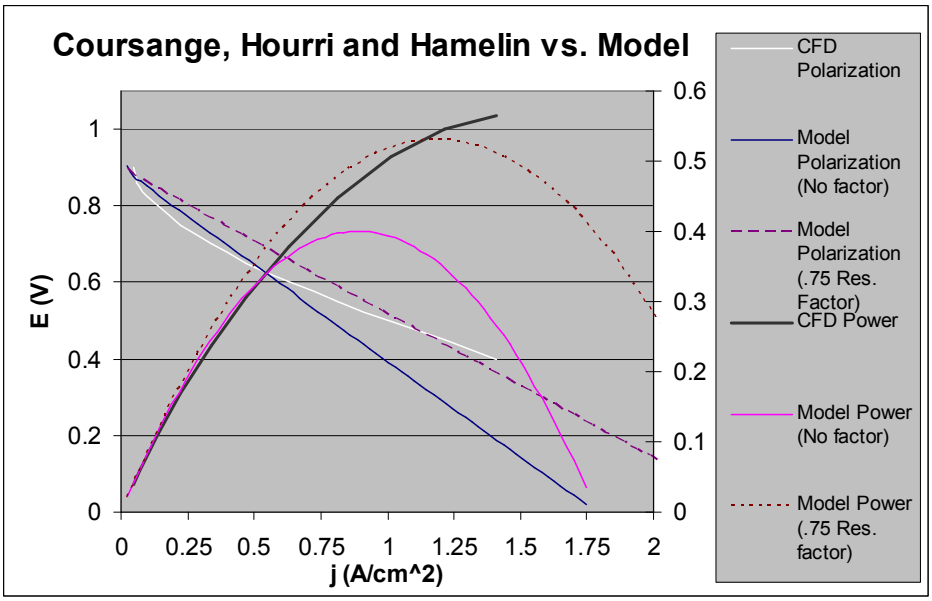

Figure 6.26 Comparison of polarization and power curves generated by MTFC model and from the modeling estimates of Coursange, Hourri, and Hamelin (2003)

Figure 6.26 shows the results of the Coursange, Hourri, and Hamelin (2003) CFD model for a tubular fuel cell, and the MTFC model estimation for the same system (this system is described in detail in Chapter 2). A current exchange density of 4.90 E-3 was found using the polarization curve of the results of Coursange, Hourri, and Hamelin (2003) which was implemented in the MTFC model. The membrane thickness used in the comparison was 0.015 cm, which corresponds to the membrane thickness most used by Luna Innovations, Inc. and is assumed to be similar to that used by Coursange, Hourri, and Hamelin (2003). The Nafion™ properties assumed are 1970 kg/m^3 dry density, and a Nafion™ equivalent weight of 1 mol/kg, which are average values for flat-plate cell membranes. Cell temperature is assumed to be 353^{o}K, while the relative humidities are

assumed to be 80% and 90% for the anode and cathode, respectively. Using these parameters it is found that the MTFC model predicts a lower performance than that predicted by Coursange, Hourri, and Hamelin (2003). Even when the results are shifted using a factor of .75 on the membrane resistance the MTFC model and the Coursange, Hourri, and Hamelin (2003) do not have the same shapes. Also the shape of the data of Coursange, Hourri, and Hamelin (2003) is different than that produced by Eshraghi et al. (2005) and the experimental data of the MTFCs developed by Luna Innovations, Inc. This difference in polarization and power curve shape could be attributed to several different factors. The polarization curve presented by Coursange, Hourri, and Hamelin (2003) (Figure 2.9) can be extrapolated to show that the open circuit voltage calculated is around 1.1 volts, which leads to the conclusion that the activation losses calculated are much lower then those seen experimentally.

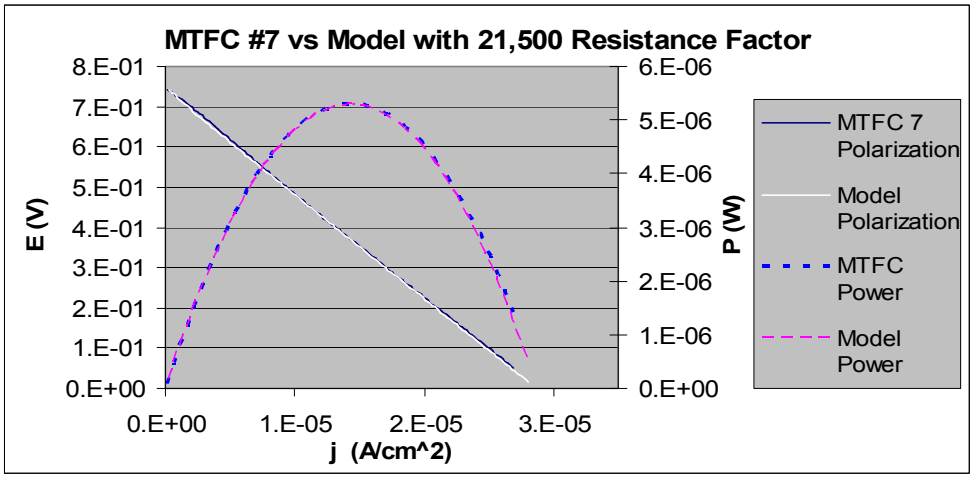

Figure 6.27 Comparison of polarization and power curves generated by MTFC model and by MTFC 7

The data generated for Figure 6.27 by the lumped-parameter MTFC model requires an increase in the overall resistance by a factor 21,500. Such a large resistance factor and such poor cell performance could be due to several different reasons. One of the assumptions of the model is that contact resistance between the different layers is small or negligible. It is thought that the poor performance of the MTFC cells currently being produced is due to very poor contact between the catalyst layers and the membrane. This poor contact would cause a very large resistance which is not accounted for in the model.

Furthermore, the values assumed for the Nafion™ properties of the cell (a 1970 kg/m^3 dry density, and a Nafion™ equivalent weight of 1 mol/kg) are the average values for flat-plate cells, which may have been altered by the method used by Perma Pure, Inc.(the manufacturer of the Nafion™ tubing used in our MTFCs). The method used for creating the Nafion™ tubing is an extrusion process that prepares tubes which are generally used to hydrate gases. This extrusion process could also have several effects on the membrane that could cause poor performance. For example the Nafion™ density and equivalent weight could be altered by the extrusion process as the material is heated, compressed, and forced through the die. In fact, the extrusion may cause an anisotropic rearrangement of the proton conducting sites which favor the axial as opposed to the radial direction, thus impeding the transfer of protons from the anode to cathode. In addition, the process of pulling Nafion™ through the die might also cause some surface hardening effects to the point where the catalyst layers might not bond well to the surface of the membrane. This would create a disconnect between the catalyst layers and the membrane which would greatly inhibit the transfer of protons across the membrane.

Another reason that a disconnect might be occurring between the catalyst layers and the membrane could be that the tubular shaped cells are difficult to hot-press after the catalyst layers have been painted on. MTFCs #13 and #16 were hot-pressed by Luna Innovations, Inc. The process used to hot-press these cells is as follows. A small stainless steel tube is placed on the anode side of the cell. Then the cell is then placed in a groove on an aluminum block which has machined grooves for different sizes of various cell diameters. A matching block is then placed on top and the assembly is bolted together and tightened by a torque wrench, after which the assembly is placed in an oven for a period of time. After the assembly has been removed from the oven and been taken apart, the stainless steel tube and the cell are put in water to allow the cell to swell and release the stainless steel tube. Much of the problem with this method of hot-pressing is that it is impossible to know how much the tube has actually been pressed. For example, the diameter of MTFC #13 was too small for the groove in the aluminum block, so it was not well pressed. Other problems with this method include pinching of the membrane if the groove is slightly too small. Currently, research is being conducted to determine the

effectiveness of the current hot-press method and determine if some new approach is needed.

The MTFC lumped parameter model was also used to see the effect of varying membrane thickness on the MTFCs. Figure 6.28 shows the model prediction of the effect

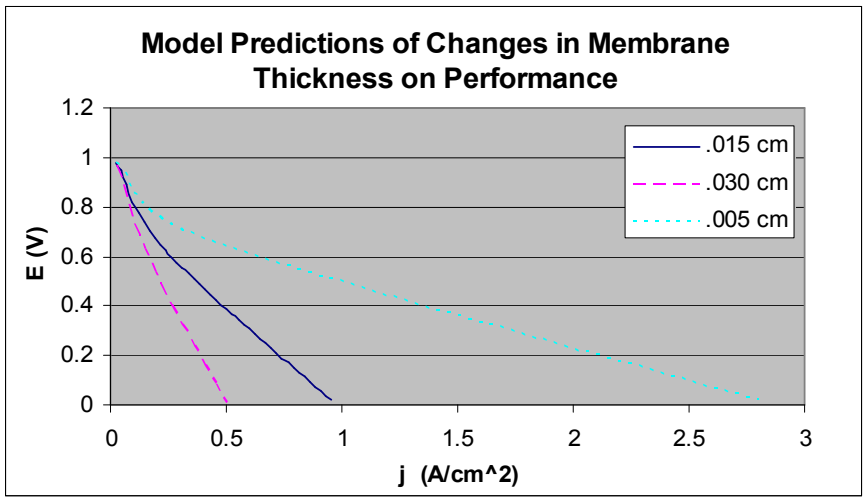

Figure 6.28 Effect of varying membrane thickness on cell performance generated by lumped-parameter MTFC model.

of varying membrane thickness on cell performance, an effect of which appears to be linear. By doubling the thickness of the membrane, the current density is approximately halved. By decreasing the thickness by a factor of three the current density is increased approximately by a factor of 3. This agrees with the conclusions reached by Teranishi et al.(2005) who observe that if the water content in membranes of different thicknesses is equal, then membrane impedance would be approximately proportional to membrane thickness. The water content in all three sets of data is, in fact, assumed equal. Also, as membrane thickness increases, resistance to proton conduction across the membrane intensifies. This supports the results found by the model.

The model is also used to predict the effect of conduction layers on cell performance. Figure 6.29 shows the model prediction for a cell without conduction layers and a cell with a wire wrap on the cathode side and a wire stretched on the anode side. The increase in performance found is slightly less than one order of magnitude. These results are consistent with the experimental data taken. The addition of a wire wrap as

discussed in Section 6.2 generally leads to an increase in current by about a factor of 5 when only the cathode is wrapped. A similar increase is seen by placing a wire on the

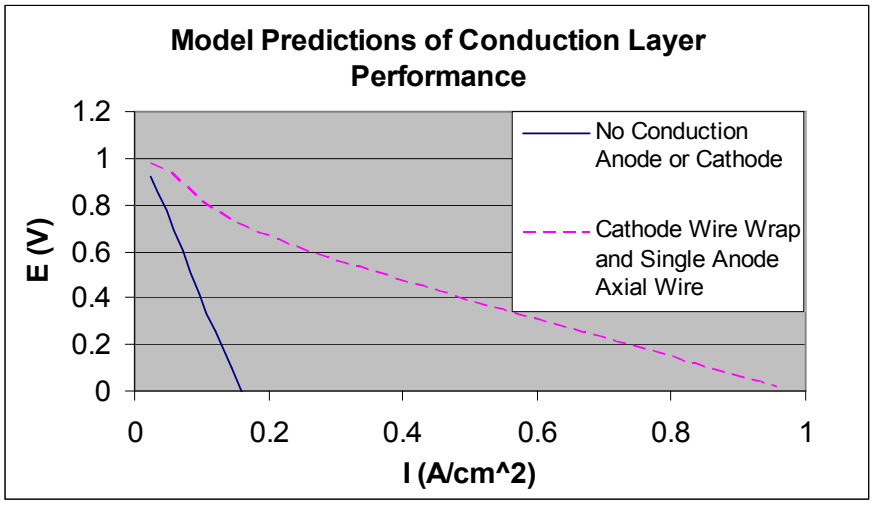

Figure 6.29 Effect of varying conduction layers on cell performance generated by MTFC model

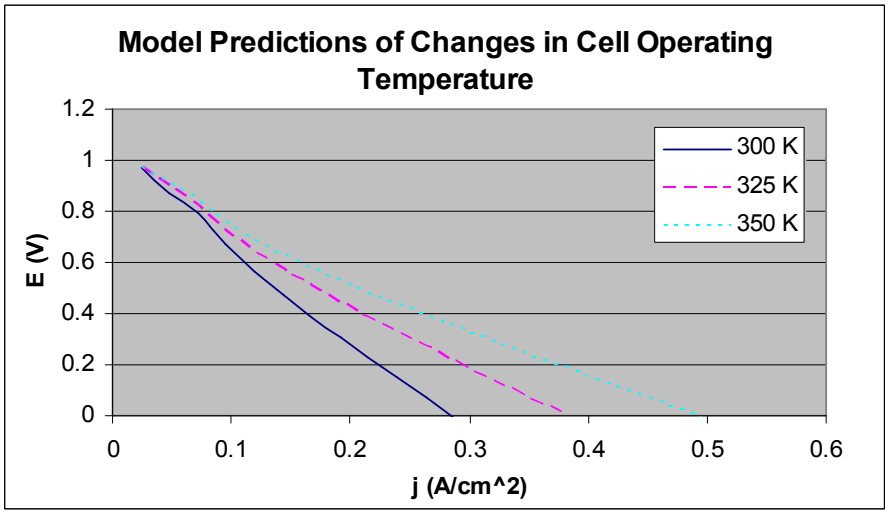

Figure 6.30 Effect of varying cell operating temperature on cell performance generated by MTFC model

anode side of the membrane.

The effects of temperature on cell performance are also explored with the lumped parameter MTFC model. Figure 6.30 shows the model predictions of the effects of varying temperatures. As can be seen, as the temperature of the cell is raised, the current

density improves. This is what would be expected for a PEMFC type cell. As temperature is increased, the thermal energy of the reactants in the cell is also raised. By raising the this energy the activation energy required to initiate a reaction is decreased. Of course, one temperature effect that the model does not take into account directly (i.e. without manually changing the value) is the change of the exchange current density with changes in temperature. Changing the temperature of the cell has an exponential effect on the exchange current density (O'Hayre, 2006). As discussed above the exchange current density for MTFC #7 was found experimentally, and all experiments were done at room temperature. Thus, the results for the temperatures of 325^{o}K and 350^{o}K shown in Figure 6.30 are lower than they would be in actuality.

Chapter 7

Conclusions

The results of the feasibility study have been presented showing that fuel cells could be used to replace batteries as the MAV energy source. It was also found that a fuel cell system configuration of methanol fuel at 3.25 molarity using wicking technology could potentially provide a 50% increase in overall power output over the current battery technology. Results from the feasibility study also indicate that by using sodium borohydride hydrogen source a 33% increase in overall power output is possible, while also decreasing the mass of the power production system.

Micro-tubular fuel cells (MTFCs) have been tested to show that these cells are a possibility for energy production in MAVs only if improvements are made to current energy production. The MTFC tests also show the development and improvement gained in collaboration between Luna Innovations, Inc. and the Center for Energy Systems Research at Virginia. Through testing and iterative designing an increase of three orders of magnitude of the maximum power production of MTFCs, constructed by Luna Innovations, Inc., has been realized. More progress, however, is needed to bring the MTFC up to the performance level required for a successfully fuel cell powered MAV.

Also an isothermal, lumped-parameter model for MTFCs has been developed to predict MTFC behavior. The use of this lumped-parameter model aids in understanding the dominant losses of the cell and methods to improve cell performance. A comparison of the lumped-parameter MTFC model using the experimental results from MTFC testing, and experimental results from the literature was performed. The performance improvements of the cells produced by Luna Innovation Inc. have been substantial. The MTFC model and the data from Eshraghi et al. show that there remains much improvement to be accomplished. The MTFC model can be used to pinpoint the effect of design modifications on cell performance to eliminate unnecessary or poor design changes.

References

Amendola, S.C., Binder, M., Sharp-Goldman, S.L., Kelly, M.T., and Petillo, P.J., inventors, 2003, United States Patent for System of Hydrogen Generation, Patent # US 6,534,033 B1, Date of Patent March 18, 2003, Assignee: Millennium Cell Inc.

Ames, J., Ancarrow, D., Durkin, B., Feucht, P., Leatherbury, E., Moyer, M., Sloan, R., Williams, D., and Zwerko, K., 2006, "Fuel Cell Research Report, Phase VIII – Direct Methanol/Formic Acid Delivery Fuel Cell," preliminary system design report, ME4015 – Senior Capstone Design Course, advisor: Prof. Michael R. von Spakovsky, Virginia Tech, Department of Mechanical Engineering, Blacksburg, VA.

Batteryspace.com, 2006, product specification pages www.batteryspace.com.

Ceraolo M., Miulli, C., and Pozio, A., 2002, "Modelling Static and Dynamic Behavior of Proton Exchange Membrane Fuel Cells on the Basis of Electro-Chemical Description," Journal of Power Sources, 113 (2003), pp. 131-144.

Coursange, J.-F., Hourri, A., and Hamelin, J., 2003, "Performance Comparison Between Planar and Tubular-Shaped PEM Fuel Cells by Three-Dimensional Numerical Simulation," Fuel Cells, Volume 3, Number 1-2, pp. 28-36.

Eshraghi, R.R., Lin, C., Lin, J.C., Ketterer, 2005 United States Patent for Microfibrous Fuel Cell Assemblies comprising Fiber-Supported Electrocatalyst Layers, and Methods of Making Same, Patent # 20050151269, Date of Patent August 18, 2005 Assignee: Microcell Corporation.

Green, K.J., Slee, R., and Lakeman, J.B., 2002, "The Development of Lightweight, Ambient Air Breathing, Tubular PEM Fuel Cell," Journal of New Materials for Materials for Electrochemical Systems, Volume 5, pp. 1-7.

Gunter, J., 2007, "Space Efficient Fuel Cell Fibers for Micro Air Vehicles (MAV)," U.S. Air Force – Air Force Research Lab – Munitions Directorate –Eglin AFB Contract No. FA8651-06-M-0192, Phase I Final Report.

Gunter, J, 2007, Private communications with Research Engineer of the Advanced Materials Group of Luna Innovations, Inc.

Guo, Z. and Cao, Y., 2004, "Passive fuel delivery system for portable direct methanol fuel cells," Journal of Power Sources, 132 (2004), pp. 86–91.

Joint Service Pollution Prevention and Sustainability Technical Library, 2005, "Impacts of the Energy Policy Act of 2005 on Federal Facility Operations," 11/14/2007, http://p2library.nfesc.navy.mil/issues/emergeoct2005/index.html

Kallender, P., 2005, "IBM, Sanyo Announce Fuel Cell Prototype," InfoWorld.com, http://www.infoworld.com/article/05/04/11/HNfuelcellprototype_1.html

Kehoe, J., Causey, R., Abdulrahim, M., and Lind, R., 2005, "Waypoint Navigation for a Micro Air Vehicle using Vision-Based Attitude Estimation," *Proceedings of the 2005 AIAA Guidance, Navigation, and Control Conference*, San Francisco, CA.

Kimble, M.C., Anderson, E.B., Jane, K.D., Woodman, A.S., and Legner, H.H., 2000, "Electrochemical Performance of a Multi-Tubular Fuel Cell and Electrolyzer Array," Intersociety Energy Conversion Engineering Conference and Exhibit (IECEC), 35th, Las Vegas, NV, July 24-28, 2000, Collection of Technical Papers. Vol. 1 (A00-37701 10-44)

Larminie, J. and Dicks, A., 2003, Fuel Cell System Explained, pp. 145, 148, and 149.

Lu, G.Q., Wang, C.Y., 2005, "Development of micro direct methanol fuel cells for high power applications," Journal of Power Sources, 144, pp 141–145.

Lt. Crosby, 2006, Private communications with AFOSR program manager.

MAV Lab. University of Florida, 2007, "UF MAV Lab homepage," http://www.mae.ufl.edu/mav/ , 12/11/07

Mench, M.M., Wang, Z.H., Bhatia, K., and Wang, C.Y., 2001, "Design of a micro direct methanol fuel cell (μDMFC)," International Mechanical Engineering Congress and Exposition (IMECE), New York, New York, USA, November 11-16.

O'Hayre, R., Cha, S.W., Colella, W., and Prinz, F.B., 2006, "Fuel Cell Fundamentals," John Wiley & Sons, Inc, Hoboken, New Jersey, pp 39, 47, 79, 116, 119, 143-147, 186.

Okada, T., 2002, "Micro-Tubular Fuel Cell, A New Model of Fuel Cell for Mobile Applications", *AIST Today* Vol. 2, No. 6, pp. 11.

PCworld.com, 2007, "Toshiba's Fuel Cell Laptop", http://www.pcworld.com/video/id,461-page,1-bid,0/video.html

Perma Pure LLC, 2007, Nafion™ Tubing specifications http://www.permapure.com/Products/NafionTubing.htm

Phillips, A.K., and Moore, R.B., 2006, "Mechanical and transport property modifications of perfluorosulfonate ionomer membranes prepared with mixed organic and inorganic counterions", Journal of Polymer Science Part B: Polymer Physics Vol. 44, No. 16, pp. 2267-2277.

power one, 2006, power one product information www.powerone-batteries.com.

Springer, T.E., Zawodzinski, T.A., and Gottesfeld, S., 1991 "Polymer Electrolyte Fuel Cell Model," Journal of Electrochemical Society, Volume 138, No. 8, pp. 2334-2342

Siegel, N.P., 2003, "Development and Validation of a Computational Model for a Proton Exchange Membrane Fuel Cell," Digital Library and Archives, ETDs @ VT, 12/15/07, http://scholar.lib.vt.edu/theses/available/etd-01202004-135932/

Teranishi, K., Tsushima, S., and Hirai, S., 2005,"Study of the Effect of Membrane Thickness on the Performance of Polymer Electrolyte Fuel Cells by Water Distribution in a Membrane", Electrochemical and Solid-State Letters, 2005, Vol. 8, No. 6, pp. A281–A284.

Thunder Power Batteries, 2006, Thunder Power Batteries product information www.thunderpower-batteries.com.

Toshiba, 2004, "Toshiba's Methanol Fuel Cell", http://www.dpreview.com/news/0406/04062401toshibafuel.asp

Vielstich, W., Lamm, A., and Gasteiger, H.A., editors, 2003, "Handbook of Fuel Cells Fundamentals, Technology and Applications - Volume 3: Fuel Cell Technology and Applications: Part 1," pp. 86-87.

Williams, M., 2006, "Panasonic Shows Laptop Fuel Cell," PCworld.com, http://www.pcworld.com/article/id,124244/article.html

Yeom, J., Jayshree, R.S., Rastogi, C., Shannon, M.A., and Kenis, P.J.A., 2006, "Passive direct formic acid microfabricated fuel cell," Journal of Power Sources, in press, available on the web at www.elsevier.com.

Yeom, J., Mozsgai, G.Z., Flachsbart, B.R., Choban, E.R., Asthana, A., Shannon, M.A., and Kenis, P.J.A., 2005, "Microfabrication and characterization of a silicon-based millimeter scale, PEM fuel cell operating with hydrogen, methanol, or formic acid," Sensors and Actuators B Volume 107, pp. 882-891.

Yi, J.S., and Nguyen, T.V., 1998, "An Along-the-Channel Model for Proton Exchange Membrane Fuel Cells," Journal of Electrochemical Society, Volume 145, No. 4, pp. 1149-1159

Zhu, W.H., Payne, R.U., Tatarchuk, B.J., 2007, "PEM Stack Test and Analysis in a Power System at Operational Load Via AC Impedance," Journal of Power Sources, Volume 168, Issue 1, pp. 211-217.

Copyright Permissions

Figures 1.1 and 1.2 reprinted from the "UF MAV Lab homepage,", http://www.mae.ufl.edu/mav/ MAV Lab. University of Florida, 2007, 12/11/07 with permission from Dr. Peter Ifju.

Figure 2.1 reprinted from the Journal of Electrochemical Society, Volume 138, No. 8, pp. 2334-2342, Springer, T.E., Zawodzinski, T.A., and Gottesfeld, S., 1991 "Polymer Electrolyte Fuel Cell Model," with permission from The Electrochemical Society.

Tabels 2.1 and 2.2 reprinted from PhD dissertation of Siegel, N.P., 2003, "Development and Validation of a Computational Model for a Proton Exchange Membrane Fuel Cell," Digital Library and Archives, ETDs @ VT, 12/15/07, http://scholar.lib.vt.edu/theses/available/etd-01202004-135932/ with permission from Dr. Nathan Siegel

Figures 2.2 and 2.3 reprinted from the Journal of Electrochemical Society, Volume 145, No. 4, pp. 1149-1159, Yi, J.S., and Nguyen, T.V., 1998, "An Along-the-Channel Model for Proton Exchange Membrane Fuel Cells," with permission from The Electrochemical Society.

Figures 2.4, 2.5, and 2.6 reprinted from the Journal of Power Sources, 113 (2003), pp. 131-144, Ceraolo M., Miulli, C., and Pozio, A., 2002, "Modelling Static and Dynamic Behavior of Proton Exchange Membrane Fuel Cells on the Basis of Electro-Chemical Description," Copyright (2003), with permission from Elsevier.

Figures 2.7, 2.8, and 2.9 reprinted from Fuel Cells, Volume 3, Number 1-2, pp. 28-36, Coursange, J.-F., Hourri, A., and Hamelin, J., 2003, "Performance Comparison Between Planar and Tubular-Shaped PEM Fuel Cells by Three-Dimensional Numerical Simulation," Copyright Wiley-VCH Verlag GmbH & Co. KGaA. Reproduced with permission.

Figures 2.10, 2.11, 2.12, 2.13, 2.14, 3.2, 3.3, 3.4, and 6.14 reprinted from Sensors and Actuators B Volume 107, Yeom, J., Mozsgai, G.Z., Flachsbart, B.R., Choban, E.R., Asthana, A., Shannon, M.A., and Kenis, P.J.A., "Microfabrication and characterization of a silicon-based millimeter scale, PEM fuel cell operating with hydrogen, methanol, or formic acid" pp. 882-891, Copyright (2005), with permission from Elsevier.

Figures 2.15, 2.16, and 2.17 reprinted from Green, K.J., Slee, R., and Lakeman, J.B., 2002, "The Development of Lightweight, Ambient Air Breathing, Tubular PEM Fuel Cell," Journal of New Materials for Materials for Electrochemical Systems, Volume 5, pp. 1-7.

Figures 2.18, 2.19, 2.20, 2.21, 2.22, 2.23, and 2.24 reprinted from Kimble, M.C., Anderson, E.B., Jane, K.D., Woodman, A.S., and Legner, H.H., 2000, "Electrochemical Performance of a Multi-Tubular Fuel Cell and Electrolyzer Array," Intersociety Energy Conversion Engineering Conference and Exhibit (IECEC), 35th, Las Vegas, NV, July 24-28, 2000, Collection of Technical Papers. Vol. 1 (A00-37701 10-44), reprinted by permission of the American Institue of Aeronautics and Astronautics, Inc.

Figures 3.1, and 4.7 reprinted from Phase I Final Report, Gunter, J., 2007, "Space Efficient Fuel Cell Fibers for Micro Air Vehicles (MAV)," U.S. Air Force – Air Force Research Lab – Munitions Directorate –Eglin AFB Contract No. FA8651-06-M-0192, reproduced by permission from Jonas Gunter.

Figures 3.6 and 3.7 reprinted from Journal of Power Sources, 132 (2004), pp. 86–91, Guo, Z. and Cao, Y., 2004, "Passive fuel delivery system for portable direct methanol fuel cells," Copyright (2004), with permission from Elsevier.

Figures 3.8, 3.9, 3.10, and 3.11 reprinted from Senior Capstone Design Final Report, Ames, J., Ancarrow, D., Durkin, B., Feucht, P., Leatherbury, E., Moyer, M., Sloan, R., Williams, D., and Zwerko, K., 2006, "Fuel Cell Research Report, Phase VIII – Direct Methanol/Formic Acid Delivery Fuel Cell," preliminary system design report, ME4015 – Senior Capstone Design Course, advisor: Prof. Michael R. von Spakovsky,

Virginia Tech, Department of Mechanical Engineering, Blacksburg, VA, with permission from Dr. Michael R. von Spakovsky.

Table 4.2 reprinted from Private communications with Research Engineer of the Advanced Materials Group of Luna Innovations, Inc.Gunter, J, 2007, reproduced by permission from Jonas Gunter.

Figure 4.17 and 6.21 reprinted from Journal of Power Sources, Volume 168, Issue 1, pp. 211-217, Zhu, W.H., Payne, R.U., Tatarchuk, B.J., 2007, "PEM Stack Test and Analysis in a Power System at Operational Load Via AC Impedance," Copyright (2007), with permission from Elsevier.

Appendix A

Tables of Feasibility Study Calculations

The equations used to generate the values found in the tables are found in Section 3.1.

Table A1 Evaluation of the leading battery technology for MAV power plants.

	Volume (cm^3)	Weight (kg)	Voltage (V)	Capacity (mAhr)	W hr/cm^3	W hr/kg	W hr
Li-ion polymer	24.78	0.054	11.1	850	0.3808	174.7222	19.4982
Thunder Power I	68	0.142	11.1	2100	0.3428	164.1549	17.5545
Thunder Power II	51.210	0.133	11.1	2100	0.4552	175.2632	23.3102
Ni-MH	3.595	0.013	1.2	850	0.2837	78.4615	14.5297
Ni-Cd	7.918	0.020	1.2	1000	0.1516	60.6061	7.7611
Zinc air	0.265	0.00083	1.4	330	1.7434	556.6265	89.2793

Table A2a Evaluation of hydrogen as a fuel in conjunction with PEM technology for MAV power plants.

Hydrogen	Volume tank (cm^3)	R J/(mol *K)	Temp. (K)	Δho (kJ/mol)	Moles	W hr/cm^3	W hr/kg	W hr
(pressurized tank)	33.58	8.3145	298	-242	0.54197	0.4340	236.8334	14.573
5800 PSI	Pressure (psi)	Pressure (Pa)	Efficiency	Voltage (V)	Capacity (mAhr)			
	5800	4.00E+07	0.4	12	1214.414			
Hydrogen	Volume tank (cm^3)	R J/(mol *K)	Temp. (K)	Δho (kJ/mol)	Moles	W hr/cm^3	W hr/kg	W hr
(pressurized tank)	33.58	8.3145	298	-242	0.93443	0.7482	426.1228	25.125
10,000 PSI	Pressure (psi)	Pressure (Pa)	Efficiency	Voltage (V)	Capacity (mAhr)			
	10000	6.89E+07	0.4	12	2093.8186			
Hydrogen	Volume (cm^3)	R J/(mol *K)	Temp. (K)	Δho (kJ/mol)	moles	W hr/cm^3	W hr/kg	W hr
Metal Hydride	51.210	8.3145	298	-242	0.71924	0.3777	87.9078	19.339
	System	H2	Efficiency	Voltage (V)	Capacity			
	0.22	0.00145	0.4	12	1611.6439			
Hydrogen	Total Volume (cm^3)	R J/(mol *K)	Temp. (K)	Δho (kJ/mol)	moles	W hr/cm^3	W hr/kg	W hr
Sodium Borohydride	51.210	8.3145	333	-242	1.1906	0.6252	611.8897	32.015
NaBH4	System Weight (kg)	H2 Weight (kg)	Efficiency	Voltage (V)	Capacity (mAhr)	Required temp. is between 60C and 90C (140F to 194F)		
	0.05232162	0.0024003	0.4	12	2667.9216			
	H2O Volume	NaBH4						
	21.44665086	20.969279						
Hydrogen	Volume (cm^3)	R J/(mol *K)	Temp. (K)	Δho (kJ/mol)	moles	W hr/cm^3	W hr/kg	W hr
(pressurized tank)	51.210	8.3145	298	-242	0.27098	0.1423	13.5531	7.2865
With Cell	Pressure (psi)	Pressure (Pa)	Efficiency	Voltage (V)	Capacity (mAhr)			
	5800	4.00E+07	0.4	12	607.2073			
	Volume tank (cm^3)	Volume F.C. (cm^3)						
	16.79	31.344						
Hydrogen	Volume (cm^3)	R J/(mol *K)	Temp. (K)	Δho (kJ/mol)	moles	W hr/cm^3	W hr/kg	W hr
(pressurized tank)	51.210	8.3145	298	-242	0.46721	0.2453	138.9255	12.562
With Cell	Pressure (psi)	Pressure (Pa)	Efficiency	Voltage (V)	Capacity (mAhr)			
	10000	6.89E+07	0.4	12	1046.9093			
	Volume tank (cm^3)	Volume F.C. (cm^3)						
	16.79	31.344						
Hydrogen	Total Volume	R J/(mol	Temp. (K)	Δho (kJ/mol)	moles	W	W hr/kg	W hr
Metal Hydride	51.210	8.3145	298	-242	0.27901	0.1465	87.9078	7.502
With Cell	System Weight (kg)	H2 Weight (kg)	Efficiency	Voltage (V)	Capacity (mAhr)			
	0.085343224	0.0005624	0.4	12	625.1949			
	Metal Hydride Volume (cm^3)							
	19.865575							
Hydrogen	Total Volume (cm^3)	R J/(mol *K)	Temp. (K)	Δho (kJ/mol)	moles	W hr/cm^3	W hr/kg	W hr
Sodium Borohydride	51.210	8.3145	333	-242	0.39471	0.2072	216.1561	10.613
With Cell	System Weight (kg)	H2 Weight	Efficiency	Voltage (V)	Capacity (mAhr)	Required temp. is between 60C and 90C (140F to 194F)		
	0.0490998	0.0007957	0.4	12	884.4355			
	H2O Volume (cm^3)	NaBH4 Volume (cm^3)						
	7.1047216	6.951469						

Table A3a Evaluation of MeOH as a fuel in conjunction with DMFC technology for MAV power plants.

Methanol	Volume (cm^3)	Molar mass (gm/mol)	Temp. (K)	Δho (kJ/mol)	moles	W hr/cm^3	W hr/kg	W hr
1.5 Molar	43.100	32.04	298	-676.5	0.06465	0.0632	54.2368	2.7259
	Density (kg/cm^3)	Weight (kg)	Efficiency	Voltage (V)	Capacity (mAhr)	% methanol by volume		
Methanol	0.0007918	0.00207138	0.22	12	227.1593	6.0697		
Water	0.001	0.04048400	Molarity	moles (water)				
	Total	0.04255539	1.5	2.249111565				
Methanol	Volume (cm^3)	Molar mass (gm/mol)	Temp. (K)	Δho (kJ/mol)	Moles	W hr/cm^3	W hr/kg	W hr
2.5 Molar	43.100	32.04	298	-676.5	0.10775	0.1757	151.7542	7.5720
	Density (kg/cm^3)	Weight (kg)	Efficiency	Voltage (V)	Capacity (mAhr)	% methanol by volume		
Methanol	0.0007918	0.00345231	0.37	12	630.9982	10.1162		
Water	0.001	0.03873997	Molarity	moles (water)				
	Total	0.04219228	2.5	2.152220804				
Methanol	Volume (cm^3)	Molar mass (gm/mol)	Temp. (K)	Δho (kJ/mol)	Moles	W hr/cm^3	W hr/kg	W hr
3.25 Molar	43.100	32.04	298	-676.5	0.14007	0.2969	257.8721	12.7966
	Density (kg/cm^3)	Weight (kg)	Efficiency	Voltage (V)	Capacity (mAhr)	% methanol by volume		
Methanol	0.0007918	0.00448800	0.49	12	1066.386	13.1510		
Water	0.001	0.03743194	Molarity	moles (water)				
	Total	0.04191995	3.25	2.079552733				
Methanol	Volume (cm^3)	Molar mass (gm/mol)	Temp. (K)	Δho (kJ/mol)	Moles	W hr/cm^3	W hr/kg	W hr
24.5 Molar	43.100	32.04	298	-676.5	1.05595	2.5322	2604.2066	109.1370
	Density (kg/cm^3)	Weight (kg)	Efficiency	Voltage (V)	Capacity (mAhr)	% methanol by volume		
Methanol	0.0007918	0.03383268	0.55	12	9094.748	99.1387		
Water	0.001	0.00037123	Molarity	moles (water)				
	Total	0.03420391	24.5	0.020624063				
Methanol	Volume (cm^3)	Molar mass (gm/mol)	Temp. (K)	Δho (kJ/mol)	Moles	W hr/cm^3	W hr/kg	W hr
(Passive)	16.290	32.04	298	-676.5	0.39910	1.0330	345.3155	16.8278
1.5 Molar	Density (kg/cm^3)	Weight (kg)	Efficiency	Voltage (V)	Capacity (mAhr)	% methanol by volume in tank	% methanol by volume at MEA	
Methanol	0.0007918	0.01278724	0.22	12	1402.316			
Water	0.001	0.00014031	Molarity Tank	moles (water)	Molarity PEM	99.1387	6.0697	
Fuel Cell		0.0324072	24.5	0.007794974	1.5			
	Total	0.04533475						

Table A3b Evaluation of MeOH as a fuel in conjunction with DMFC technology for MAV power plants.

Methanol	Volume (cm^3)	Molar mass (gm/mol)	Temp. (K)	Δho (kJ/mol)	Moles	W hr/cm^3	W hr/kg	W hr
(Passive)	16.290	32.04	298	-676.5	0.39910	1.7217	575.5258	28.0463
2.5 Molar	Density (kg/cm^3)	Weight (kg)	Efficiency	Voltage (V)	Capacity (mAhr)	% methanol by volume in tank	% methanol by volume at MEA	
Methanol	0.0007918	0.01278724	0.37	12	2337.193			
Water	0.001	0.00014031	Molarity Tank	moles (water)	Molarity PEM	99.1387	10.1161	
Fuel Cell		0.0324072	24.5	0.007794974	2.5			
	Total	0.04533475						
Methanol	Volume (cm^3)	Molar mass (gm/mol)	Temp. (K)	Δho (kJ/mol)	Moles	W hr/cm^3	W hr/kg	W hr
(Passive)	16.290	32.04	298	-676.5	0.39910	2.2382	748.1835	36.4602
3.25 Molar	Density (kg/cm^3)	Weight (kg)	Efficiency	Voltage (V)	Capacity (mAhr)	% methanol by volume in tank	% methanol by volume at MEA	
Methanol	0.0007918	0.01278724	0.49	12	3038.351			
Water	0.001	0.00014031	Molarity Tank	moles (water)	Molarity PEM	99.1387	13.1510	
Fuel Cell		0.0324072	24.5	0.007794974	3.25			
	Total	0.04533475						
Methanol	Volume (cm^3)	Molar mass (gm/mol)	Temp. (K)	Δho (kJ/mol)	Moles	W hr/cm^3	W hr/kg	W hr
(Passive)	16.290	32.04	298	-676.5	0.39910	2.5322	846.4499	41.2489
24.5 Molar	Density (kg/cm^3)	Weight (kg)	Efficiency	Voltage (V)	Capacity (mAhr)	% methanol by volume in tank	% methanol by volume at MEA	
Methanol	0.0007918	0.01278724	0.55	12	3437.408			
Water	0.001	0.00014031	Molarity Tank	moles (water)	Molarity PEM	99.1387	99.1387	
Fuel Cell		0.0324072	24.5	0.007794974	24.5			
	Total	0.04533475						

Table A4a Evaluation of HCOOH as a fuel in conjunction with DFAC technology for MAV power plants.

Formic Acid	Volume (cm^3)	Molar mass (gm/mol)	Temp. (K)	Δho (kJ/mol)	moles	W hr/cm^3	W hr/kg	W hr
1 Molar	43.100	46.03	298	-257.19	0.04310	0.0016	1.3306	0.0680
	Density (kg/cm^3)	Weight (kg)	Efficiency	Voltage (V)	Capacity (mAhr)	% formic acid by volume		
Formic Acid	0.0012	0.001983896	0.02	12	5.6698	3.835833333		
Water	0.001	0.041446812	Molarity	moles (water)				
	Total	0.043430708	1	2.30260				

Formic Acid	Volume (cm^3)	Molar mass (gm/mol)	Temp. (K)	Δho (kJ/mol)	moles	W hr/cm^3	W hr/kg	W hr
10 Molar	43.100	46.03	298	-257.19	0.43100	0.1579	125.7389	6.8038
	Density (kg/cm^3)	Weight (kg)	Efficiency	Voltage (V)	Capacity (mAhr)	% formic acid by volume		
Formic Acid	0.0012	0.019838957	0.22	12	566.9839	38.35833333		
Water	0.001	0.026567595	Molarity	moles (water)				
	Total	0.046406552	10	1.47597747				
Formic Acid	Volume (cm^3)	Molar mass (gm/mol)	Temp. (K)	Δho (kJ/mol)	moles	W hr/cm^3	W hr/kg	W hr
21 Molar	43.100	46.03	298	-257.19	0.90510	0.6962	519.5838	30.004
	Density (kg/cm^3)	Weight (kg)	Efficiency	Voltage (V)	Capacity (mAhr)	% formic acid by volume		
Formic Acid	0.0012	0.04166181	0.46	12	2500.399	80.5525		
Water	0.001	0.008381884	Molarity	moles (water)				
	Total	0.050043694	21	0.46566021				
Formic Acid	Volume (cm^3)	Molar mass (gm/mol)	Temp. (K)	Δho (kJ/mol)	moles	W hr/cm^3	W hr/kg	W hr
26 Molar	43.100	46.03	298	-257.19	1.12060	1.0671	774.2925	45.993
	Density (kg/cm^3)	Weight (kg)	Efficiency	Voltage (V)	Capacity (mAhr)	% formic acid by volume		
Formic Acid	0.0012	0.051581288	0.57	12	3832.811	99.73166667		
Water	0.001	0.000115652	Molarity	moles (water)				
	Total	0.05169694	26	0.00642510				
Formic Acid	Volume (cm^3)	Molar mass (gm/mol)	Temp. (K)	Δho (kJ/mol)	moles	W hr/cm^3	W hr/kg	W hr
(Passive)	16.290	46.03	298	-257.19	0.42353	0.0410	12.0810	0.6686
1 Molar	Density (kg/cm^3)	Weight (kg)	Efficiency	Voltage (V)	Capacity (mAhr)	% formic acid by volume in tank	% formic acid by volume at MEA	
Formic Acid	0.0012	0.019495421	0.02	12	55.7165	99.73166667	3.835833	
Water	0.001	4.37112E-05	Molarity Tank	moles (water)	Molarity (PEM)			
Fuel Cell		0.0324072	26	0.00242840	1			
	Total	0.051946332						

Appendix B

Flat Plate versus Tubular Figures and Tables

The equations used to generate the values found in the tables below are found in Section 3.4. Given in the present appendix are the additional figures that were omitted from section Chapter 6 Results and Discussion. The data for all of these figures appears in Tables B1 to B4. In particular, the data for Figures B1, B3, B5, and B7, which show the volume comparisons for the different configurations, is given in Tables B1 and B2, while that for the weight comparisons in Figures B2, B4, B6, and B8 appears in Tables B3 and B4.

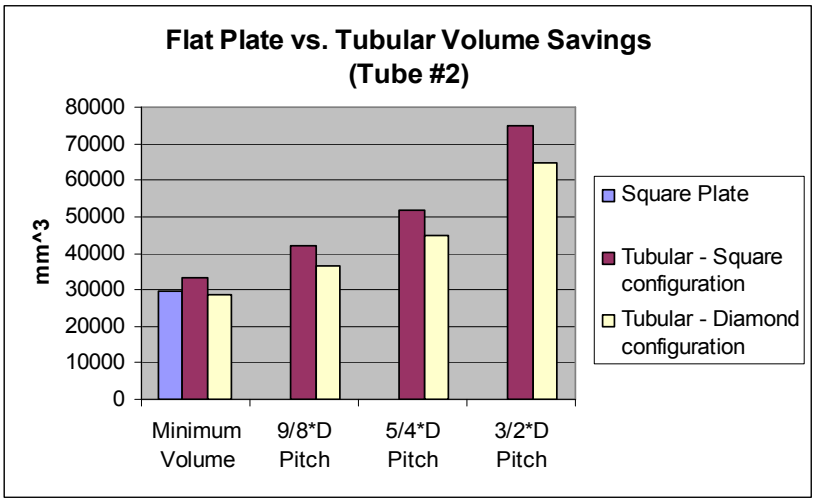

Figure B1 Volume savings of the micro-tubular design versus the flat plate design for tube #2.

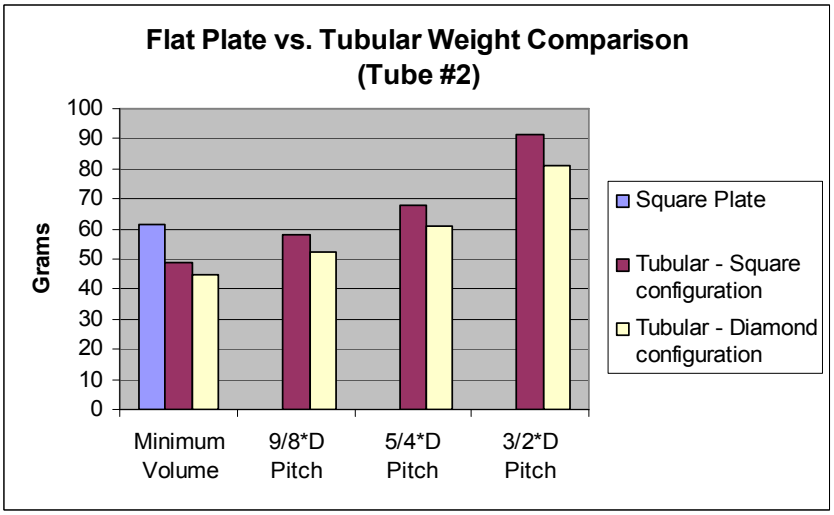

Figure B2 Weight savings of the micro-tubular design versus the flat plate design for tube #2.

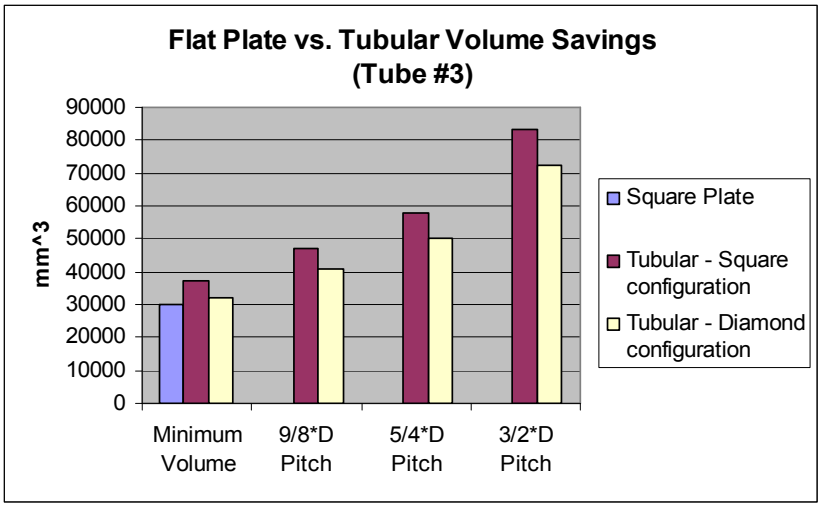

Figure B3 Volume savings of the micro-tubular design versus the flat plate design for tube #3.

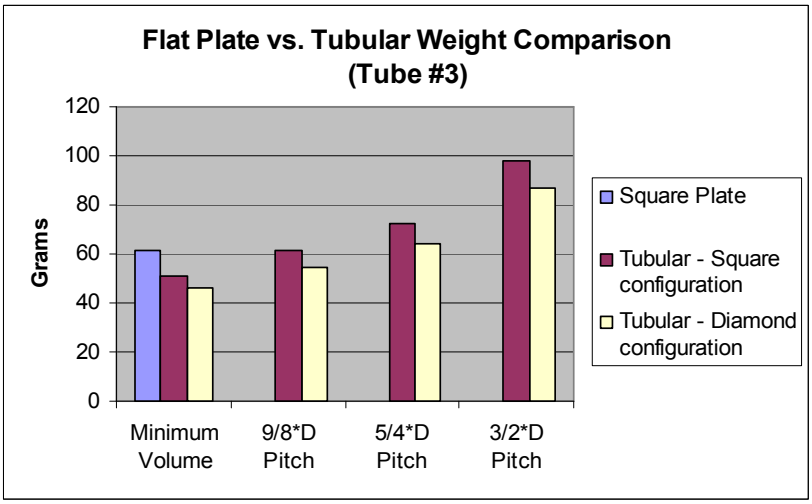

Figure B4 Weight savings of the micro-tubular design versus the flat plate design for tube #3.

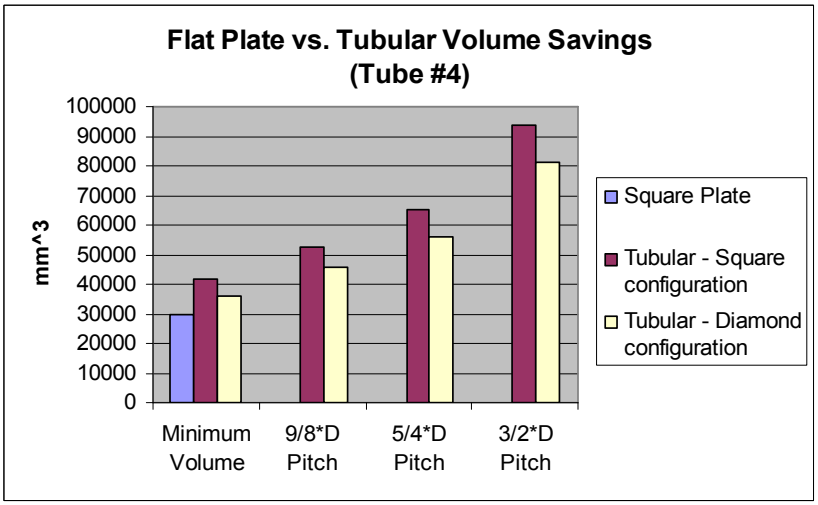

Figure B5 Volume savings of the micro-tubular design versus the flat plate design for tube #4.

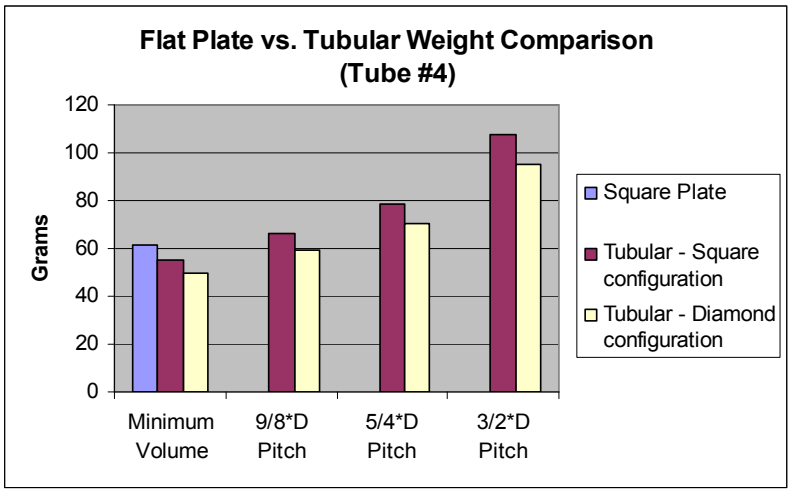

Figure B6 Weight savings of the micro-tubular design versus the flat plate design for tube #4.

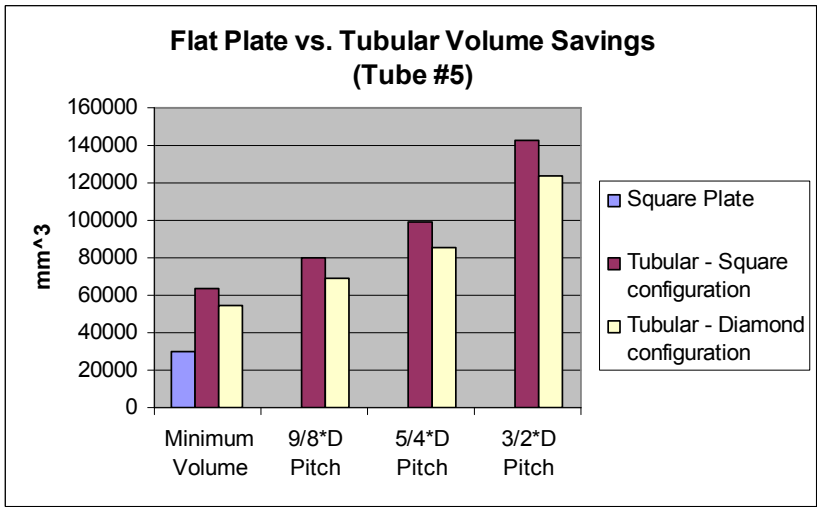

Figure B7 Volume savings of the micro-tubular design versus the flat plate design for tube #5.

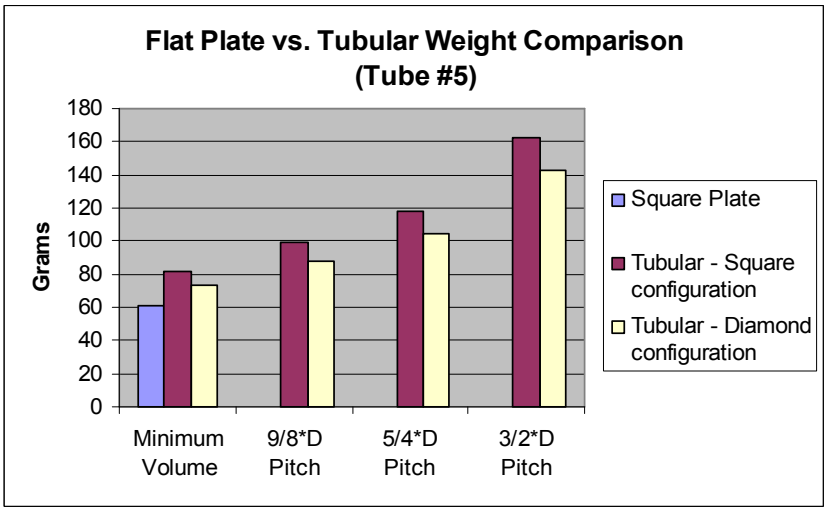

Figure B8 Weight savings of the micro-tubular design versus the flat plate design for tube #5.

Table B1 Evaluation of tubular fuel cells (square pattern) and flat plate cell volumes.

	tubing only	tubing only	tubing only	tubing with cat./silver	tubing with cat./silver	for 1 plate	for 1 cell	for 24 cells
	OD (mm)	ID (mm)	t of mem. (mm)	OD (mm)	ID (mm)	H of ID (mm)	H of ID (mm)	H of ID (mm)
1	0.838	0.635	0.1016	0.888	0.585	54.41194636	1088.238927	26117.73425
2	1.346	1.067	0.1397	1.396	1.017	31.2989072	625.9781439	15023.47545
3	1.6	1.321	0.1397	1.65	1.271	25.04405084	500.8810168	12021.1444
4	1.829	1.524	0.1524	1.879	1.474	21.59497193	431.8994385	10365.58652
5	2.743	2.184	0.2794	2.793	2.134	14.91611463	298.3222926	7159.735022

	Area Square Plate	Per cell	24 cells needed
(cm^2)	1	20	480
(mm^2)	100	2000	48000

	Volume Square plate 1 cell	24 cells
(mm^3)	1240.25	29766

Square formation Assumed H= 14 L= the pitch

Minimum Top Areas L=0

			Top	mm^3		Top	mm^3		Top	mm^3
(mm^2)	Area/tube	# tubes/plate	Area/plate	Volume/plate	# tubes/cell	Area/cell	Volume/cell	# tubes/24 cells	Area/24 cells	Volume/24 cells
1	0.788544	4	3.154176	50.072544	78	61.506432	976.414608	1866	1471.423104	23358.84178
2	1.948816	3	5.846448	92.812362	45	87.69672	1392.18543	1074	2093.028384	33226.8256
3	2.7225	2	5.445	86.439375	36	98.01	1555.90875	859	2338.6275	37125.71156
4	3.530641	2	7.061282	112.0978518	31	109.449871	1737.516702	741	2616.204981	41532.25407
5	7.800849	2	15.601698	247.6769558	22	171.618678	2724.446513	512	3994.034688	63405.30067

Square formation Assumed H= 14

Top Areas Assuming L=9/8*D

			Top	mm^3		Top	mm^3		Top	mm^3
(mm^2)	Area/tube	# tubes/plate	Area/plate	Volume/plate	# tubes/cell	Area/cell	Volume/cell	# tubes/24 cells	Area/24 cells	Volume/24 cells
1	0.998001	4	3.992004	63.3730635	78	77.844078	1235.774738	1866	1862.269866	29563.53412
2	2.46647025	3	7.39941075	117.4656457	45	110.9911613	1761.984685	1074	2648.989049	42052.70114
3	3.445664063	2	6.891328125	109.399834	36	124.0439063	1969.197012	859	2959.82543	46987.2287
4	4.468467516	2	8.936935031	141.8738436	31	138.522493	2199.044576	741	3311.134429	52564.25906
5	9.872949516	2	19.74589903	313.4661471	22	217.2048893	3448.127618	512	5054.950152	80247.33366

Square formation Assumed H= 14

Top Areas Assuming L=5/4*D

			Top	mm^3		Top	mm^3		Top	mm^3
(mm^2)	Area/tube	# tubes/plate	Area/plate	Volume/plate	# tubes/cell	Area/cell	Volume/cell	# tubes/24 cells	Area/24 cells	Volume/24 cells
1	1.2321	4	4.9284	78.23835	78	96.1038	1525.647825	1866	2299.0986	36498.19028
2	3.045025	3	9.135075	145.0193156	45	137.026125	2175.289734	1074	3270.35685	51916.91499
3	4.25390625	2	8.5078125	135.0615234	36	153.140625	2431.107422	859	3654.105469	58008.92432
4	5.516626563	2	11.03325313	175.1528934	31	171.0154234	2714.869847	741	4087.820283	64894.14699
5	12.18882656	2	24.37765313	386.9952434	22	268.1541844	4256.947677	512	6240.6792	99070.7823

Square formation Assumed H= 14

Top Areas Assuming L=3/2*D

			Top	mm^3		Top	mm^3		Top	mm^3
(mm^2)	Area/tube	# tubes/plate	Area/plate	Volume/plate	# tubes/cell	Area/cell	Volume/cell	# tubes/24 cells	Area/24 cells	Volume/24 cells
1	1.774224	4	7.096896	112.663224	78	138.389472	2196.932868	1866	3310.701984	52557.394
2	4.384836	3	13.154508	208.8278145	45	197.31762	3132.417218	1074	4709.313864	74760.35759
3	6.125625	2	12.25125	194.4885938	36	220.5225	3500.794688	859	5261.911875	83532.85102
4	7.94394225	2	15.8878845	252.2201664	31	246.2622098	3909.41258	741	5886.461207	93447.57167
5	17.55191025	2	35.1038205	557.2731504	22	386.1420255	6130.004655	512	8986.578048	142661.9265

Table B2 Evaluation of tubular fuel cells (diamond pattern) volumes

Diamond formation Assumed H= 14

Top Areas Assuming W=D, Z=3^.5*D

			Top	mm^3		Top	mm^3		Top	mm^3
(mm^2)	Area/tube	# tubes/plate	Area/plate	Volume/plate	# tubes/cell	Area/cell	Volume/cell	# tubes/24 cells	Area/24 cells	Volume/24 cells
1	0.682899136	4	2.731596544	43.36409514	78	53.26613261	845.5998552	1866	1274.289788	20229.35038
2	1.687724163	3	5.06317249	80.37786328	45	75.94758735	1205.667949	1074	1812.615751	28775.27505
3	2.357754162	2	4.715508324	74.85869464	36	84.87914982	1347.456503	859	2025.310825	32151.80935
4	3.057624798	2	6.115249595	97.07958733	31	94.78636873	1504.733604	741	2265.699975	35967.9871
5	6.755733405	2	13.51146681	214.4945356	22	148.6261349	2359.439892	512	3458.935503	54910.60112

Diamond formation Assumed H= 14

Top Areas Assuming W=9/8*D, Z=3^.5*(9/8*D)

			Top	mm^3		Top	mm^3		Top	mm^3
(mm^2)	Area/tube	# tubes/plate	Area/plate	Volume/plate	# tubes/cell	Area/cell	Volume/cell	# tubes/24 cells	Area/24 cells	Volume/24 cells
1	0.864294219	4	3.457176876	54.88268291	78	67.41494908	1070.212317	1866	1612.773013	25602.77158
2	2.136025894	3	6.408077683	101.7282332	45	96.12116524	1525.923498	1074	2294.09181	36418.70749
3	2.984032611	2	5.968065222	94.7430354	36	107.425174	1705.374637	859	2563.284013	40692.1337
4	3.869806385	2	7.739612769	122.8663527	31	119.9639979	1904.428467	741	2867.526531	45521.98368
5	8.550225091	2	17.10045018	271.4696466	22	188.104952	2986.166113	512	4377.715246	69496.22954

Diamond formation Assumed H= 14

Top Areas Assuming W=5/4*D, Z=3^.5*(5/4*D)

			Top	mm^3		Top	mm^3		Top	mm^3
(mm^2)	Area/tube	# tubes/plate	Area/plate	Volume/plate	# tubes/cell	Area/cell	Volume/cell	# tubes/24 cells	Area/24 cells	Volume/24 cells
1	1.0670299	4	4.2681196	67.75639865	78	83.2283322	1321.249774	1866	1991.077793	31608.35997
2	2.637069005	3	7.911207015	125.5904114	45	118.6681052	1883.856171	1074	2832.212112	44961.36727
3	3.683990878	2	7.367981756	116.9667104	36	132.6236716	2105.400787	859	3164.548164	50237.2021
4	4.777538746	2	9.555077493	151.6868552	31	148.1037011	2351.146256	741	3540.156211	56199.97985
5	10.55583345	2	21.11166689	335.1477119	22	232.2283358	3686.624831	512	5404.586724	85797.81424

Diamond formation Assumed H= 14

Top Areas Assuming W=3/2*D, Z=3^.5*(3/2*D)

			Top	mm^3		Top	mm^3		Top	mm^3
(mm^2)	Area/tube	# tubes/plate	Area/plate	Volume/plate	# tubes/cell	Area/cell	Volume/cell	# tubes/24 cells	Area/24 cells	Volume/24 cells
1	1.536523056	4	6.146092224	97.56921406	78	119.8487984	1902.599674	1866	2867.152023	45516.03836
2	3.797379367	3	11.3921381	180.8501924	45	170.8820715	2712.752886	1074	4078.385441	64744.36887
3	5.304946864	2	10.60989373	168.4320629	36	190.9780871	3031.777133	859	4556.949356	72341.57103
4	6.879655795	2	13.75931159	218.4290715	31	213.2693296	3385.650608	741	5097.824944	80927.97098
5	15.20040016	2	30.40080032	482.6127051	22	334.4088036	5308.739756	512	7782.604883	123548.8525

Table B3 Evaluation of tubular fuel cells (square pattern) masses.

Material	Thickness (mm)	density (gm/mm^3)	
catalyst	0.005	0.00158	Assume nafion
electrode	0.02	0.0084	Assuming 80% silver, and 20% air
tubing	varies	0.00158	Assume nafion
end plates	0.3988	0.008	assume stainless steel
tube plates	0.3988	0.008	assume stainless steel

Minimum - square configuration

	Tube 1	Tube 2	Tube 3	Tube 4	Tube 5
W (mm)	30.95	30.95	30.95	30.95	30.95
L (mm)	47.541942	67.62611903	75.56147011	84.53005	129.048
He (mm)	15.875	15.875	15.875	15.875	15.875
Ht (mm)	14	14	14	14	14
OD assembly (mm)	0.888	1.396	1.65	1.879	2.793
OD tubing (mm)	0.838	1.346	1.6	1.829	2.743
ID tubing (mm)	0.635	1.067	1.321	1.524	2.184
# of tubes	1866	1074	859	741	512
Tube plate (gm)	2.0148659	2.866049485	3.202356066	3.582452	5.469157
End plates (gm)	17.621257	23.67313407	26.06425868	28.76672	42.18111
Tube total (gm)	20.297944	22.57016382	21.85504622	22.76499	34.24893
Total mass (gm)	39.934066	49.10934738	51.12166097	55.11417	81.8992

9/8*D - square configuration

	Tube 1	Tube 2	Tube 3	Tube 4	Tube 5
W (mm)	30.95	30.95	30.95	30.95	30.95
L (mm)	60.17027	85.5893069	95.63248561	106.9833	163.3263
He (mm)	15.875	15.875	15.875	15.875	15.875
Ht (mm)	14	14	14	14	14
OD assembly (mm)	0.888	1.396	1.65	1.879	2.793
OD tubing (mm)	0.838	1.346	1.6	1.829	2.743
ID tubing (mm)	0.635	1.067	1.321	1.524	2.184
# of tubes	1866	1074	859	741	512
Tube plate (gm)	4.5087809	6.413523293	7.166095816	8.016657	12.23865
End plates (gm)	21.426496	29.08590285	32.11216993	35.53247	52.51006
Tube total (gm)	20.297944	22.57016382	21.85504622	22.76499	34.24893
Total mass (gm)	46.23322	58.06958997	61.13331197	66.31412	98.99764

5/4*D - square configuration

	Tube 1	Tube 2	Tube 3	Tube 4	Tube 5
W (mm)	30.95	30.95	30.95	30.95	30.95
L (mm)	74.284284	105.665811	118.0647971	132.0782	201.6375
He (mm)	15.875	15.875	15.875	15.875	15.875
Ht (mm)	14	14	14	14	14
OD assembly (mm)	0.888	1.396	1.65	1.879	2.793
OD tubing (mm)	0.838	1.346	1.6	1.829	2.743
ID tubing (mm)	0.635	1.067	1.321	1.524	2.184
# of tubes	1866	1074	859	741	512
Tube plate (gm)	7.2960977	10.37834696	11.59615789	12.97253	19.80455
End plates (gm)	25.67941	35.13546795	38.87160015	43.0942	64.05418
Tube total (gm)	20.297944	22.57016382	21.85504622	22.76499	34.24893
Total mass (gm)	53.273451	68.08397874	72.32280426	78.83172	118.1077

3/2*D - square configuration

	Tube 1	Tube 2	Tube 3	Tube 4	Tube 5
W (mm)	30.95	30.95	30.95	30.95	30.95
L (mm)	106.96937	152.1587678	170.0133078	190.1926	290.3579
He (mm)	15.875	15.875	15.875	15.875	15.875
Ht (mm)	14	14	14	14	14
OD assembly (mm)	0.888	1.396	1.65	1.879	2.793
OD tubing (mm)	0.838	1.346	1.6	1.829	2.743
ID tubing (mm)	0.635	1.067	1.321	1.524	2.184
# of tubes	1866	1074	859	741	512
Tube plate (gm)	13.750937	19.56004388	21.85524901	24.4493	37.32558
End plates (gm)	35.528264	49.14498714	54.52501751	60.60556	90.78794
Tube total (gm)	20.297944	22.57016382	21.85504622	22.76499	34.24893
Total mass (gm)	69.577144	91.27519484	98.23531273	107.8199	162.3624

Table B4 Evaluation of tubular fuel cells (diamond pattern) masses.

Minimum - diamond configuration

	Tube 1	Tube 2	Tube 3	Tube 4	Tube 5
W (mm)	30.95	30.95	30.95	30.95	30.95
L (mm)	41.172529	58.56593704	65.43815267	73.20517	111.7588
He (mm)	15.875	15.875	15.875	15.875	15.875
Ht (mm)	14	14	14	14	14
OD assembly (mm)	0.888	1.396	1.65	1.879	2.793
OD tubing (mm)	0.838	1.346	1.6	1.829	2.743
ID tubing (mm)	0.635	1.067	1.321	1.524	2.184
# of tubes	1866	1074	859	741	512
Tube plate (gm)	0.7569976	1.076792559	1.203145026	1.345949	2.054796
End plates (gm)	15.70199	20.94306909	23.01384375	25.35424	36.97145
Tube total (gm)	20.297944	22.57016382	21.85504622	22.76499	34.24893
Total mass (gm)	36.756931	44.59002547	46.07203499	49.46519	73.27518

9/8*D - Diamond configuration

	Tube 1	Tube 2	Tube 3	Tube 4	Tube 5
W (mm)	30.95	30.95	30.95	30.95	30.95
L (mm)	52.108983	74.12251407	82.82016197	92.65029	141.4448
He (mm)	15.875	15.875	15.875	15.875	15.875
Ht (mm)	14	14	14	14	14
OD assembly (mm)	0.888	1.396	1.65	1.879	2.793
OD tubing (mm)	0.838	1.346	1.6	1.829	2.743
ID tubing (mm)	0.635	1.067	1.321	1.524	2.184
# of tubes	1866	1074	859	741	512
Tube plate (gm)	2.9167914	4.148994996	4.635844344	5.186084	7.917346
End plates (gm)	18.997423	25.63066436	28.25148853	31.21356	45.91658
Tube total (gm)	20.297944	22.57016382	21.85504622	22.76499	34.24893
Total mass (gm)	42.212158	52.34982318	54.74237909	59.16464	88.08286

5/4*D - Diamond configuration

	Tube 1	Tube 2	Tube 3	Tube 4	Tube 5
W (mm)	30.95	30.95	30.95	30.95	30.95
L (mm)	64.332077	91.50927662	102.2471135	114.3831	174.6232
He (mm)	15.875	15.875	15.875	15.875	15.875
Ht (mm)	14	14	14	14	14
OD assembly (mm)	0.888	1.396	1.65	1.879	2.793
OD tubing (mm)	0.838	1.346	1.6	1.829	2.743
ID tubing (mm)	0.635	1.067	1.321	1.524	2.184
# of tubes	1866	1074	859	741	512
Tube plate (gm)	5.3306785	7.582633014	8.472390639	9.478	14.46961
End plates (gm)	22.680555	30.86974142	34.10532682	37.7622	55.91408
Tube total (gm)	20.297944	22.57016382	21.85504622	22.76499	34.24893
Total mass (gm)	48.309177	61.02253825	64.43276367	70.0052	104.6326

3/2*D - Diamond configuration

	Tube 1	Tube 2	Tube 3	Tube 4	Tube 5
W (mm)	30.95	30.95	30.95	30.95	30.95
L (mm)	92.638191	131.7733583	147.2358435	164.7116	251.4573
He (mm)	15.875	15.875	15.875	15.875	15.875
Ht (mm)	14	14	14	14	14
OD assembly (mm)	0.888	1.396	1.65	1.879	2.793
OD tubing (mm)	0.838	1.346	1.6	1.829	2.743
ID tubing (mm)	0.635	1.067	1.321	1.524	2.184
# of tubes	1866	1074	859	741	512
Tube plate (gm)	10.920733	15.53421579	17.35702417	19.41717	29.64327
End plates (gm)	31.209912	43.00234093	47.6615839	52.92749	79.06619
Tube total (gm)	20.297944	22.57016382	21.85504622	22.76499	34.24893
Total mass (gm)	62.428589	81.10672054	86.87365428	95.10965	142.9584

Appendix C

Additional MTFC Experimental Testing Results

The figures shown below are a continuation of the data presented in Section 6.2 of Chapter 6. Between the figures presented here and in Section 6.2 a polarization and power curve for each cell with usable results is shown. Polarization and power curves of MTFCs 5, 8, 10,12, 13, and 17 are shown.

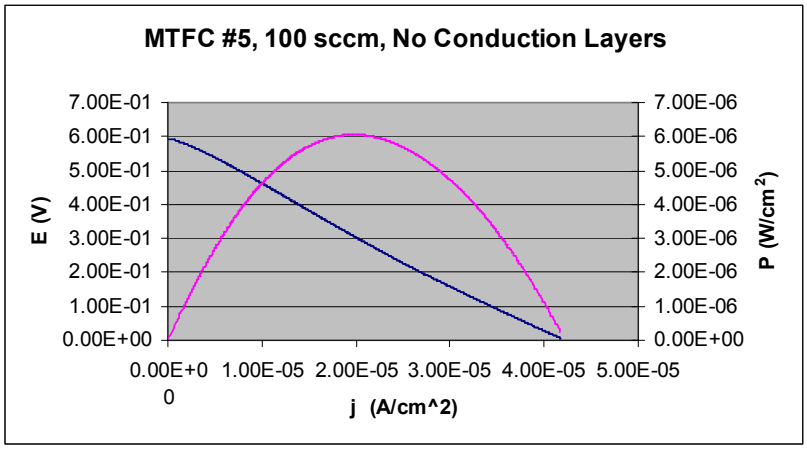

Figure C1 Performance of MTFC #5 at 100 sccm with no conduction layers added

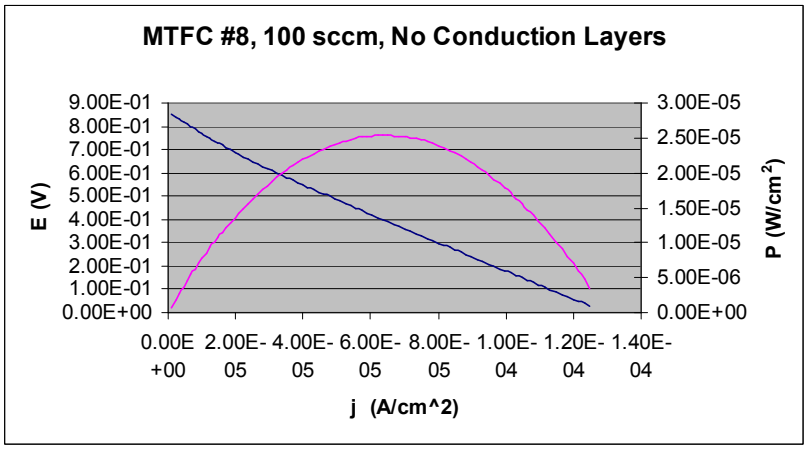

Figure C2 Performance of MTFC #8 at 100 sccm with no conduction layers added

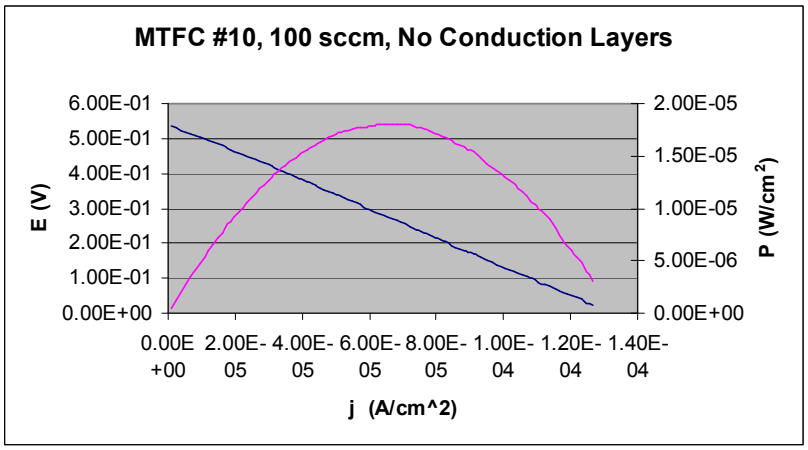

Figure C3 Performance of MTFC #10 at 100 sccm with no conduction layers added

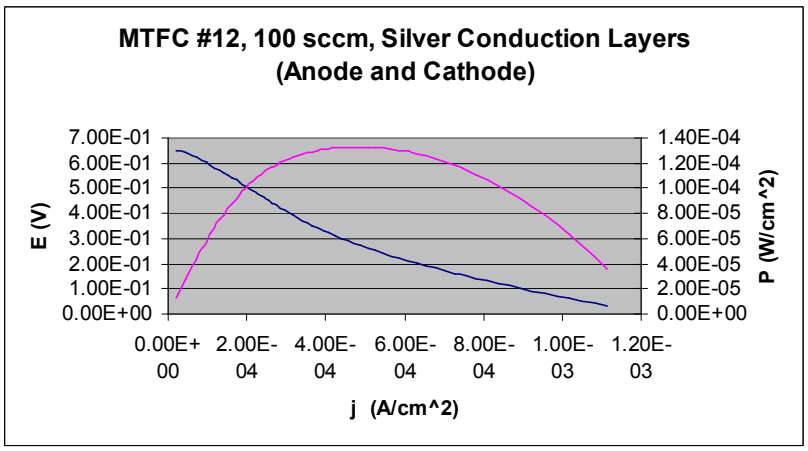

Figure C4 Performance of MTFC #12 at 100 sccm with no conduction layers added

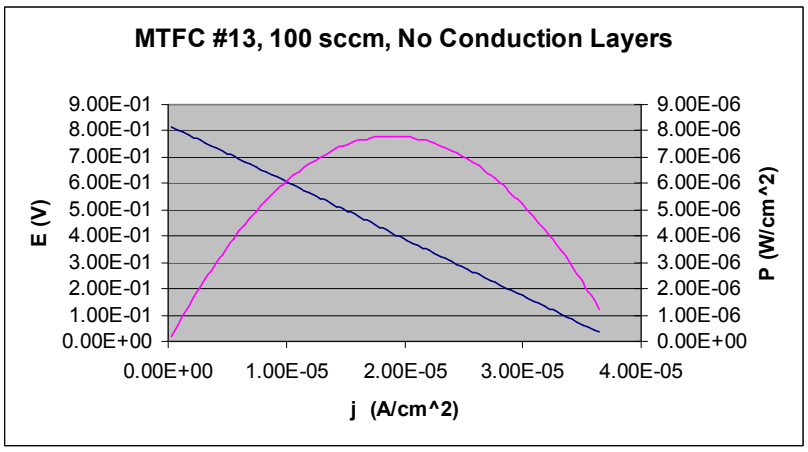

Figure C5 Performance of MTFC #13 at 100 sccm with no conduction layers added

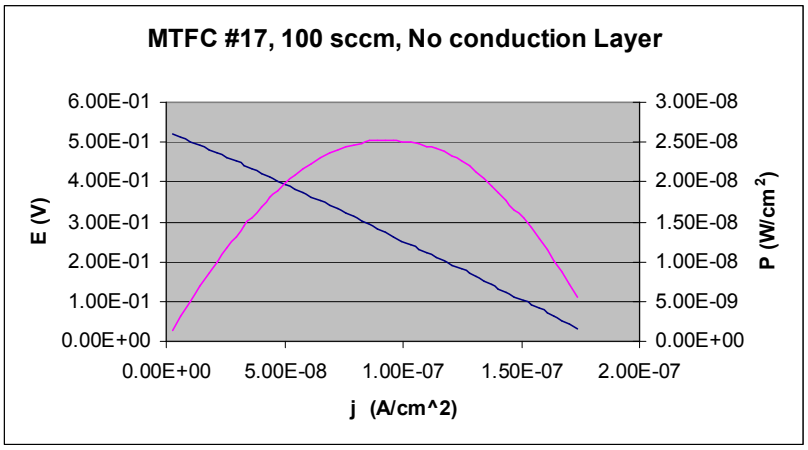

Figure C6 Performance of MTFC #17 at 100 sccm with no conduction layers added